The Pennsylvania State University

The Graduate School

College of Earth and Mineral Sciences

DETERMINATION OF FLUID TRANSPORT PROPERTIES FROM CONE PENETROMETER SOUNDING DATA

A Thesis in

Energy and Geo-Environmental Engineering

by

Dae Sung Lee

Submitted in Partial Fulfillment
of the Requirements
for the Degree of

Doctor of Philosophy

August, 2006

The thesis of Dae Sung Lee has been reviewed and approved by the following:

Derek Elsworth
Professor of Energy and Geo-Environmental Engineering
Thesis Advisor
Chair of Committee

Abraham S. Grader
Professor of Petroleum and Natural Gas Engineering

Peter B. Flemings
Professor of Geosciences

Chris J. Marone
Professor of Geosciences

Yaw D. Yeboah
Professor of Energy and Geo-Environmental Engineering
Head of the Department of Energy and Geo-Environmental Engineering

Abstract

This work examines the hypothesis that the form and magnitude of the pore fluid pressure field, which develops around an advancing penetrometer, is conditioned by in-situ permeability; correspondingly penetration-induced pore pressures may be used to estimate permeability distribution, *on-the-fly*. Mechanistic models are developed to describe the steady, partially-drained, fluid pressure field which develops around an advancing penetrometer. These models are used to rationalize the recovery of in-situ permeability profiles (K_D) from the cone metrics of excess pore pressures (B_q), end-bearing (Q_t), and sleeve friction (F_r), recovered during penetration. The determination of permeability is possible only if penetration-generated pore pressures are partially drained. To enable permeabilities to be recovered from uCPT data gathered *on-the-fly*, plausible limits are defined for the transition from partially-drained to undrained behavior during penetrometer advance (Chapter 1). These show that permeability may be determined from the excess pore pressures through a relation of the form $K_D = 0.62/(B_q Q_t)^{1.6}$ for $B_q Q_t < 1.2$ where the penetration response is both partially drained and steady.

Where the penetration-induced pore pressure field is undrained, tip-local permeabilities cannot be determined. Instead, the undrained pore pressures may be used to recover undrained pore pressure coefficients from the instantaneous pressure data, and consolidation coefficients from their dissipation. To represent this behavior, anomalous pore pressure dissipation records are accommodated in cavity expansion models in terms of pore pressures developed as a result of undrained dilation in the soil within the tip process zone (Chapter 2). These results reveal that the consolidation coefficient,

undrained strength and shear modulus may be determined directly from the dissipation response, and confirmed against independent measurements.

Steady models for the excess pore pressure field are applied to define continuous profiles of permeability based on pore pressure data from uCPT profiles. These predictions are validated against independent measurements of permeabilities from slug tests, direct-push permeameter (DPP) profiling, and grain-size correlations completed at an unusually well characterized field site in Nauen, Germany (Chapter 3). These confirm that permeabilities may indeed be estimated from cone metrics, with the estimates of average permeabilities of the order of 6% higher than those measured from direct-push permeameter (DPP) profiling.

Permeabilities interpreted from cone metrics recovered on-the-fly are also compared with a dense suite of measurements from a variety of independent methods. These include measurements by standard direct-push permeameters, by low-disturbance thin-tipped permeameters, and through grain size correlations recovered from high-quality Vision-CPT. These characterizations, completed at the Geohydrologic Experimental and Monitoring Site (GEMS), Kansas (Chapter 4), show that sample disturbance during penetration by a standard uCPT is minor; permeabilities measured at the tip of a standard cone (60° tip and 10 cm2 area) are therefore representative of in situ permeabilities. Furthermore, direct-push permeameter measurements, show remarkably close agreement with the relation $K_D = 1/(B_q Q_t)$, where undrained data are excluded.

These results indicate that within feasible ranges where steady penetration by uCPT will be partially drained, permeability magnitudes may be recovered directly from cone measured metrics recovered during active penetration. The proposed evaluation of

permeability, *on-the-fly*, requires that the penetration is partially drained, and the pore pressure distribution has reached a dynamic steady state. Notably, this analysis is not applicable for suspected dilatant silts that return negative pore pressures during penetration. The extensive suite of independently measured permeability profiles enabled validating of permeability evaluated from the *on-the-fly* method. These analyses show that the relation $K_D = 1/(B_q Q_t)$ exhibits promise as a practical means of prediction of fine-scale permeability structure within feasible ranges where the penetration response is both partially-drained and steady.

In addition, related solutions have been applied to the problem of defining the pore fluid pressure field that develops around a penetrometer that self-embeds from freefall into the seabed (Appendix A).

This thesis comprises a series of five papers either published or in-submittal in journals. In chronological order these papers are:

1. Lee, D.S., Elsworth, D., Hryciw, R.D., and Butler, Jr. J.J. (2006). Hydraulic conductivity measurement from the-on-fly uCPT sounding and from VisCPT

2. Lee, D.S., Elsworth, D., Butler, Jr. J.J., and Dietrich, P. (2006). Direct Evaluation of Permeability from uCPT Soundings: Validation against Data from the Nauen Test Site, Germany

3. Elsworth, D., Lee, D.S., Hryciw, R.D., and Shin, S.C. (2005). Pore pressure response following undrained uCPT sounding in a Dilating Soil ASCE Journal of Geotechnical and GeoEnvironmental Engineering (in press).

4. Elsworth, D. and Lee, D.S. (2005). Limits of Determining Permeability from On-

the-fly CPT Sounding - Geotechnique (under review).

5. Lee, D.S. and Elsworth, D (2004). Indentation of a Free-Falling Sharp Penetrometer into a Poroelastic Seabed - ASCE Journal of Engineering Mechanics Vol 130, No 2. 170 - 179.

Table of Contents

Chapter 3: Pore Pressure Response Following Undrained uCPT Sounding in a Dilating

List of Tables

List of Figures

Acknowledgements

It has been my great honor and privilege to learn scientific thinking from my advisor, Dr. Derek Elsworth. I have learned the art of performing engineering and presenting it in an exciting manner. His enthusiasm and strong motivation to explore demanding questions has greatly shaped and broadened my perspective of engineering. Thanks to him, I feel confident in accepting engineering challenges and venturing into new fields of research. His words of encouragement always motivated, inspired, and helped me view matters from a different perspective. I am most grateful and indebted to him for the large doses of guidance, patience, and encouragement he has shown me during my time here at Penn State.

With all my heart, I would like to thank Dr. Roman Hryciw (University of Michigan) and Dr. James J. Butler (Kansas Geological Survey) for locating the important data, guidance, support, and engineering advice. Their willingness to educate me to understand the fundamental concepts of research will always remain with me. I am very grateful to all my committee members, Dr. Abraham S. Grader, Dr. Peter B. Flemings, and Dr. Chris J. Marone for their helpful discussions and guidance.

I am very thankful to Michael Fitzgerald, Seungcheol Shin (University of Michigan), Youngsub Jung (University of Michigan), and Steve Knobbe (GeoProbe) who assisted with the field measurements. I am very thankful to the past and present 131A Hosler office members, Marielle Narkiewicz, Joshua Taron, Jose Zaghloul, and Phillip Bower. I would like to especially thank Dr. Hideaki Yasuhara (Ehime University, Japan) for friendship and enlightening discussions on a wide variety of research topics. I am very

grateful to all my friends and colleagues in the department of Energy and Geo-Environmental Engineering for their friendship, help, and support. They certainly made Penn State to be the most exiting place to carry out research.

My family has provided me with a tremendous amount of encouragement and love during my time in graduate school. I am indebted to my wife, So Jeong Kim, and my daughter Ellie Lee for their love and support. I am also indebted to my family and So Jeong's family for their endless love and encouragement. I am grateful to them for teaching me the value of optimism.

Chapter 1: Limits in Determining Permeability from On-the-fly uCPT Sounding

Abstract

Limits are defined for the transition from partially drained to undrained penetration during uCPT testing. These limits prescribe the range of cone metrics for which coefficient of permeability magnitudes may be recovered from peak pore pressure data, on-the-fly. The transition from partially drained to undrained behavior is defined through the traditional non-dimensional metrics of cone resistance, Q_t, sleeve friction, F_r, and pore pressure ratio, B_q, together with the undrained shear strength, S_u, normalized by shear modulus, G, and in situ effective stress, σ_{v0}'. For plausible ranges of S_u/σ_{v0}' and G/S_u, the lower bound for transition from partial drainage is defined by the uCPT metric products and ratios of $B_q Q_t < 1.2$, $Q_t F_r < 0.3$, and $B_q/F_r < 4$, with the first and last proving the best determinant of drainage condition. Standard (2 *cm/s*) uCPT data together with independently measured permeabilities identify the transition from partially drained to undrained conditions at permeability magnitudes of-the-order of 10^{-5} *m/s*. These results are used to define limits of partial drainage where peak tip pore pressures may be used to recover in situ permeability profiles. For conditions of partial drainage, non-dimensional permeability K_D is defined independently in terms of cone metrics as $K_D = 1/B_q Q_t$ (with $B_q Q_t < 1.2$), enabling permeability to be recovered during standard penetration for $k > 10^{-5}$ *m/s*. Where stress conditions at the cone tip are additionally assumed, permeability may also be dependently defined in terms of the metric product $Q_t F_r$ and the ratio

B_q / F_r, although these parameters prove less robust in determining permeability. Where undrained data are excluded, non-dimensional permeability, K_D, is optimally defined as

$$K_D = 0.62 / (B_q Q_t)^{1.6}.$$

1.1   Introduction

Piezocone sounding (uCPT) is a rapid, minimally invasive and inexpensive method for determining the mechanical and transport properties of soil types, their distribution in space, and the type and distribution of the soil-saturants (Campanella and Robertson 1988; Mitchell and Brandon 1998). In determining soil transport properties, the absolute magnitude or rate of decay of penetration-generated excess pore fluid pressures are recorded, and correlated with the coefficient of consolidation, of the soil, and via estimates of soil compressibility, with permeability. Current data reduction techniques may be divided broadly between methods that employ empirical correlations, and those that measure the generation or dissipation of pore fluid pressures, at the cone tip, face, or sleeve, either concurrent with penetration or after penetration-arrest. The latter include pump-type fluid injection tests.

Empirical predictions link recorded magnitudes of cone end-bearing, friction ratio, and induced pore pressures with classifications of soils by grain size and type (Douglas and Olsen 1981; Robertson et al. 1986). These classifications may be used to estimate permeability coefficients directly from inferred soil type (Douglas and Olsen 1981; Manassero 1994), or may be further constrained by in situ imaging and the use of capillary models (Hryciw et al. 2003). Alternative methods involve estimating coefficient of permeability directly from end-bearing (Chiang et al. 1992; Smythe et al. 1989) when

sleeve friction is known.

Permeabilities may also be evaluated from uCPT-measured pore pressures. The coefficient of consolidation may be evaluated from dissipation rate following cone arrest, provided magnitudes of drained soil compressibility are also available. Several methods are used to calculate coefficient of consolidation (Levadoux and Baligh 1986). All require that a pre-arrest pore pressure distribution may be determined. Most assume undrained loading for this evaluation, and incorporate cavity expansion (Burns and Mayne 1998; Torstensson 1977) or strain path models (Baligh 1985; Baligh and Levadoux 1986; Danziger et al. 1997; Levadoux and Baligh 1986; Teh and Houlsby 1991) to define initial pore pressure distributions that may subsequently dissipate to background levels.

These evaluations compare well with field (Baligh and Levadoux 1986; Levadoux and Baligh 1986) and calibration chamber (Kurup et al. 1994) results. Predictions of induced strain fields and pore pressure magnitudes from complex (Baligh and Levadoux 1986) and simple material models (Teh and Houlsby 1991) compare well with more rigorous representations of finite strain continuum behavior for clays (Kiousis and Voyiadjis 1985; Voyiadjis and Abu-Farsakh 1997; Voyiadjis and Song 2000), sands (Cividini and Gioda 1988) and clays to sands (Berg. 1994). For linear soil behavior, a variant of these methods may be applied to account for partial drainage in an effective stress analysis (Elsworth 1991; Elsworth 1993; Elsworth 1998) and this yields similar results to those from strain path and continuum models. Permeabilities are determined from consolidation coefficients via empirical estimates of soil compressibility. These estimates have a wide range, yielding estimates of permeability that exhibit similar wide range (Lunne et al. 1997). Other direct correlations of coefficient of consolidation with

coefficient of permeability exist (Schmertmann 1978) but are not broadly confirmed either by data (Robertson et al. 1992), or on functional grounds.

For on-the-fly evaluations(Elsworth 1990; Elsworth and Lee 2005), permeabilities are evaluated from the magnitudes of peak pore pressures recorded at the penetrometer tip, or face. When pore pressures are generated around the cone tip and dissipate concurrently (as in sands), the behavior may be viewed as a controlled strain-rate test. The magnitude of the steady pore fluid pressure is controlled by competition between the strain rate that generates excess pore pressure, and permeability that dissipates it. Low permeabilities impede drainage and result in the generation of high excess pore pressures. The generation and concurrent dissipation of pore pressures around a blunt penetrometer may be represented by simple linear poroelastic models (Elsworth 1990; Elsworth 1991; Elsworth 1992; Elsworth 1993), but may also be evaluated using models representing the tapered form (Elsworth 1998) of the tip and more realistic constitutive parameters (Elsworth and Lee 2005; Song et al. 1999; Voyiadjis and Song 2000; Voyiadjis and Song 2003).

Regardless of the method used, functional relations result that link permeability, K, with penetration rate, U, and reciprocal excess pore pressure at the tip, $p - p_s$, relative to the static pore pressure magnitude, p_s, as $K \propto U/(p - p_s)$. This latter method is attractive because sounding is not interrupted to measure permeability, and the correlation with permeability is direct – no *a priori* measurement of soil compressibility is needed. However, a principal requirement in recovering permeabilities from peak pressure data is that penetration is partially drained - undrained measurements will provide information of soil strength and deformability, only. In the following we first develop a rationale to

discriminate between undrained and partially drained response, using cone metrics alone, and then provide methods to recover permeability magnitudes from *bona fide* partially drained data.

1.2   Mechanical Response

Permeability magnitudes may be recovered from tip-local pore pressure response only if the behavior is partially-drained (Elsworth and Lee 2005). If undrained, the penetration-induced pore pressures represent the strength and deformability characteristics of the soil, alone (Bai and Elsworth 2000), and provide no useful information on transport characteristics. Correspondingly, we desire to discriminate between partially-drained and undrained loading, using cone metrics, to determine regimes where permeability magnitudes may be confidently recovered.

1.2.1   Cone Metrics

uCPT sounding yields profiles of cone resistance, q_t, excess pore pressures, $p - p_s$, and sleeve friction, f_s, with depth. These dimensional metrics may be recast as normalized magnitudes of tip resistance, Q_t, pore pressure ratio, B_q, and friction ratio, F_r, as

$$Q_t = \frac{q_t - \sigma_{v0}}{\sigma_{v0}'}; \quad B_q = \frac{p - p_s}{q_t - \sigma_{v0}}; \quad F_r = \frac{f_s}{q_t - \sigma_{v0}} \qquad (1.1)$$

where σ_{v0} is the initial *in situ* vertical stress, p_s, the initial *in situ* pore pressure, and the prime denotes effective stress.

1.2.2 Cavity Expansion Solutions

Loading is most likely to be undrained as soils become progressively more cohesive, and this case is selected in the following. Limits may be placed on end-bearing and sleeve friction stresses, and on pore fluid pressures that may be developed during undrained penetration by considering cavity expansion solutions. Where a spherical cavity is expanded within an ideal elastic perfectly-plastic soil $(c = S_u; \phi = 0)$ from nominal radius to final radius, a, with no net volume change at failure $(\Delta V = 0; \nu = 0.5)$, as shown in Figure 1.1, the resulting radial σ_r and tangential σ_θ stresses adjacent to the cavity wall are recorded as (Hill 1983)

$$\sigma_r = \sigma_{v0} + \frac{4}{3} S_u [1 + \ln(G/S_u)] \tag{1.2}$$

$$\sigma_\theta = \sigma_{v0} + \frac{4}{3} S_u [1 + \ln(G/S_u)] - 2S_u \tag{1.3}$$

where G is the shear modulus. These stresses are overprinted on the initial pre-expansion total stress, σ_{v0}, assumed uniform in vertical and horizontal directions. Cavity expansion stress, q_t, may be approximated from equation (1.2) as

$$q_t = \sigma_r = \sigma_{v0} + \frac{4}{3} S_u [1 + \ln(G/S_u)], \tag{1.4}$$

although this typically acts as a lower-bound to observations (Konrad and Law 1987). The undrained pore pressures, $p - p_s$, generated during cavity expansion may be determined from the changes in mean total stress, $\Delta\sigma_m = \frac{1}{3}(\Delta\sigma_r + 2\Delta\sigma_\theta)$, and deviatoric total stress, $\Delta\sigma_d = \Delta\sigma_r - \Delta\sigma_\theta$, via the pore pressure relation, $p - p_s = B\Delta\sigma_m + B\bar{A}\Delta\sigma_d$, where B and $\bar{A}$ are the pore pressure coefficients (Skempton 1954). For saturated conditions we assume $B = 1$ and set $\bar{A}$ to zero, as a first assumption. From this, the
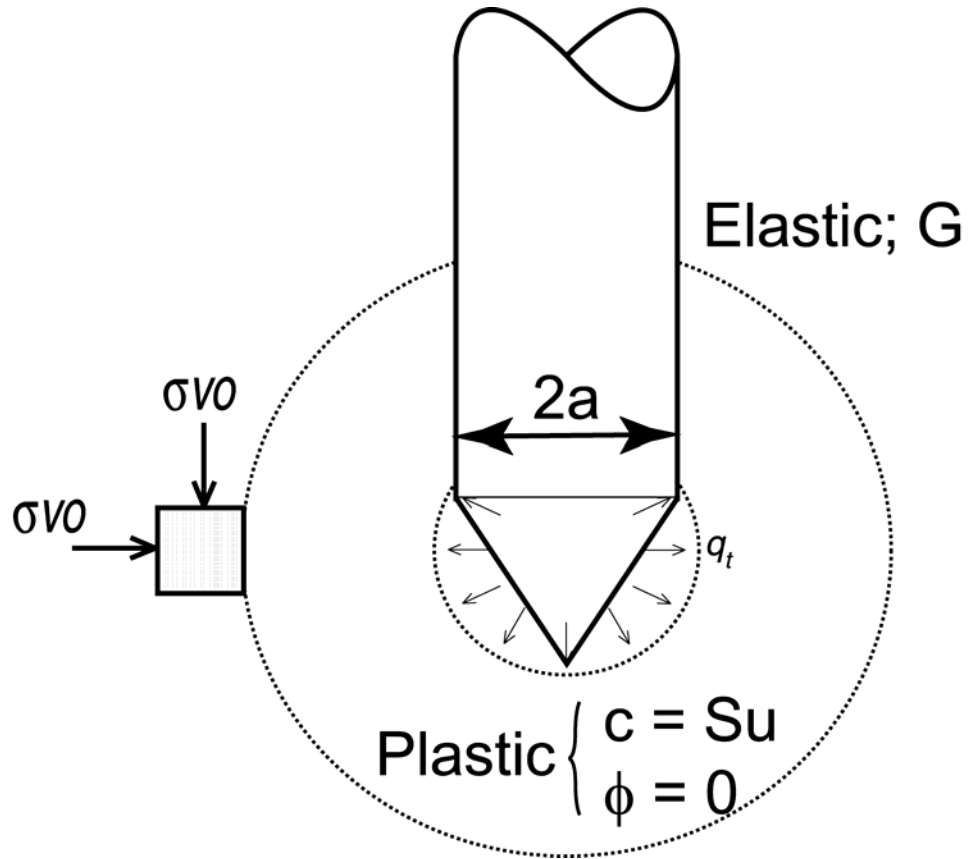
Figure 1.1: Geometry for spherical expansion of a cavity of diameter, $2a$, in a cohesive soil $(c = S_u; \phi = 0)$ with uniform far-field total stress, σ_{v0}.

excess pore pressure is recovered as,

$$p - p_s = \tfrac{1}{3}(\Delta\sigma_r + 2\Delta\sigma_\theta) = \tfrac{4}{3}S_u \ln(G/S_u) \tag{1.5}$$

representing the pressure induced and recorded at the cone face. If the adhesion of the cone sleeve is assumed equal to the undrained shear strength, $f_s = S_u$, then the magnitudes of non-dimensional cone metrics of end-bearing, sleeve friction, and pore pressure ratio may be determined by substituting equations (1.4) and (1.5) into equation (1.1) to yield

$$B_q = \frac{p - p_s}{q_t - \sigma_{v0}} = \frac{\ln(G/S_u)}{1 + \ln(G/S_u)} \tag{1.6}$$

$$Q_t = \frac{q_t - \sigma_{v0}}{\sigma_{v0}'} = \frac{4}{3}\frac{S_u}{\sigma_{v0}'}[1 + \ln(G/S_u)] \tag{1.7}$$

$$F_r = \frac{f_s}{q_t - \sigma_{v0}} = \frac{1}{\tfrac{4}{3}[1 + \ln(G/S_u)]} \tag{1.8}$$

These relations enable regions of undrained penetration to be denoted on plots of cone metrics typically used for soil classification, similar to Figure 1.2. This Figure defines a form of "stress path," shown schematically by the trajectory of point (1) through (3) in Figure 1.2. As penetration initiates at point (1), the tip resistance, Q_t, and pore pressure ratio, B_q, are limited by the "failure envelope" at point (3). If the penetrated medium has a high permeability, undrained conditions may not be reached, and the resulting tip-local stress and pressure conditions will correspond to the dynamic steady state of point (2). This condition represents the condition of partial drainage where the rates of pore fluid pressure development and dissipation exactly cancel, enabling permeabilities to be evaluated from the peak pore pressure magnitude (Elsworth 1993; Elsworth and Lee 2005).
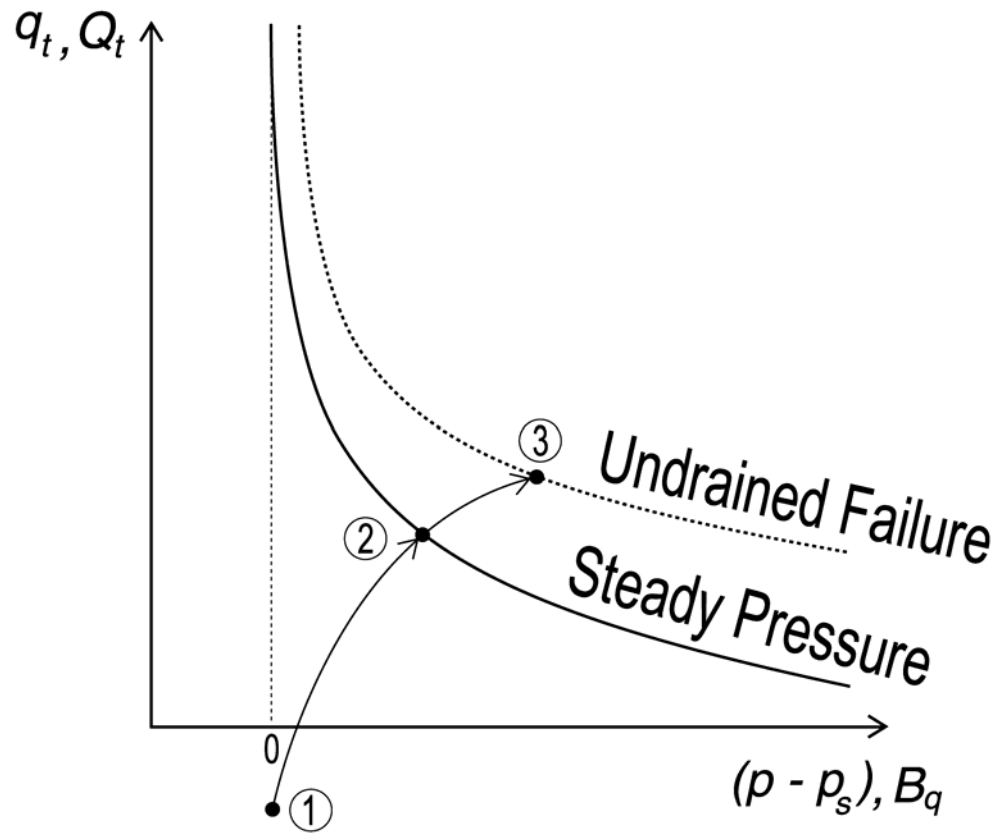
Figure 1.2: Schematic plot of normalized tip resistance, log Q_t, to pore pressure ratio, B_q, showing the stress path taken as penetration is initiated. Penetration initiates at (1) and may transit via (2) to undrained failure (3). If the material is granular, with relatively high permeability and high strength, penetration may be partially-drained, resulting in the development of steady fluid pressure at the penetrometer tip (2).

Where penetration is undrained, the resulting cone response is controlled by the strength of the soil alone, and generated pore pressures represent only this process, and provide no information on soil permeability. These relations may be determined for the usual plots of $Q_t - B_q$ and $Q_t - F_r$, and the less commonly used plot of $B_q - F_r$, by combining equations (1.6) to (1.8) as

$$B_q Q_t = \frac{4}{3} \frac{S_u}{\sigma_{v0}'} \ln(G/S_u) \qquad (1.9)$$

$$Q_t F_r = \frac{S_u}{\sigma_{v0}'} \qquad (1.10)$$

$$\frac{B_q}{F_r} = \frac{4}{3} \ln(G/S_u) \qquad (1.11)$$

For typical magnitudes of $S_u/\sigma_{v0}' \sim 0.3 \text{ to } 0.7$ and $G/S_u \sim 20 \text{ to } 400$, equations (1.9) through (1.11) yield bounds on the transition from undrained to partially drained behavior as $B_q Q_t < 1.2 \text{ to } 5.6$, $Q_t F_r < 0.3 \text{ to } 0.7$, and $B_q/F_r < 4 \text{ to } 8$. These bounds are illustrated in Figure 1.3, isolating cone sounding metric products and ratios consistent with undrained behavior, and by inference defining regions representing partially-drained penetration.

These regions alone can be used to define whether permeability magnitudes may be evaluated from cone sounding metrics on-the-fly. Data are included that represent penetration under both presumed partially-drained and undrained conditions; conformity to either of these modes is conditioned by the magnitudes of in situ permeability, reported in Table 1.1. Under standard penetration at 2 *cm/s*, the transition from partial-drainage to undrained behavior is expected to index directly with measured in situ permeability. Permeabilities decrease from the order of 10^{-3} to 10^{-5} m/s for sand and silts at Treasure
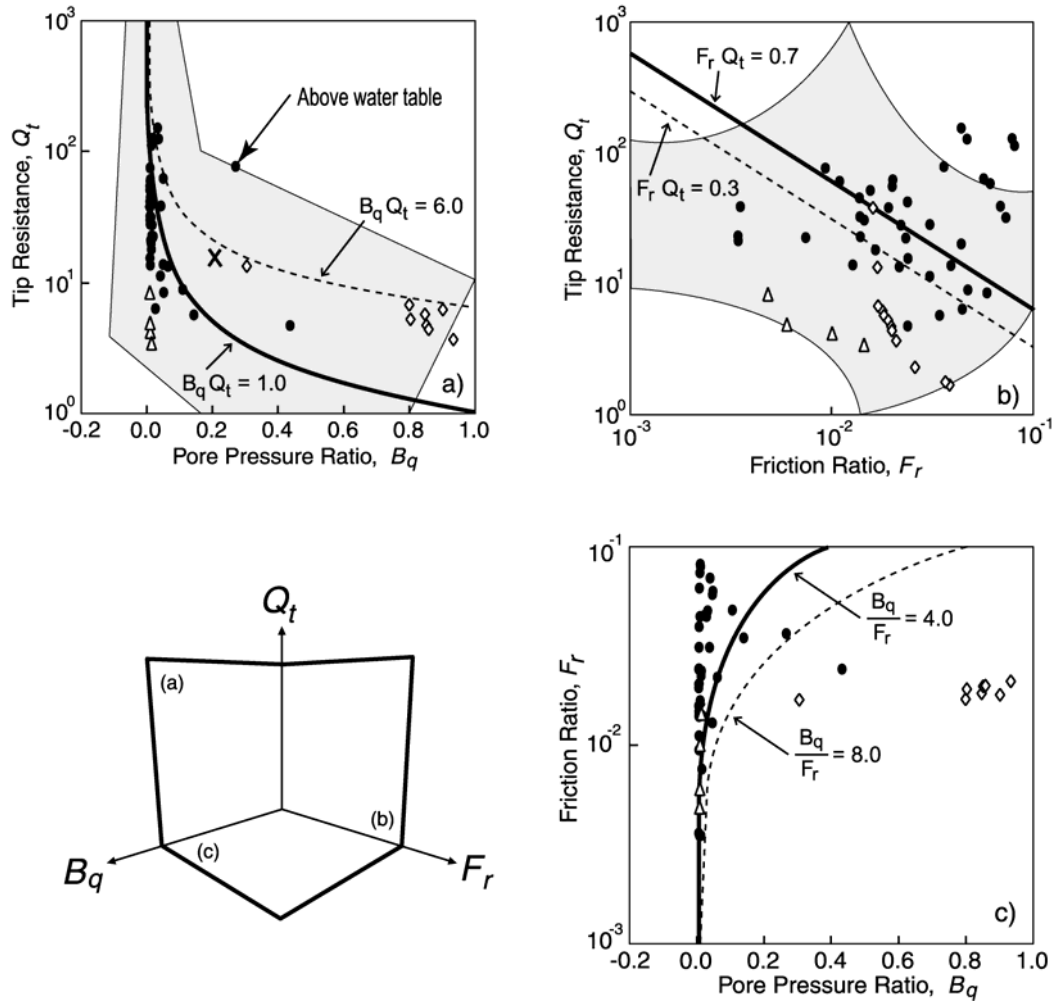
Figure 1.3: Plots of cone metrics (a) $Q_t - B_q$, (b) $Q_t - F_r$, and (c) $F_r - B_q$ with the lower limits (range of transition given by solid and dashed lines) of undrained penetration identified. Shaded regions in (a) and (b) denote defined ranges of material types (Robertson 1990). Symbols denote data from varved clays at the NGES Amherst, MA, test site (diamonds), tailings slimes at Tyrone, NM, (cross), and sands and silts at Treasure Island, CA, (triangles), and at the Savannah River Test Site, Aiken, SC, (filled circles). See Table 1.1 for details.

Island, CA, and Savannah River, Aiken, SC, through silts of Tyrone, NM, to magnitudes of 10^{-9} m/s in varved clays at Amherst, MA. This transition in drainage condition is best honored by the metrics of $B_q Q_t$ and B_q / F_r apparent in Figure 1.3 (a) and (c), exhibiting a sharp contrast between partially drained and undrained behavior. The metric $Q_t F_r$, shown in Figure 1.3 (b), is less definitive in defining this transition. The boundaries between drained and undrained behavior, apparent in Figures 1.3 (a) and (b), transect the soil facies types noted in related correlations by (Robertson 1990). Notably, these observations are not contradictory, since although a single facies may have relatively tightly constrained mechanical attributes of strength, permeabilities may vary over multiple orders of magnitude. Since permeability therefore exerts the principal influence on the degree of drainage experienced under standard penetration, it is reasonable that one facies type could behave as either drained, or undrained, depending on the permeability.

1.3   Permeability from Steady Hydraulic Response

With the limits defined that represent the transition from undrained to partially-drained behavior, it is possible to first isolate the data that conform to partial drainage, and to then use these data alone to determine permeability magnitudes. A relation is required that links in situ permeability magnitudes to measured steady tip pore pressures.

1.3.1   Hydraulic Methods

Hydraulic methods require that a relation can be defined that links the tip-local permeability with the penetration-induced pore pressure. Assuming that the moving cone displaces a volume of fluid per unit time equivalent to the insertion volume of the cone,

that this source dissipates roughly spherically, and that there is little fluid storage in the system, enables the induced pore pressures to be evaluated (Elsworth and Lee 2005) as (Figure 1.4),

$$\frac{p - p_s}{\sigma_{v0}'} = \frac{Ua\gamma_w}{4K\sigma_{v0}'} = \frac{1}{K_D} \tag{1.12}$$

where U is the rate of penetrometer advance, a, is the penetrometer radius (synonymous with the cavity expansion radius defined earlier), γ_w is the unit weight of water, and K is the coefficient of permeability, or hydraulic conductivity. As apparent in equation (1.12), permeability is related to a non-dimensional permeability, K_D. Noting that $p - p_s / \sigma_{v0}' = B_q Q_t$ (equation (1.1)) yields a single relation linking the cone metrics of end-bearing and pore pressure ratio, as,

$$K_D = 1/B_q Q_t \tag{1.13}$$

enabling permeability to be directly evaluated from cone metrics, provided they are recorded during partially-drained penetrometer drivage.

The permeability relation of equation (1.13) is applicable only where penetration is partially drained, with this threshold similarly defined uniquely in terms of $B_q Q_t$ as equation (1.9). Correspondingly, admissible cone data that are both partially-drained, and for which permeability may therefore be evaluated from $K_D = 1/B_q Q_t$, are identified in Figure 1.5. The same suite of data shown in Figure 1.3 are included, together with additional data for which only composite magnitudes of the product $B_q Q_t$ are reported (Voyiadjis and Song 2003). Again, the degree of drainage under standard penetration will be indexed to permeability, reported in Table 1.1. The threshold undrained behavior is apparent for permeabilities lower than about 10^{-5} to 10^{-6} *m/s* ($K_D < 10^0$ to 10^{-1}), as
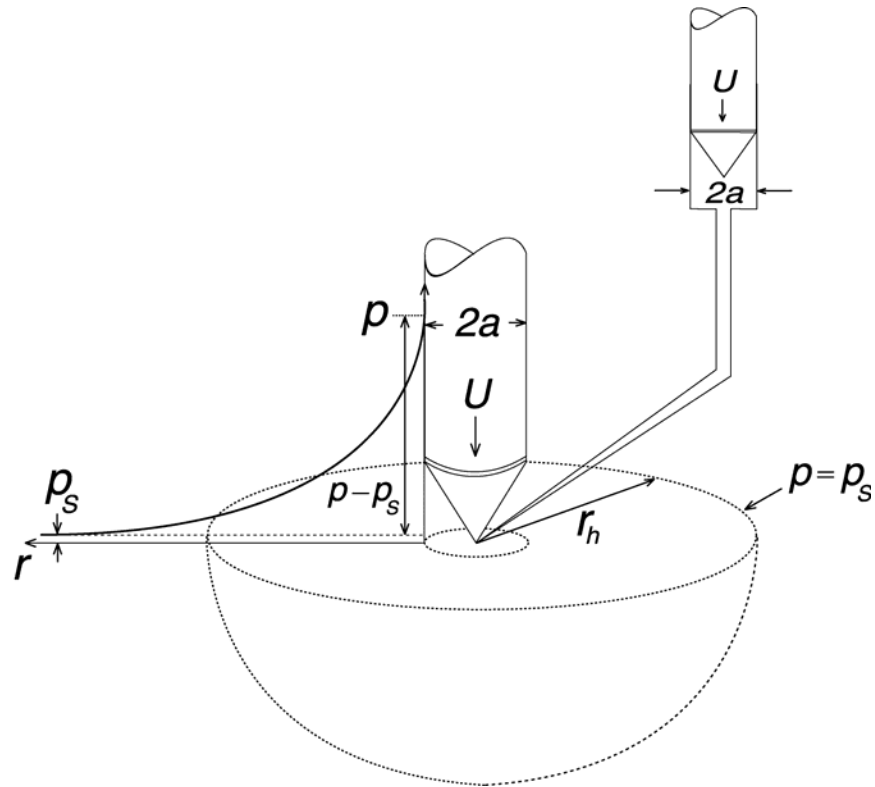
Figure 1.4: Flow geometry local to the penetrometer tip. In partially drained penetration, the pore pressure is elevated at the center of the spherical shell to p relative to the far-field pressure, p_s.
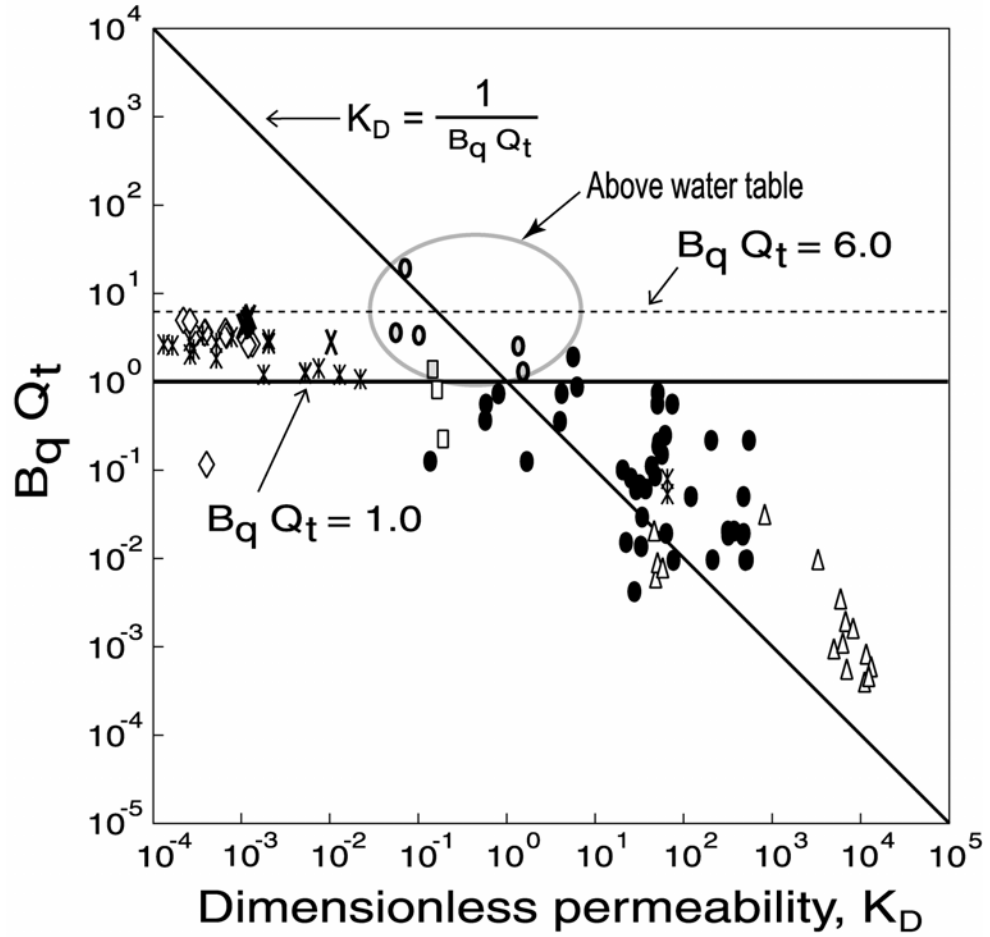
Figure 1.5: Threshold magnitudes of excess pore pressure, $p - p_s / \sigma_{v0}' = B_q Q_t = 1/K_D$ relative to independently measured non-dimensional permeability, K_D, for data from sites at Amherst, MA (diamonds), Tyrone, NM (cross), Opelika, GA (box), Savannah River, SC (circles), Treasure Island, CA (triangles), and Various (star). See Table 1.1 for details.

Table 1.1. Permeability magnitudes reported for cone metric data reported in Figures 1.3, 1.5 and 1.7.

Location	Reported Permeability (m/s)	Soil Characteristics	Presumed Drainage Characteristics	Source
Amherst, MA	3.0×10^{-9} ~ 4.0×10^{-9}	Normally consolidated varved clay	Undrained	DeGroot & Lutenegger, 1994 Mayne, 2001
Tyrone, NM	1.0×10^{-8} ~ 7.4×10^{-8}	Silty clay	Undrained	Personal communication
Opelika, GA	3.5×10^{-7} ~ 1.5×10^{-6}	Residual silts and fine sands	Partially-drained	Finke, et al, 2001
Savannah River, Aiken, SC	1.0×10^{-5} ~ 1.0×10^{-3}	Silts and sands	Partially-drained	Personal communication
Treasure Island, CA	1.0×10^{-4} ~ 0.5×10^{-4}	Sand hydraulic fill	Partially-drained	National Geotechnical Experimentation Sites
Various	3.6×10^{-10} ~ 9.0×10^{-3}	Clay to sand	Partially-drained through Undrained	Voyiadjis & Song, 2003

References

1. DeGroot, D.J. and Lutenegger, A.J. (1994). "A comparison between field and lab measurements of hydraulic conductivity in a varved clay." Hydraulic conductivity & waste contaminant transport in soil (STP 1142), ASTM, West Conshohocken, PA, 300-317.

2. Mayne, P. W. (2001). "Stress-strain-strength-flow parameters from enhanced in-situ tests", Proceedings, International conference on in-situ measurement of soil

properties & case histories [In-Situ 2001], Bali, Indonesia, May, 27-48.

3. Voyiadjis, G. Z. and C. R. Song (2003). "Determination of hydraulic conductivity using piezocone penetration test." International Journal of Geomechanics **3**(2): 217-224.

4. Finke, K.A., Mayne, P.W., and Klopp, R.A. (2001). "Piezocone penetration testing in Atlantic piedmont residuum" Journal of Geotechnical and Geoenvironmental Engineering, Vol. 127, No, 1, 48-54.

reported earlier. This is signified by the plateau in $B_q Q_t$ data, in the range $10^0 < B_q Q_t < 10^1$. However, in addition, a preliminary correspondence is apparent between the data representing partial drainage, and the relation $K_D = 1/B_q Q_t$ reported in equation (1.13), and also shown on the Figure. The fidelity of this match will be discussed later.

1.3.2 Mechanical Methods

Evaluations of permeability from penetrometer data may be further constrained through consideration of consistent models for the generation of penetrometer end-bearing and sleeve friction, which have a mechanistic basis. These models rely on basic assumptions of stress changes that develop around the penetrometer tip, concurrent with penetration. Two assumptions are selected, as illustrated in Figure 1.6. The first is that vertical total stresses in the tip process zone remain invariant with penetration (Figure 1.6 (b)), as $\Delta\sigma_v = 0$ or $\sigma_v = \sigma_{v0}$. The second is that horizontal stresses immediately behind the penetrometer tip are limited to the cavity expansion stress (Figure 1.6 (c)), as $\sigma_h = q_t$. These conditions are examined separately in the following, enabling dependent relations to be developed that link in situ permeability with either constraints on sleeve friction, or on end-bearing, respectively.

1.3.2.1 Vertical Stresses Remain Invariant

For a frictional soil, where the cohesion has been destroyed by large deformations, the sleeve friction, f_s, may be defined as $f_s = (\sigma_h - p)\tan\phi$. Consistent with the destruction of cohesion in the process zone, the Mohr-Coulomb strength criterion may be
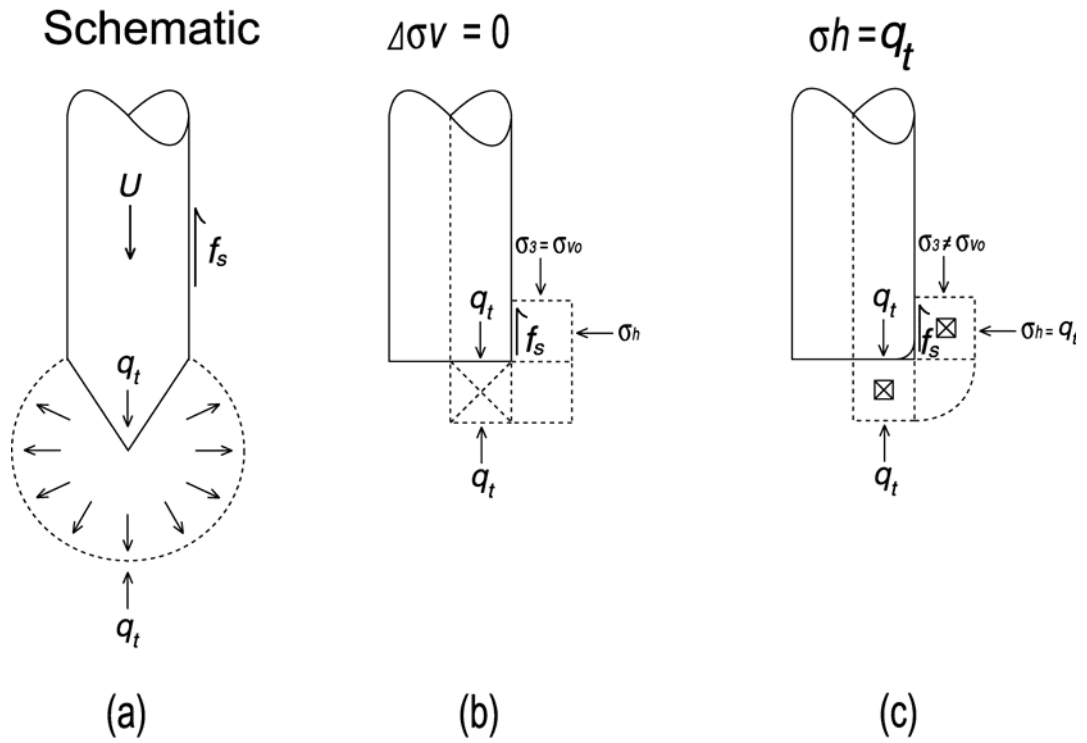
Figure 1.6: Actual (a), and assumed ((b) & (c)) limiting magnitudes of stresses beneath the tip of a blunt indentor, assuming that within the tip process zone, either (b) vertical stresses remain unchanged $(\Delta\sigma_{v0} = 0)$, or (c) horizontal stresses are limited to the tip expansion stress, $(\sigma_h = q_t)$. Squares inscribed with crosses represent conjugate failure planes.

defined in terms of principal stresses as $\sigma_1' = N\sigma_3' + 2c\sqrt{N}$ which for $c = 0$ reduces to $\sigma_1' = N\sigma_3'$ where $N = (1+\sin\phi)/(1-\sin\phi)$, and ϕ is the angle of internal friction of the soil. The internal frictional resistance, and the angle of interface friction are considered the same. Simple considerations of lower bound perfect plasticity, as identified in Figure 1.6 (b), yield magnitudes of sleeve friction, F_r, as

$$F_r = N\tan\phi[\frac{1}{Q_t} - B_q]$$ (1.14)

and end bearing, Q_t, as,

$$Q_t = \frac{1}{[\frac{1}{N^2-1} + B_q]}$$ (1.15)

where all parameters are as previously defined.

Equations (1.14) and (1.15) represent separate and independent equations, the first defining sleeve-friction in terms of the other cone metrics, and the second defining end-bearing, again relative to consistent complimentary cone metrics. These relations may be substituted with the permeability relation $K_D = 1/B_q Q_t$, to alternately remove B_q and Q_t, and to define permeability as a function of only two of the three possible cone metrics. This is completed sequentially for sleeve-friction, and then for end-bearing.

Sleeve-Friction: Permeability relations recovered from sleeve-friction are obtained by substituting equation (1.14) with (1.13) to yield

$$\frac{F_r}{B_q} = N\tan\phi(K_D - 1)$$ (1.16)

when Q_t is eliminated, and alternatively

$$Q_t F_r = N \tan \phi (1 - \frac{1}{K_D}) \tag{1.17}$$

when B_q is eliminated. Importantly, once rearranged, equations (1.16) and (1.17) define non-dimensional permeability as a function of the same cone metric groups that index the transition from undrained to partially-drained behavior. Importantly, these relations are dependent on the fundamental assumption of a steady fluid flow field (equation (1.13)), and provide only a dependent evaluation of permeability, albeit for other parameter groupings. These relations are shown in Figure 1.7 for the three suites of parameter groups: $B_q Q_t$ (equation (1.13)) defined previously (Figure 1.5), and $Q_t F_r$ (equation (1.17)) and F_r / B_q (equation (1.16)), each defined as a function of non-dimensional permeability, K_D. These are discussed later.

End-Bearing: For completeness, the permeability relations for end-bearing are recovered where the magnitude of end-bearing (equation (1.15)) is substituted by the permeability relation of equation (1.13) to yield

$$K_D = 1 + \frac{1}{(N^2 - 1)B_q} \tag{1.18}$$

when Q_t is eliminated, and

$$K_D = \frac{1}{[1 - Q_t /(N^2 - 1)]} \tag{1.19}$$

when B_q is eliminated. These expressions appear less useful than those determined from limits on sleeve-friction, as they are not obvious functions of the same cone metric products and ratios that modulate the transition from undrained to partially-drained loading.
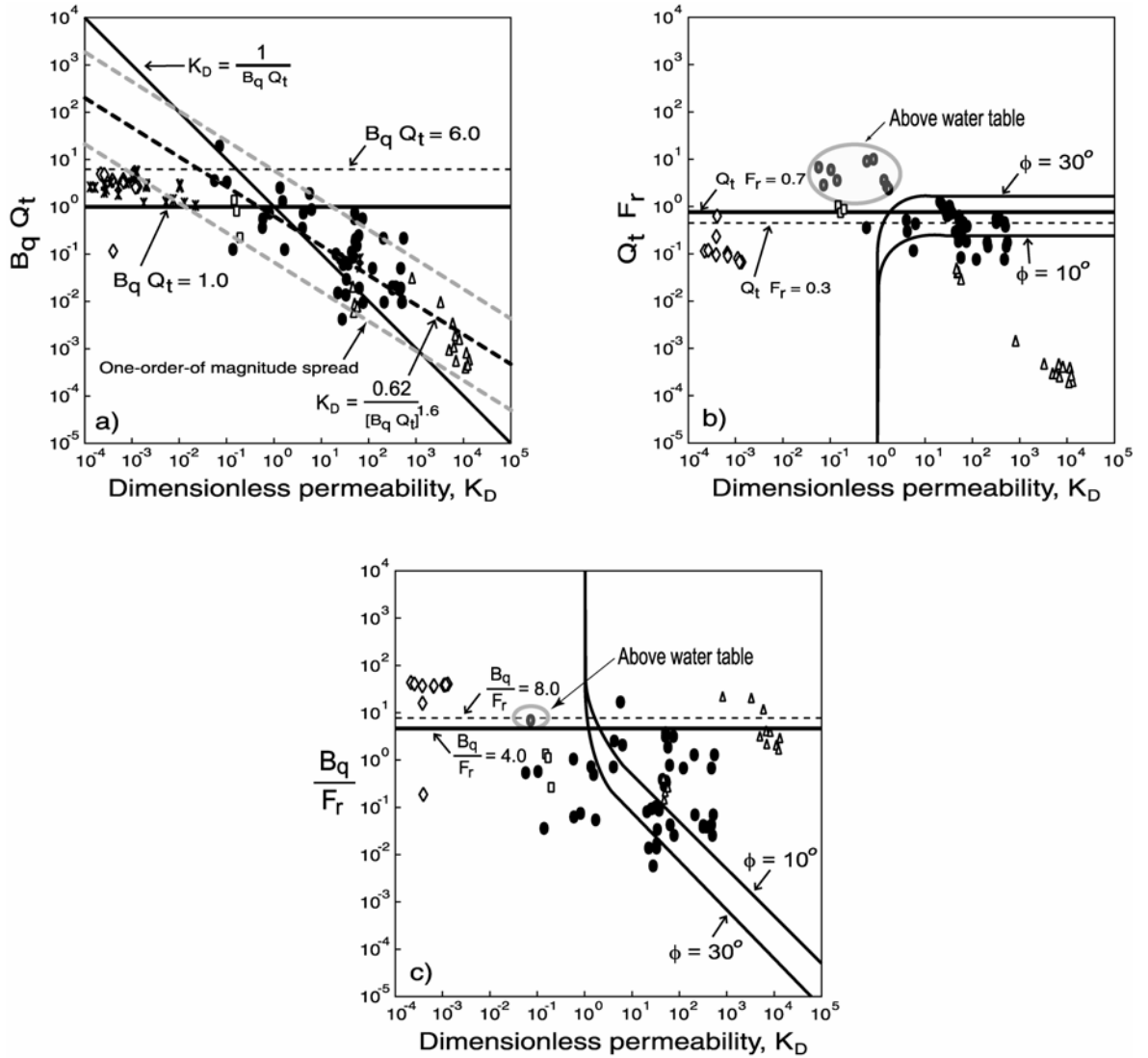
Figure 1.7: Plots of cone metric products (a) B_qQ_t and (b) Q_tF_r, and the ratio (c) B_q/F_r with independent measurements of non-dimensional permeability, K_D. Figures identify both the transition from partially drained to undrained behavior, and prospective relations for permeability, with data from the locations noted in Table 1.1. Amherst, MA (diamonds), Tyrone, NM (cross), Opelika, GA (box), Savannah River, SC (circles), Treasure Island, CA (triangles), and Various (star). See Table 1.1 for details.

1.3.2.2 Horizontal Stresses Limited to Cavity Expansion Stress

Where horizontal stresses are limited to the cavity expansion stress, as $\sigma_h = q_t$, then similar relations may be built for sleeve-friction as

$$F_r = \tan\phi[1 + \frac{1}{Q_t} - B_q] \qquad (1.20)$$

and also for end-bearing (not reported here), if a relation is prescribed to define the cavity expansion stress as a function of material properties (Vesic 1972). The prior result (equation (1.20)) follows directly from the assumption that $\sigma_h = q_t$, and a similar substitution may be made for permeability magnitudes through the incorporation of equation (1.13) into equation (1.20). This yields

$$K_D = \frac{1}{B_q}[\frac{F_r}{\tan\phi} - 1 + B_q] \qquad (1.21)$$

where Q_t is eliminated, and

$$K_D = \frac{1}{Q_t[1 + \frac{1}{Q_t} - \frac{F_r}{\tan\phi}]} \qquad (1.22)$$

where B_q is eliminated. Where lateral stresses are prescribed as equivalent to the cavity expansion stress, as $\sigma_h = q_t$, then the predictions of permeability, constrained by sleeve friction (equations (1.21) and (1.22)) are identical to those reported elsewhere (Elsworth and Lee 2005). Equation (1.20) has been shown to significantly underestimate frictional strength from uCPT sounding data (Lee et al. 2004). Despite this shortcoming, permeability predictions from $B_q - F_r$ data (equation (1.21)) have been shown satisfactory, although those from $Q_t - F_r$ data (equation (1.22)) have not

performed so well (Elsworth and Lee 2005). Correspondingly, these characterizations are not pursued further.

1.4   Discussion

Where tip-local stresses are constrained by perfect lower bound plasticity for a frictional soil, dependent relations may be developed to define permeability as functions of uCPT metrics. These relations are further constrained by the operational assumptions that either vertical stresses remain invariant $(\Delta\sigma_v = 0)$, or that peak lateral stresses approach the cavity expansion stress $(\sigma_h \sim q_t)$. This latter assumption significantly overestimates lateral stresses (Lee et al. 2004), and is not considered further. Conversely, where vertical stresses are assumed invariant, reasonable predictions of frictional resistance are recovered from uCPT sounding data (Lee et al. 2004). Assuming that vertical stresses do not change, enables separate dependent relations to be constructed that define permeability from soundings conducted on-the-fly, that supplement the single independent relation $K_D = 1/B_q Q_t$ (equation (1.13)). These result from constraints on both sleeve friction (equations (1.16) and (1.17)), and on end bearing (equations (1.18) and (1.19)). Although either suite of relations may be used to recover permeabilities, those derived from constraints on sleeve friction are most useful as they directly incorporate the metrics that describe the limits on partially-drained behavior, namely the product $Q_t F_r$ and the ratio B_q / F_r.

These relations are shown in Figure 1.7 for the three suites of parameter groups: $B_q Q_t$ defined previously (Figure 1.5), and $Q_t F_r$ and F_r / B_q. The Figures each incorporate both the proposed limits to partially-drained response (equations (1.9),

(1.10), and (1.11)), and appropriately defined permeability relations (equations (1.13), (1.16), and (1.17)), defining nondimensional permeability, K_D. Also included are correlated uCPT and independently measured permeability data from sites in clays through sands, identified in Table 1.1.

The transition from partially-drained to undrained penetration is represented on each of Figures 1.7 (a) through 1.7 (c) by the horizontal boundary. For the $B_q Q_t$ metric, the presumed undrained data (Amherst, Tyrone, and Various (Voyiadjis)) are most tightly constrained within the prescribed bounds of $1 < B_q Q_t < 6$. For the other metrics, undrained data transit the upper limit of the undrained response. The outlier Savannah River data of Figure 1.7 (b) are from above the water table, and their locations are moderated by pore pressure ratio in Figures (*viz.* Figures 1.7 (a) and (c)) that additionally incorporate B_q as a metric. Regardless of this, soundings in varved clays at Amherst spill beyond the undrained limits where either $Q_t F_r$ and F_r / B_q are used as metrics. Apparent from the previous is that the $B_q Q_t$ metric provides the most promising index between the partially-drained and undrained response.

Usefully, non-dimensional permeabilities may be defined in terms of the same metric pairs that index the transition from partially drained to undrained behavior. This evaluation is dependent only on the sounding metrics for $B_q Q_t$, but requires a measured or assumed frictional strength for either $Q_t F_r$ or F_r / B_q. These relations are included in Figure 1.7, where frictional strengths of $\phi = 10^o$ and 30° are selected. Where undrained data are ignored, the use of $B_q Q_t$ shows a positive correspondence between the data and the proposed permeability relationship $K_D = 1 / B_q Q_t$. For the other two metric pairs of

Figures 1.7 (b) and 1.7 (c), the data are broadly scattered around the proposed relations, making it difficult to reconcile permeability magnitudes from equations (1.16) and (1.17). This poor match is ascribed to the imperfect estimates of frictional strength that are recovered from the sleeve friction parameterizations. If equation (1.14) is used to directly recover friction angle, then predictions identical to using $K_D = 1/B_q Q_t$ are recovered. Thus there appears no advantage in utilizing either of the dependent relations embodied in Figures 1.7 (b) or 1.7 (c), over the independent relation, $K_D = 1/B_q Q_t$. Although Figures 1.7 (b) and 1.7 (c) appear less useful than 7 (a), an interesting feature is that both equations (1.16) and (1.17) asymptote to $K_D = 10^0$, the operational limit for partially drained response, and hence the limiting permeability that can be recovered, on-the-fly. This observation is consistent with the transition in drainage condition anticipated in the data of Table 1.1. Where the undrained data of Figure 1.7 (a) are excluded, the provisional best straight-line fit conforms to as $K_D = 0.62/(B_q Q_t)^{1.6}$, with a spread of approximately one order-of-magnitude around this best fit relationship.

1.5 Conclusions

A methodology is developed that potentially enables permeability profiles to be recovered from cone metrics routinely recovered from uCPT soundings, on-the-fly. The technique requires that penetration is partially drained, resulting in the penetration-induced tip-local pore fluid pressures reflecting the competition between the penetration process that generates excess pressures, and the dissipation process that ameliorates them. The latter process, for the dynamic steady state that develops rapidly around the cone tip, is primarily controlled by the permeability of the surrounding soil, with the magnitude of

the measured excess pore pressure therefore directly indexing permeability.

The proposed evaluation of permeability from the magnitude of peak pore fluid pressure requires that the penetration is partially drained, and that the pore pressure distribution has reached a dynamic steady state. The former is satisfied by excluding sounding data that are undrained, defined tentatively in this work as functions of the cone metric products and ratios, $B_q Q_t$, $Q_t F_r$, and B_q/F_r. The utility of these tentative metrics in identifying the transition between conditions of partial drainage and undrained behavior, local to the cone tip, is confirmed by collocated sounding and permeability data in materials from clays to sands, and spanning the permeability range 10^{-9} to 10^{-3} *m/s*. Standard penetration at 2 *cm/s* represents a near-constant tip-local strain rate that generates tip pressures, and the transition to conditions of partial drainage should be indexed relative to permeability alone. This appears to be the case, with the transition identified for permeabilities of the order of 10^{-5} to 10^{-6} *m/s*, based jointly on characteristics of soil texture (Table 1.1), and on correspondence established between predicted and measured permeabilities (Figures 1.5 and 1.7). In addition, sounding intervals containing penetration-reduced (negative or sub-hydrostatic) pore pressures are excluded from the characterization; these are not readily accommodated by the simple model presented here.

Where the penetration response is both partially drained and steady, permeability may be determined from the excess pore pressures through a relation of the form $K_D = \alpha/(B_q Q_t)^\beta$ for $B_q Q_t < 1.2$ where α and β are constants defined as unity from theory, and, as $\alpha = 0.62$ and $\beta = 1.6$ from the fitting to observational data $(R^2 = 0.7)$, and with a spread of approximately one order-of-magnitude either side of this relation.

Although the currently available data are meager, the reciprocal correlation between K_D and the metric pair $B_q Q_t$ is clear. This metric pair is the only one that provides an independent evaluation of permeability, from cone sounding data. Related correlations of K_D with the alternate pairs $Q_t F_r$, and B_q / F_r are not independent – they are dependent both on the primary assumption that $K_D = 1/B_q Q_t$, and additionally on assumptions of tip local stresses, that impart a further dependency on strength (in this case frictional strength). Correspondingly, a relation of the form $K_D = \alpha /(B_q Q_t)^\beta$ with $B_q Q_t < 1.2$ is both the most fundamental and most robust characterization available. Importantly, permeabilities are recovered from sounding data recovered on-the-fly, without the need to arrest penetration and to either record pressure dissipation, or to conduct miniature pump tests through the injection or recovery of fluids through the tip. Correspondingly, this method may be applied *a posteriori* to the extensive accumulated archive of sounding data, worldwide, enabling permeability profiles to be recovered where these data were initially neither recovered, nor sought.

Acknowledgements

References

Bai, M., and Elsworth, D. (2000). Coupled processes in subsurface deformation, flow, and transport, ASCE Press, Reston, VA.

Baligh, M. M. (1985). "Strain path method." Journal of Geotechnical Engineering, 111(9), 1108-1136.

Baligh, M. M., and Levadoux, J. N. (1986). "Consolidation after undrained piezocone penetration. II: Interpretation." Journal of Geotechnical Engineering, 112(7), 727-745.

Berg., v. d. (1994). " Analysis of Soil Penetration," Ph.D. Thesis, Delft University, Netherlands.

Burns, S. E., and Mayne, P. W. (1998). " Monotonic and dilatory pressure decay during piezocone tests in clay." Canadian Geotechnical Journal, 35(6), 1063-1073.

Campanella, R. G., and Robertson, P. K. "Current status of the piezocone test." Penetration Testing 1988, Orlando, 93-116.

Chiang, C. Y., Loos, K. R., and Klopp, R. A. (1992). "Field determination of geological/chemical properties of an aquifer by cone penetrometry and head-space analysis." Ground Water, 30(3), 428-436.

Cividini, A., and Gioda, G. (1988). "A simplified analysis of pile penetration." Proc. 6th Int. Conf. Num. Meth. Geomech, 1043-1049.

Danziger, F. A. B., Almeida, M. S. S., and Sills, G. C. (1997). "The significance of the strain path analysis in the interpretation of piezocone dissipation data." Geotechnique, 47(5), 901-914.

Douglas, B. J., and Olsen, R. S. "Soil classification using electric cone penetrometer."

Symposium on cone penetration testing and experience, St. Louis, 209-227.

Elsworth, D. (1990). " Theory of partially drained piezometer insertion." Journal of Geotechnical Engineering, 116(6), 899-914.

Elsworth, D. (1991). "Dislocation analysis of penetration in saturated porous media." Journal of Engineering Mechanics, 117(2), 391-408.

Elsworth, D. (1992). "Pore pressure response due to penetration through layered media." International Journal for Numerical and Analytical Methods in Geomechanics, 16, 45-64.

Elsworth, D. (1993). " Analysis of piezocone dissipation data using dislocation methods." Journal of Geotechnical Engineering, 119(10), 1601-1623.

Elsworth, D. (1998). "Indentation of a sharp penetrometer in a poroelastic medium." International Journal of Solids and Structures, 35(34-35), 4895-4904.

Elsworth, D., and Lee, D. S. (2004). "Permeability determination from On-the-fly piezocone sounding." Journal of Geotechnical and Geoenvironmental Engineering, In press.

Elsworth, D., and Lee, D. S. (2005). "Permeability determination from on-the-fly piezocone sounding." Journal of Geotechnical and Geoenvironmental Engineering, 131(5), 643-653.

Hill, R. (1983). The Mathematical Thory of Plasticity, Oxford University Press, Oxford.

Hryciw, R. D., Shin, S., and Ghalib, A. M. "High resolution site characterization by visCPT with application to hydrogeology." Proc. 12th Panamerican Conf. on Soil Mechs., Boston, 293-298.

Kiousis, P. D., and Voyiadjis, G. Z. (1985). "Lagrangian continuum theory for saturated

porous media." Journal of Engineering Mechanics, 111(10), 1277-1288.

Konrad, J. M., and Law, K. T. (1987). "Undrained Shear-Strength from Piezocone Tests." Canadian Geotechnical Journal, 24(3), 392-405.

Kurup, P. U., Voyiadjis, G. Z., and Tumay, M. T. (1994). "Calibration chamber studies of piezocone tests in cohesive soils." Journal of Geotechnical Engineering, 120(1), 81-107.

Lee, D. S., Elsworth, D., and Butler, J. J. (2004). "Direct evaluation of permeability from uCPT soundings: validation against data from the Nauen site, Germany." In preparation.

Levadoux, J. N., and Baligh, M. M. (1986). "Consolidation after undrained piezocone penetration. I: Prediction." Journal of Geotechnical Engineering, 112(7), 707-725.

Lunne, T., Robertson, P. K., and Powell, J. J. M. (1997). Cone Penetration Testing in Geotechnical Practice, Blackie Academic.

Manassero, M. (1994). "Hydraulic conductivity assessment of slurry wall using piezocone test." Journal of Geotechnical Engineering, 120(10), 1725-1746.

Mitchell, J. K., and Brandon, T. L. "Analysis and use of CPT in earthquake and environmental engineering." Geotechnical Site Characterization, 69-96.

Robertson, P. K. (1990). "Soil classification using the cone penetration test." Canadian Geotechnical Journal, 27(1), 151-158.

Robertson, P. K., Campanella, R. G., Gillespie, D., and Greig, J. "Use of piezometer cone data." Proc. ASCE Spec. Conf. In Situ '86. Use of In Sit Tests in Geotechnical Engineering, Blacksburg.

Robertson, P. K., Sully, J. P., Woeller, D. J., Lunne, T., Powell, J. J. M., and Gillespie, D.

G. (1992). "Estimating coefficient of consolidation from piezocone tests." Canadian Geotechnical Journal, 29(4), 539-550.

Schmertmann, J. H. (1978). "Guidelines for cone penetration test: Performance and design."

Skempton, A. W. (1954). "The pore pressure coefficients A and B." Geotechnique, 4, 143 - 147.

Smythe, J. M., Bedient, P. B., Klopp, R. A., and Chiang, C. Y. "An advanced technology for the in situ measurement of heterogeneous aquifers." Proc. Conf. New Field Tech. Quant. Phys.Chem. Prop. Heter. Aquifers, 605-628.

Song, C. R., Z., V. G., and Tumay, M. T. (1999). "Determination of permeability of soils using the multiple piezo-element penetrometer." IInternational Journal for Numerical and Analytical Methods in Geomechanics, 23(13), 1609-1629.

Teh, C., and Houlsby, G. (1991). "An analytical study of the cone penetration test in clay." Geotechnique, 41, 17-34.

Torstensson, B. A. (1977). "The pore pressure probe."

Vesic, A. S. (1972). "Expansion of cavities in infinete soil mass." Journal of the Soil Mechanics and Foundations Division, 98, 265-290.

Voyiadjis, G. Z., and Abu-Farsakh, M. Y. (1997). "Coupled theory of mixtures for clayey soils." Computers and Geotechnics, 20(3/4), 195-222.

Voyiadjis, G. Z., and Song, C. R. (2000). "Finite strain ansiotropic Cam Clay model with plastic spin. II: Application to piezocone test." Journal of Engineering Mechanics, 126(10), 1020-1026.

Voyiadjis, G. Z., and Song, C. R. (2003). "Determination of hydraulic conductivity using

piezocone penetration test." International Journal of Geomechanics, 3(2), 217-224.

Chapter 2: Pore Pressure Response Following Undrained uCPT Sounding in a Dilating Soil

Abstract

The generation and dissipation of pore fluid pressures following standard uCPT sounding in silty sands are observed to exhibit many of the characteristics of undrained penetration in dilatant materials; steady excess pore pressures may be sub-hydrostatic, or may become sub-hydrostatic during dissipation, and are slow to decay. Enigmatic pore pressure dissipation histories which transit from sub- to supra- and again to sub-hydrostatic before equilibrating at hydrostatic are consistent with a response where undrained pressures are maximally negative remote from the penetrometer tip. This surprising distribution of induced pore fluid pressures is accommodated in cavity expansion models for a dilating soil. A Mohr-Coulomb constitutive model is established for undrained loading of a soil with pore pressure response defined by Skempton pore pressure parameters. Defined in terms of effective stresses, this allows undrained stresses and pore pressures to be determined following cavity expansion in a $c-\phi$ soil. Pore pressures are conditioned by the shear modulus, Skempton A parameter, and the "undrained shear strength." The undrained shear strength is additionally modulated by the magnitudes of c, ϕ, A, and of the initial in situ effective stress, σ_0'. Cavity expansion stresses, and pore pressures may be back-calculated. Undrained pore pressures are shown to decay log-linearly with radius from the cavity wall; they may be either supra-hydrostatic or sub-hydrostatic at the cavity wall, and where supra-hydrostatic may become sub-hydrostatic close to the transition to the elastic region. This initial pressure

distribution contributes to the observed switching between supra- and sub-hydrostatic pore pressures recorded during dissipation. "Type curves" that reflect the dissipation response enable the consolidation coefficient, undrained strength and shear modulus to be computed from observed pore pressure data, and confirmed against independent measurements.

2.1 Introduction

Piezocone sounding (uCPT) is an evolving rapid, minimally invasive and inexpensive method for determining the mechanical and transport properties of soil, their spatial distribution, and the type and distribution of the soil-saturants (Campanella and Robertson 1988; Mitchell and Brandon 1998). Indirect methods to determine the transport characteristics of soils alternately rely on empirical correlations with soil gradation (Douglas and Olsen 1981; Manassero 1994; Robertson et al. 1986), from the imaging of soil fabric (Hryciw et al. 2003), or from correlations with cone metrics (Chiang et al. 1992; Smythe et al. 1989). Direct measurements may also be made using direct-push permeameters (Auxt and Wright 1995; Konrad and P. 1995; Lowry 1998; Scaturo and Wissowson 1997), or by measuring either rates of dissipation of excess pore pressures (Burns and Mayne 1998; Elsworth 1993; Gribb et al. 1998; Lunne et al. 1997; Robertson et al. 1992; Schmertmann 1978; Teh and Houlsby 1991; Torstensson 1977) or their on-the-fly magnitudes (Elsworth 1993; Elsworth 1998; Elsworth and Lee 2004; Elsworth and Lee 2006; Voyiadjis and Song 2003). Importantly, dissipation tests are usually conducted following undrained penetration where the dissipation of pore pressures following cone arrest are controlled by the coefficient of consolidation alone – additional assumptions regarding soil compressibility are required to allow estimation of

hydraulic conductivity. Conversely, on-the-fly pressure tests require that the loading is only partially drained, and consequently allow on-the-fly pressures to be a direct index of hydraulic conductivity.

Dissipation behavior is typically discussed in relation to penetration in clays. The development of undrained pore pressures is typically evaluated using cavity expansion (Burns and Mayne 1998; Torstensson 1977) or strain path models (Baligh 1985; Baligh and Levadoux 1986; Danziger et al. 1997; Levadoux and Baligh 1986; Teh and Houlsby 1991) to define initial pore pressure distributions that subsequently dissipate to background levels. These evaluations compare well with field (Baligh and Levadoux 1986; Levadoux and Baligh 1986) and calibration chamber (Kurup et al. 1994) results. Predictions from complex (Baligh and Levadoux 1986) and simple material models (Teh and Houlsby 1991) compare well with more rigorous representations of finite strain continuum behavior for clays (Kiousis and Voyiadjis 1985; Voyiadjis and Abu-Farsakh 1997; Voyiadjis and Song 2000), sands (Cividini and Gioda 1988) and clays to sands (Berg. 1994). For linear soil behavior, a variant of these methods may be applied to account for partial drainage in an effective stress analysis (Elsworth 1991; Elsworth 1993; Elsworth 1998) and this yields similar results to those from strain path and continuum models.

Although able to accommodate various soil models including overconsolidated and dilatant clays (Burns and Mayne 1998; Levadoux and Baligh 1986), undrained and dilatant response should not be restricted to penetration in cohesive materials. Recent observations of pressure dissipation following arrested penetration in silty sands exhibit many of the attributes of undrained penetration in dilatant soils. A mechanistic model to

describe this observed response is examined in the following.

2.2   Mechanical Response

We examine the mechanical response adjacent to the undrained expansion of a spherical cavity in a dilating soil, as a model for the local response to penetrometer insertion. The cavity is of radius a, within a soil subject to uniform initial total stress of σ_0 and initial pore pressure p_0. This geometry is illustrated in Figure 2.1. Equilibrium of total stresses is enforced for the assumed spherically symmetric geometry, accommodating Mohr-Coulomb failure and absent any change in volume. This enables the instantaneous undrained pore pressure distribution to be defined adjacent to the cavity.

2.2.1   Undrained Pore Pressures

Pore pressure change δp generated by changes in total maximum $\delta\sigma_1$ and minimum $\delta\sigma_3$ principal stresses may be determined in terms of the pore pressure coefficients A and B (Skempton 1954) as

$$\delta p = B\delta\sigma_3 + B\,A(\delta\sigma_1 - \delta\sigma_3). \tag{1.1}$$

The change in pore pressure is relative to an initial static pore pressure of magnitude p_0 and the change in the intermediate principal stress $\delta\sigma_2$ follows the minimum principal stress as $\delta\sigma_2 = \delta\sigma_3$. Final stress (σ_1, σ_3) and pore pressure p magnitudes are defined relative to initial magnitudes of the isotropic total stress (σ_0) and initial pore pressure (p_0) as,

$$\sigma_1 = \sigma_0 + \delta\sigma_1 \tag{1.2}$$
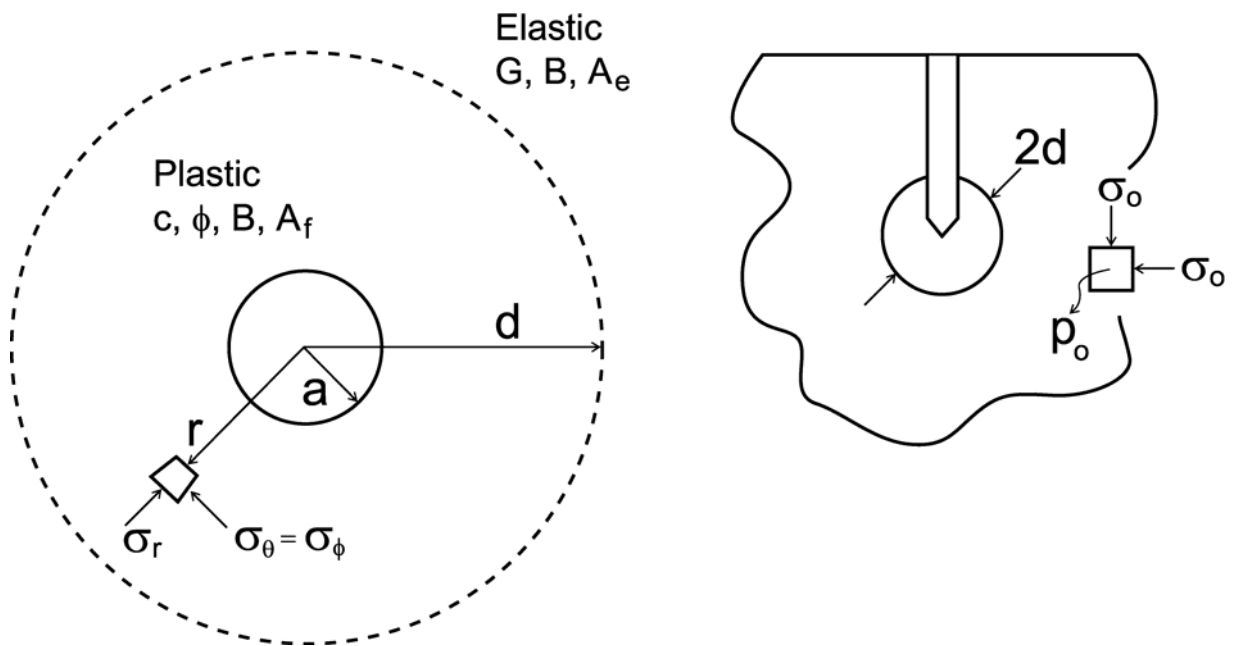
Figure 2.1: Spherical geometry of cavity inflated within an infinite medium

$$\sigma_3 = \sigma_0 + \delta\sigma_3 \tag{1.3}$$

$$p = p_0 + \delta p \tag{1.4}$$

with compressive stresses and pore fluid pressures defined positive. Substituting equations (1.2) through (1.4) into equation (1.1) enables generated pore pressures to be defined in terms of final total stresses as

$$p = (p_0 - B\sigma_0) + B\sigma_3 + B\ A(\sigma_1 - \sigma_3). \tag{1.5}$$

This defines the resulting pore fluid pressure relative to the induced total stresses that will be used in solving the stress equilibrium equation.

2.2.2   Constitutive Behavior

The Mohr-Coulomb criterion may be defined in terms of maximum $\sigma_1{}'$ and minimum $\sigma_3{}'$ principal effective stresses as

$$\sigma_1{}' = N\sigma_3{}' + 2c\sqrt{N} \tag{1.6}$$

where c is the cohesion and N indexes the frictional strength in terms of the frictional coefficient ϕ' as $N = (1 + \sin\phi')/(1 - \sin\phi')$. Effective stresses are defined as $\sigma_i{}' = \sigma_i - \alpha p$ where the Biot coefficient α is approximated as unity. Substituting for effective stresses in the failure criterion of equation (1.6) gives strength in terms of total stresses as,

$$\sigma_1 = N\sigma_3 + (1 - N)p + 2c\sqrt{N} \tag{1.7}$$

The undrained pore pressures of equation (1.5) may be substituted into equation (1.7) to yield the strength criterion defined in terms of total stresses as,

$$\sigma_1 = \frac{[N + (1 - N)(1 - A)B]}{[1 - (1 - N)\ B\ A]}\sigma_3 + \frac{[N - 1](B\sigma_0 - p_0) + 2c\sqrt{N}}{[1 - (1 - N)\ B\ A]}. \tag{1.8}$$

Importantly, this strength criterion defines an effective cohesion in the second term on the right-hand-side that includes two components. The first is due to the frictional resistance acting via the assumed uniform initial in situ effective stress $(B\sigma_0 - p_0)$, which is independent of stress change and invariant in space and time, and the second is a true cohesive component present when $c \neq 0$. Most transparently, when $B = 1$, the bracketed first term on the right-hand-side of equation (1.8) reduces to unity, and the expression is redefined as

$$\sigma_1 = \sigma_3 + 2\zeta \tag{1.9}$$

where

$$2\zeta = \frac{[N-1]\sigma_0' + 2c\sqrt{N}}{[1-(1-N)A]}. \tag{1.10}$$

Notably, the new strength criterion of equation (1.9) is in the form of a Tresca criterion. In this the shear strength $(\sigma_1 - \sigma_3)$ is not dependent on the minimum principal stress σ_3, and can be effectively represented by an effective undrained strength of $\zeta = S_u$. Note that a distinction is made between the initial cohesive strength of the soil ($c \neq 0$), such as due to an initial adhesion between soil grains, that may be destroyed by large displacements in the tip-local process zone, and the resulting undrained strength that results from the frictional contribution *via* changes in undrained pore pressures ($\zeta = S_u \neq 0$). The adhesion is a microscopic property, whereas the undrained strength is a macroscopic property of strength, which in this case replaces the frictional strength.

The principal assumption embodied in equations (1.9) and (1.10) is that loading is undrained. This condition is met if the permeability is sufficiently small, relative to the loading or soil strain (dilation or compaction) rate – a condition that is typically satisfied

for uCPT sounding in clays and silts, and even in fine sands. This ratio of pressure generation and pressure loss can be indexed relative to either material properties, or to cone measured indices. To first order, penetration response transits to undrained where the dimensionless permeability, $K_D = (4K\sigma_0')/(Ua\gamma_w)$ is less than unity ($K_D < 1$), as defined through hydraulic conductivity of the penetrated soil, K, the initial effective stress, σ_0', penetration rate, U, penetrometer radius, a, and the unit weight of water, γ_w (Elsworth and Lee 2005; Elsworth and Lee 2006). Non-dimensional permeability K_D represents the ratio of the rate of dissipation of fluid mass from the tip-local zone, to the rate of pressure generation by either dilation or compaction. The reciprocal of dimensionless permeability ($K_D = 1/B_q Q_t$) is alternately represented by the ensemble cone index of the product of penetration measured pore pressure ratio (B_q) and end-bearing (Q_t). Penetration is undrained when the product $B_q Q_t$ is greater than about unity ($B_q Q_t > 1$). Additionally, undrained loading absent the escape of fluid mass infers no net volume change in the soil-water assemblage, allowing simplified treatment of post-failure behavior in plasticity models.

Where displacements are sufficiently large to destroy any initial cohesion, or where frictional strength dominates, the failure criterion of equation (1.10), reduces to

$$2\zeta = \frac{[N-1]}{[1-(1-N)A]}\sigma_0' \qquad (1.11)$$

In this instance, the undrained strength $\zeta = S_u$ is controlled by the angle of internal friction ϕ', the pore pressure coefficient A and the initial uniform in situ effective stress σ_0', only. The variation of "normalized undrained strength" $\zeta/\sigma_0' \equiv S_u/\sigma_0'$

with A for $10° < \phi' < 40°$ is shown in Figure 2.2 (a). It is always positive and non-zero, with a singular magnitude at $A = 1/(1 - N)$.

The "undrained strength" ζ may be considered analogous to the effective frictional strength modulated by *in situ* effective stress as $\zeta = "S_u" = \sigma_0' \tan \phi$, as utilized to describe the rigidity index in terms of the shear modulus G as $G/Su = G/(c + \sigma_0' \tan \phi)$ (Vesic 1972). Thus where cohesion is negligible, the resulting drained ($Su/\sigma_0' = \tan \phi$) and undrained ($\zeta/\sigma_0' = \frac{1}{2}[N-1]/[1-(1-N)A]$; from equation (1.11)) strength ratios may be compared for various magnitudes of the pore pressure parameter A as in Figure 2.2 (b). The strength ratios Su/σ_0' and ζ/σ_0' are identical when $A = \frac{1}{3}$, corresponding to the elastic magnitude of A. As the pore pressure coefficient is increased relative to this, the material becomes weaker as excess pore pressures reduce the effective stresses. Conversely, for $A < \frac{1}{3}$ the undrained strength is increased as a consequence of dilation.

2.2.3   Stress Distribution around a Spherical Cavity

We describe the expansion of a spherical cavity within a soil where strength is independent of the local mean stress magnitude as $\sigma_1 = \sigma_3 + 2\zeta$, and where failure evolves absent volume change. This solution is directly analogous to cavity expansion within an elastic-perfectly-plastic soil with equivalent shear modulus G and undrained shear strength $Su = \zeta$. Satisfying equilibrium between radial σ_r and tangential σ_θ total stresses everywhere [Figure 2.1] as $\frac{d\sigma_r}{dr} + \frac{2(\sigma_r - \sigma_\theta)}{r} = 0$, subject to the strength criterion $\sigma_1 = \sigma_3 + 2\zeta$ in the failed zone, and Hooke's law in the elastic region, yields
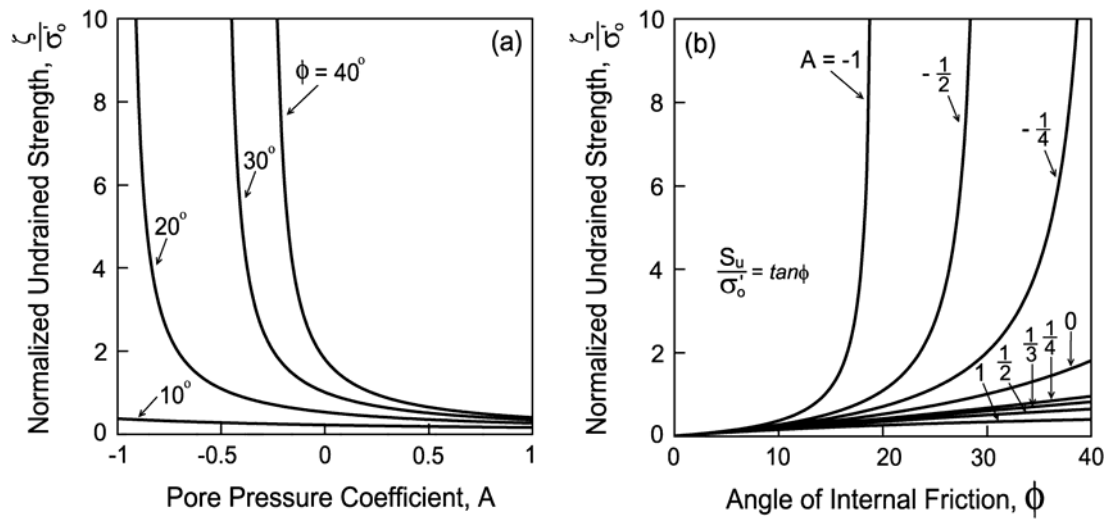
Figure 2.2: Variation of normalized undrained strength with (a) Skempton pore pressure coefficient A, and (b) angle of internal friction.

changes in the radial ($\delta\sigma_r = \delta\sigma_1$) and tangential ($\delta\sigma_\theta = \delta\sigma_3$) stresses in the failed region as (Elsworth and Lee 2006; Hill 1983),

$$\delta\sigma_r = \tfrac{4}{3}\zeta[1 + \ln(G/\varsigma) + 3\ln(a/r)] \tag{1.12}$$

$$\delta\sigma_\theta = \tfrac{4}{3}\zeta[-\tfrac{1}{2} + \ln(G/\varsigma) + 3\ln(a/r)]. \tag{1.13}$$

The failed zone extends to a radial distance $d = a(G/\zeta)^{1/3}$ around the cavity of radius $r = a$, with the change in radial stress at distance d obtained by setting $r = a(G/\zeta)^{1/3}$ in equation (1.12) to yield $\delta\sigma_r|_{r=d} = \tfrac{4}{3}\zeta$. Beyond this radius, the changes in stresses are elastic and are defined by the Lamé relations (Hill 1983), where substituting $\delta\sigma_r|_{r=d} = \tfrac{4}{3}\zeta$ and $d = a(G/\zeta)^{1/3}$ yields

$$\delta\sigma_r = \delta\sigma_{r|r=d}\frac{d^3}{r^3} = \tfrac{4}{3}G\frac{a^3}{r^3} \tag{1.14}$$

$$\delta\sigma_\theta = -\tfrac{1}{2}\delta\sigma_{r|r=d}\frac{d^3}{r^3} = -\tfrac{2}{3}G\frac{a^3}{r^3} \tag{1.15}$$

These provide the necessary relations to define initial undrained pore pressures.

2.2.4 Undrained Pore Pressure Distribution

With undrained changes in total stresses defined for both the failed (equations (1.12) and (1.13)) and elastic (equations (1.14) and (1.15)) regions, the resulting changes in pore fluid pressures may also be defined. Where a distinction is made between the pore pressure parameters of the failed ($B = 1; A = A_f$) and elastic ($B = 1; A = A_e = \tfrac{1}{3}$) (Elsworth 1991) regions, the resulting pore pressure distributions may be determined. For the failed region ($a < r < a(G/\zeta)^{1/3}$), the undrained pore pressure change is defined by substituting equations (1.12) and (1.13) into equation (1.1) as

$$\delta p = p - p_0 = \tfrac{4}{3}\zeta[(1 + \ln(G/\zeta)) - \tfrac{3}{2}(1 - A_f) + 3\ln(a/r)]. \tag{1.16}$$

For the elastic region ($a(G/\zeta)^{1/3} < r < \infty$) the pore pressures are similarly evaluated by substituting equations (1.14) and (1.15) into equation (1.1) to yield a null change in pore pressure as $\delta p = 0$. This null change in pore pressure results since the change in mean stress in the elastic zone is zero and any resulting deviatoric loading results in null volume change, and therefore no change in pressure.

These results are similar to those defined for undrained expansion of a cylindrical cavity in clays where induced pore pressures are indexed to the mean stress (Randolph and Wroth 1979), or for cylindrical and spherical geometries where induced pore pressures are determined from Skempton's pore pressure coefficients (Battaglio 1981). However, the constraint of applying only to cohesive soils is now lifted. As in other representations of cavity expansion in granular material, the limit stress is modulated by the shear modulus (Vesic 1972), although now the influence of undrained pore fluid pressures is directly incorporated.

The resulting changes in total stresses and in pore fluid pressures are illustrated schematically in Figure 2.3. In the failed zone, the stress difference is given by $\delta\sigma_r - \delta\sigma_\theta = \sigma_r - \sigma_\theta = 2\zeta$, and is constant throughout, while both the minimum and maximum principal stresses decrease linearly with log-radius. Correspondingly, pore pressures induced by the stress difference are uniform throughout the failed zone, and may be either positive or negative, depending on the pore pressure coefficients. Undrained pore pressure changes modulated by the minimum principal stress decrease log-linearly with radius from their peak at the cavity surface, with the potential to become negative at the interface with the elastic zone. The ultimate pressure change distribution
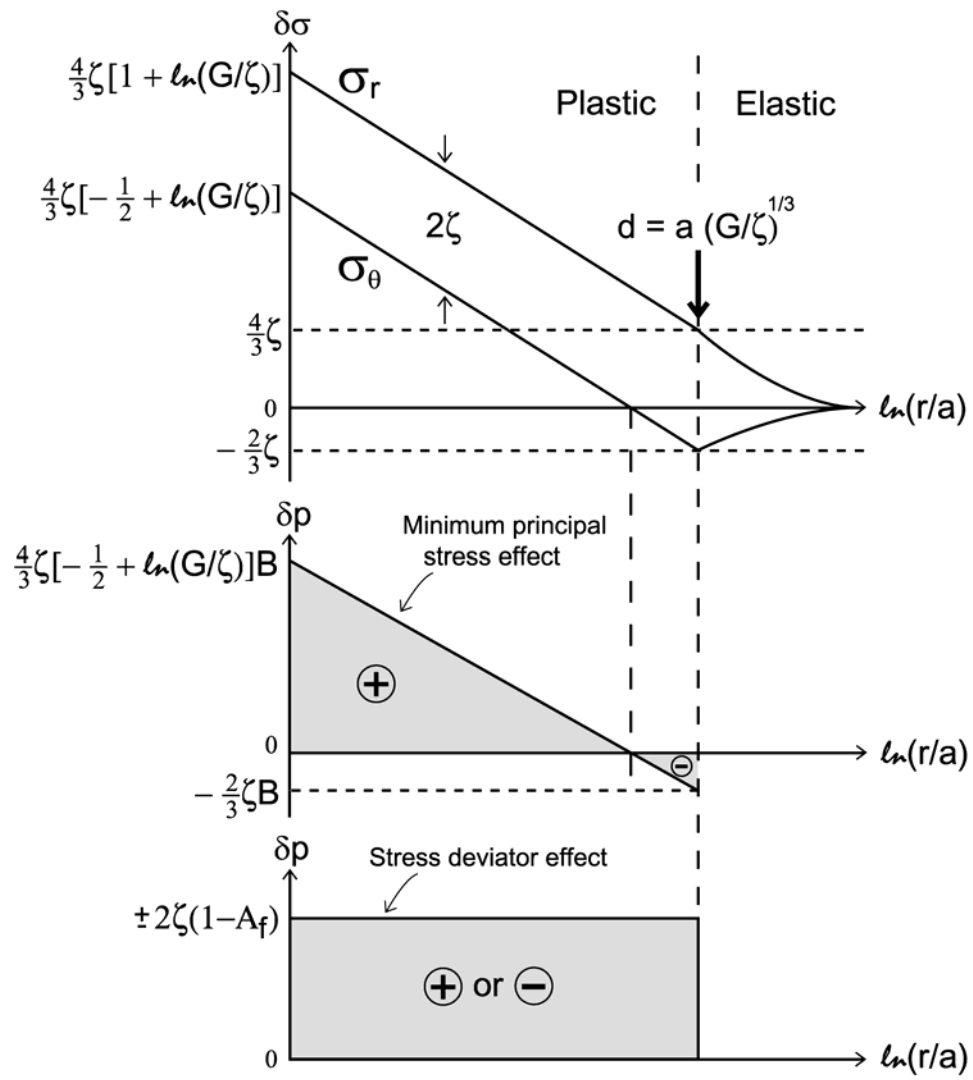
Figure 2.3: Variation in induced stresses and pore fluid pressures with radius from the wall of an expanded cavity within a saturated medium ($B = 1$).

is the combination of these effects, resulting in a pressure dropping monotonically with log-radius.

The resulting normalized undrained pore pressures are uniquely defined by the coefficients $\delta p / \zeta = \Im[G / \zeta; A_f; r / a]$ where ζ is a unique function of pore pressure coefficient A_f, friction angle ϕ', and initial mean stress σ_0. Although coefficients ζ and A_f, and perhaps ζ and G, are related, it is instructive to consider the anticipated influence of G / ζ and A_f on the anticipated radial distribution of change in normalized pore pressures $\delta p / \zeta$ with normalized radius r / a, as illustrated in Figure 2.4. These illustrate that normalized excess pore pressures increase with an increase in either of the parameters A_f or G / ζ. The pore pressure distribution is discontinuous, as is the change in tangential total stress, although radial total stresses are continuous. The abrupt transition of both pore pressures and tangential stresses at the outermost boundary of the plastic zone is a characteristic of the assumption of elastic-perfectly-plastic constitutive behavior.

2.3 Pressure Dissipation Response

With the undrained pressure distribution defined with radius, the dissipation response may be determined. Subject to appropriate magnitudes of the controlling parameters, the dissipation response may be described by a set of "type curves," to enable transport parameters to be recovered from the pressure dissipation data.

2.3.1 Pressure Diffusion Equation

The dissipation response may be described relative to the spherical symmetry of the
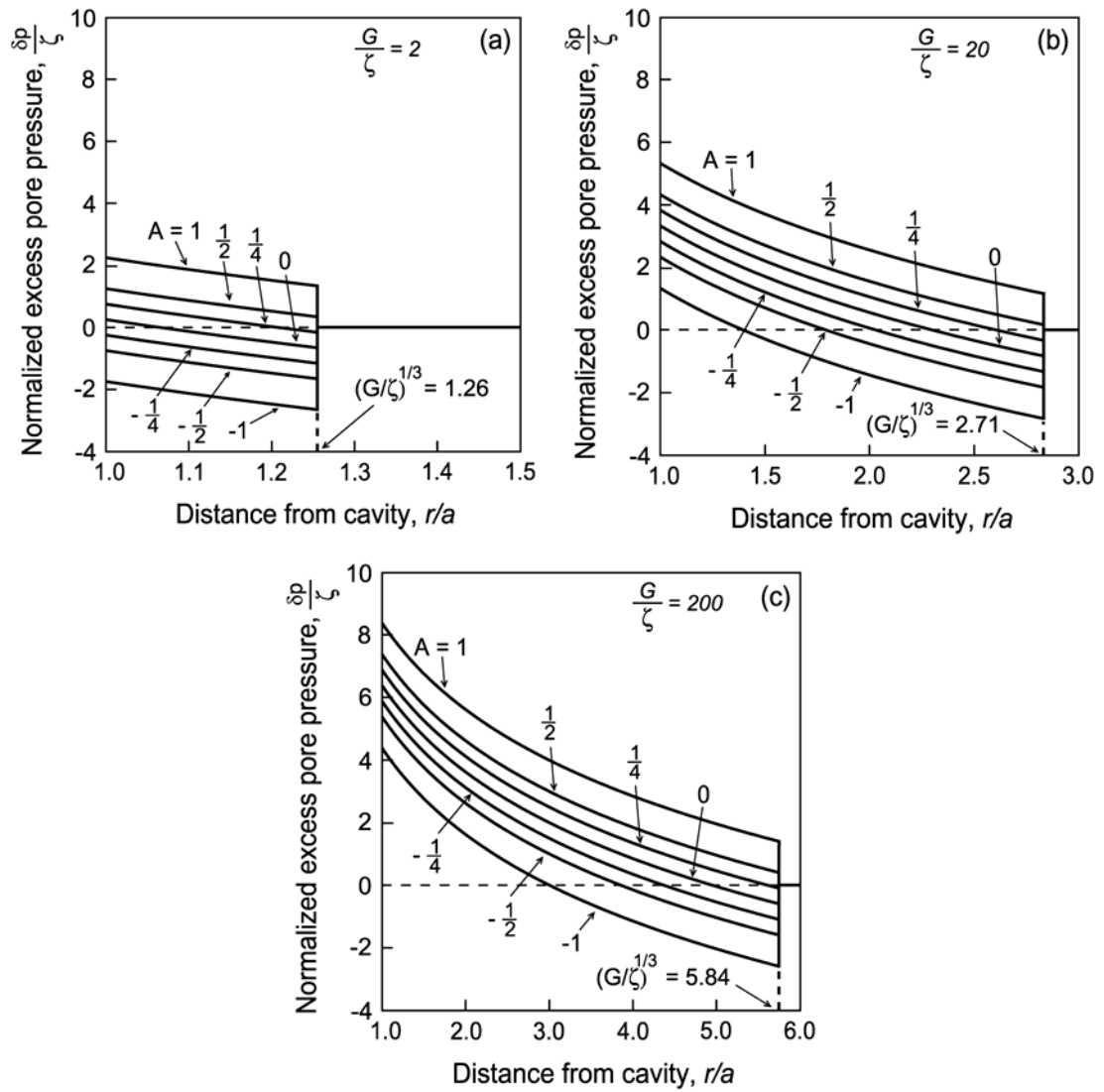
Figure 2.4: Variation in normalized excess pore pressure with dimensionless radius for ratios of shear modulus to undrained strength (G / ζ) of (a) 2, (b) 20, and (c) 200.

problem geometry through the diffusion equation

$$\kappa[\frac{\partial^2 p}{\partial r^2} + \frac{2}{r}\frac{\partial p}{\partial r}] = \frac{\partial p}{\partial t} \qquad (1.17)$$

defining changes in pressure p with time t, as modulated by hydraulic diffusivity or analogous consolidation coefficient κ. Initial conditions for the uncoupled analysis are defined in terms of fluid pressures relative to the baseline background pressure p_0 (Figure 2.1). These initial excess pressures are defined within the failed region $a < r < a(G/\zeta)^{1/3}$ by equation (1.16), and are null within the elastic region $a(G/\zeta)^{1/3} < r < \infty$. These initial conditions are supplemented by boundary conditions $\partial p / \partial r = 0$ at $r = a$, and $p = p_0$ at $r = \infty$. These conditions are applied to solve equation (1.17) using an axisymmetric finite element approximation. Variation within individual three-noded elements is linear, and the solution in time is by forward differencing (implicit method). The rectangular mesh extends to 20 cavity radii above, below, and to the side of the cavity, with a total of 24,000 degrees-of-freedom. The consolidation coefficient κ is prescribed uniform in space, and constant in time, with the solution proceeding at logarithmically varying time steps to a maximum non-dimensional time of $t_D = \kappa t / a^2 = 10^2$.

2.3.2   Type Curves

The pore pressure response may be defined most conveniently where equation (1.17) is recast in non-dimensional form as

$$[\frac{\partial^2 P_D}{\partial r_D{}^2} + \frac{2}{r_D}\frac{\partial P_D}{\partial r_D}] = \frac{\partial P_D}{\partial t_D} \qquad (1.18)$$

where non-dimensional pressure $P_D = (p - p_0)/\zeta$ varies in space $r_D = r/a$ and time

$t_D = \kappa t / a^2$. Similar to equation (1.17), initial conditions are for $P_D = 0$ at $t_D = 0$, and boundary conditions are $\partial P_D / \partial r_D = 0$ at $r_D = 1$, and $P_D = 0$ at $r_D = \infty$. In turn, non-dimensional pressures are indexed to the undrained response as $\delta p / \zeta = \Im[G / \zeta; A_f; r_D]$ with the parameter ζ additionally modulated by $\zeta = \Im[N; A_f; \sigma_0'; \text{and } c]$. Correspondingly, the two parameters of non-dimensional pressure P_D and time t_D are sufficient to examine the evolution of pressure measured at the cone face, $r_D = 1$.

At the cavity face ($r_D = 1$)the dissipation response ($P_D; t_D$) may be represented uniquely for the two parameters of shear modulus to strength ratio G / ζ and Skempton pore pressure parameter A_f. The dissipation response is shown for three representative magnitudes of $G / \zeta = 2, 20, 200$ and for pore pressure coefficients in the range $-1 < A_f < 1$ in Figure 2.5. Where G / ζ is smallest, the magnitude of the initial pore pressure distribution is also the smallest magnitude (Figure 2.4 (a)), and results in the shortest time history for pressures to decay (Figure 2.5 (a)). Both pore pressure magnitude and time-to-decay increase as G / ζ increases. As the magnitude of A_f decreases, both the magnitudes of the initial undrained pressures decrease, and the potential to develop negative pore pressures away from the cavity increases. Correspondingly, for intermediate and small (negative) magnitudes of A_f, pore pressures at the cavity face may begin positive, but become negative once negative pressures that are developed further into the failed zone reverse-diffuse towards the cavity. This feature is apparent for all selected shear moduli G / ζ but the threshold to this behavior occurs at progressively smaller magnitudes of the pore pressure parameter A_f as G / ζ
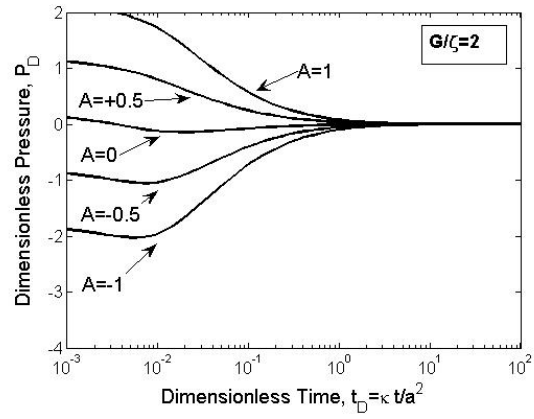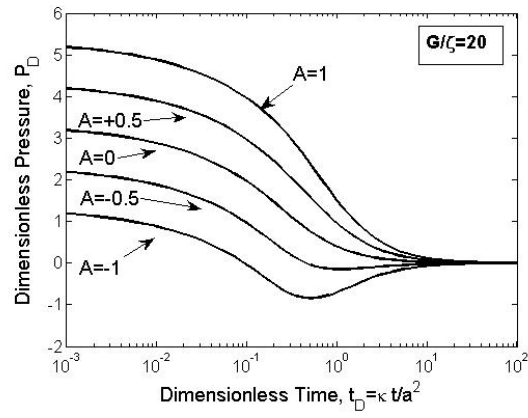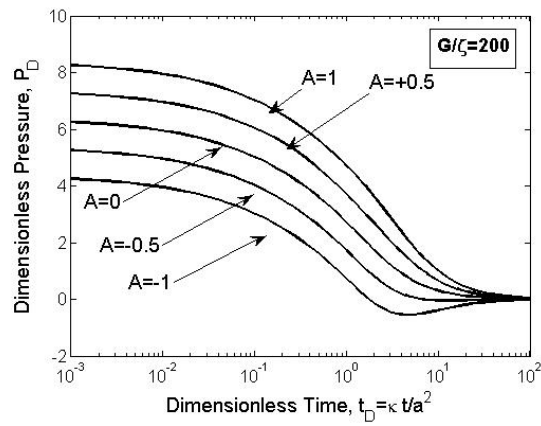
Figure 2.5: Dissipation of dimensionless excess pore pressure with dimensionless time for initial pressure distributions for shear modulus to undrained strength ratios (G/ζ) of (a) 2, (b) 20, and (c) 200.

increases. Where initial undrained pore pressures at the cavity face are sub-hydrostatic (e.g. Figure 2.4 (a), Figure 2.5 (a); $A_f < -1/4$) then pore pressures remain negative throughout the pressure history. Ultimately the pressure record dissipates to background levels (i.e. $P_D = 0$) and is of the order of 95% complete at $t_D > 10^0$.

Type curves may be directly compared with field data to determine the in situ material parameters affecting the undrained pore pressure and strength response (ζ), and of transport parameters (κ). In matching with field data, it is convenient to compare the absolute magnitudes of log-pressure with log-time, as represented in Figure 2.6. These are merely replots of the responses shown in Figure 2.5, with negative pressures shown as their absolute value (i.e. as positive to allow them to be shown on a log-log plot).

2.4 Data Analysis

A series of uCPT dissipation tests were conducted in silty sands near Milan, Michigan. These tests involved standard penetration at 2 *cm/s* using a standard 60° cone of 10 cm^2 end-bearing area. Pore pressures recorded during steady penetration were typically sub-hydrostatic but upon cone arrest would first become supra-hydrostatic, then again sub-hydrostatic, before asymptoting to the in situ magnitude. Typical responses are illustrated in Figure 2.7. These are interpreted to result from dilatant soils that drive the initial tip-local steady pore pressures to be sub-hydrostatic. The arrest of penetration releases the loading on the rods that gives a pore pressure response dominated by local conditions at the cone face. As these disturbed tip-local pore pressures change, the influence of the zone progressively more distant from the cone tip is felt, as pressure diffusion progresses. Ultimately, the influence of the distant zone of sub-hydrostatic pore pressures (Figure 2.4) is felt, driving tip-local pressures below hydrostatic, before

(a)

(b)

(c)
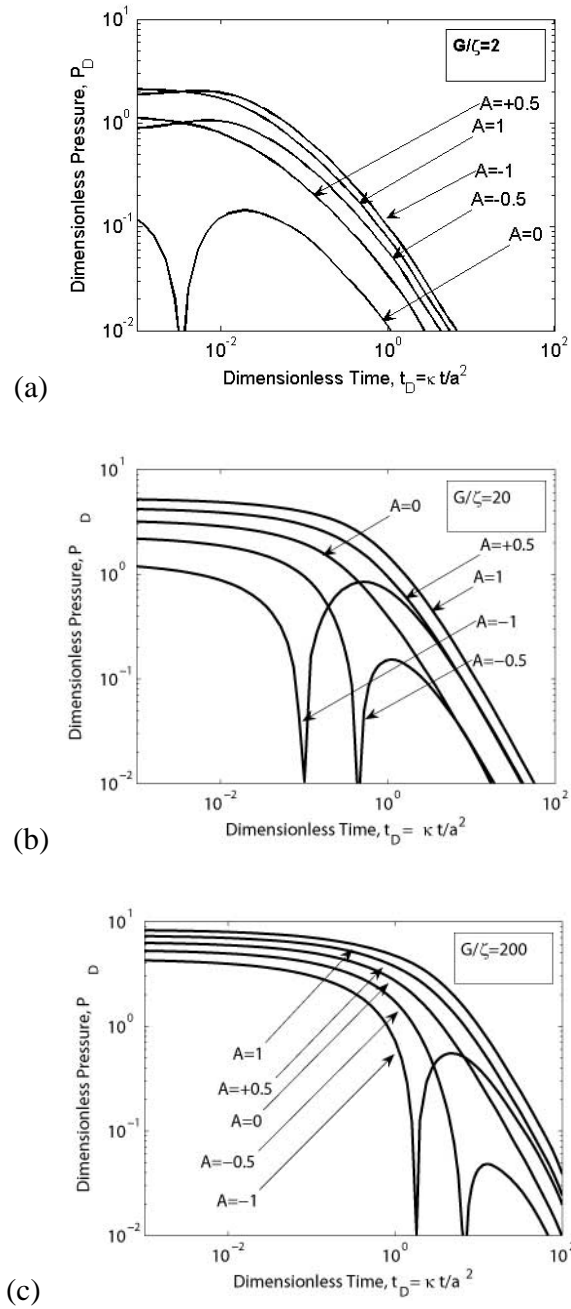
Figure 2.6: Dissipation of dimensionless excess pore pressure with dimensionless time for initial pressure distributions for shear modulus to undrained strength ratios (G/ζ) of (a) 2, (b) 20, and (c) 200. This is a log-log replot of the semi-log Figure 2.5, with the sub-hydrostatic pore pressures (negative) plotted as their absolute positive magnitude.
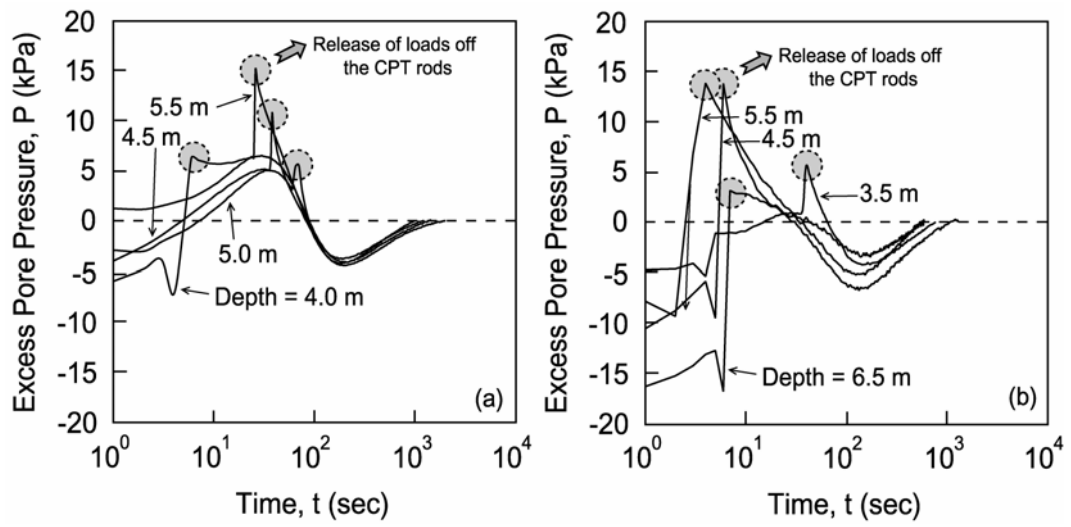
Figure 2.7: Pore pressure records for uCPT dissipation tests in silty sand for soundings in two adjacent profiles. Pressures are recorded at the u2 location on the piezocone.

ultimately asymptoting to background pressures. It is this late-time sub-hydrostatic response that is observed both in the transient "type curves" (Figure 2.5), and the field observations that is used to back-calculate mechanical and transport properties from the dissipation response. These are used to determine the shear modulus to undrained strength ratio (G/ζ), undrained strength (ζ), and consolidation coefficient (κ) from the field pore pressure dissipation data. These investigations are documented in the following.

2.4.1   Typical Dissipation Data

Pore pressure dissipation records are evaluated for the shallow Milan, MI, soundings in silty sand. The deposit is underlain by clay at a depth of ~6.5 m with the water table present at ~1.7 m below the ground surface. uCPT dissipation tests were conducted in two sounding profiles at depths of 4, 4.5, 5, and 5.5 m and 3.5, 4.5, 5.5, and 6.5 m below surface, in respective profiles. The pore pressures recorded at the u2 location are reported in Figure 2.7. Two different types of response of the excess pore pressure are apparent. The predominant response is where the initial excess pore pressure is sub-hydrostatic, but increases following the arrest of penetration, before dipping below hydrostatic on the way to equilibrium. The release of load from the CPT rod-string causes a jump in the pore pressure. Suppressing the loss of load on the rods makes no significant change in the observed pressure response. The second type of response is where the initial pore pressure is supra-hydrostatic (apparent in only one record at a depth of 5.5 m), but then follows the other curves noted previously. For both observed types of response, the time to the peak supra-hydrostatic pressure, and to the ultimate trough in the sub-hydrostatic pressure are similar. This coherence in the observed pressure signal (Figure 2.7) suggests that we are observing a characteristic of the system response, rather than an artifact of

unloading resulting from the test. The peak in positive pressure occurs in the interval 10 - 20 s, and the peak in negative pressure in the range 100 – 200 s. The mechanisms responsible for this unusual pressure-dissipation response are examined in the following.

2.4.2   Systematic Fitting of Type Curves

To enable representation of these pore pressures in log-pressure versus log-time space, the records of Figure 2.7 are recast as the absolute magnitude of excess pressure as shown in Figure 2.8 and in Figure 2.9. This transformation merely replots the semi-log plot as a log-log plot – since the sub-hydrostatic (negative) excess pressures cannot be represented on a log-scale, all negative pressures are plotted as their positive absolute magnitude. Importantly, the width of the pulse representing the negative pressure portion of the response is indicative of the magnitude of the pore pressure factor A_f. For these particular data, a fit is not feasible for shear modulus to strength ratios G/ζ of 2 nor 200. However, the data are congruent with the type curves for $G/\zeta = 25-30$, with A_f in the range -0.4 to -1.0. These data directly overprint the type curves for the late-time data, as shown in Figure 2.8 (a) through Figure 2.8 (d). Although the late-time match is excellent, the early-time data are not so well accommodated by this proposed model. This mismatch is magnified by the log-log representation. Since the early-time pressure response is generally indicative of near field processes, the tip-local mechanisms of local redistribution of stresses following penetration arrest are implicated. Rod unloading is not the reason, as similar pressure response results when the rod load is maintained, post arrest. Alternately, near-tip shearing or shearing at the probe shaft may have an undue influence in the near-field and initial response.
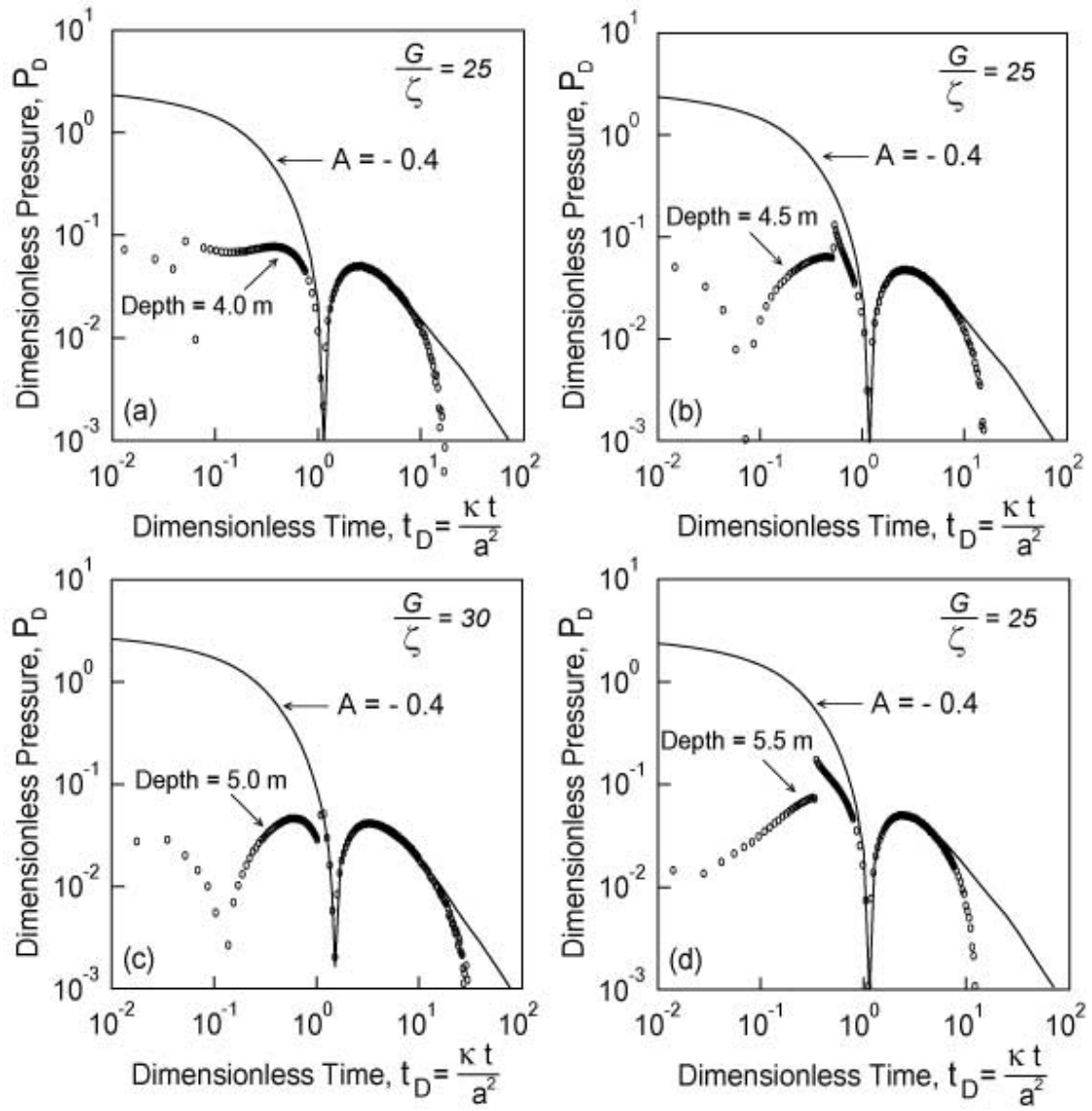
Figure 2.8: Pressure dissipation data of Figure 2.7 are shown (open circles) on the log-log type curves (solid line) of Figure 2.6. The four dissipation tests are from Figure 2.6 (left).
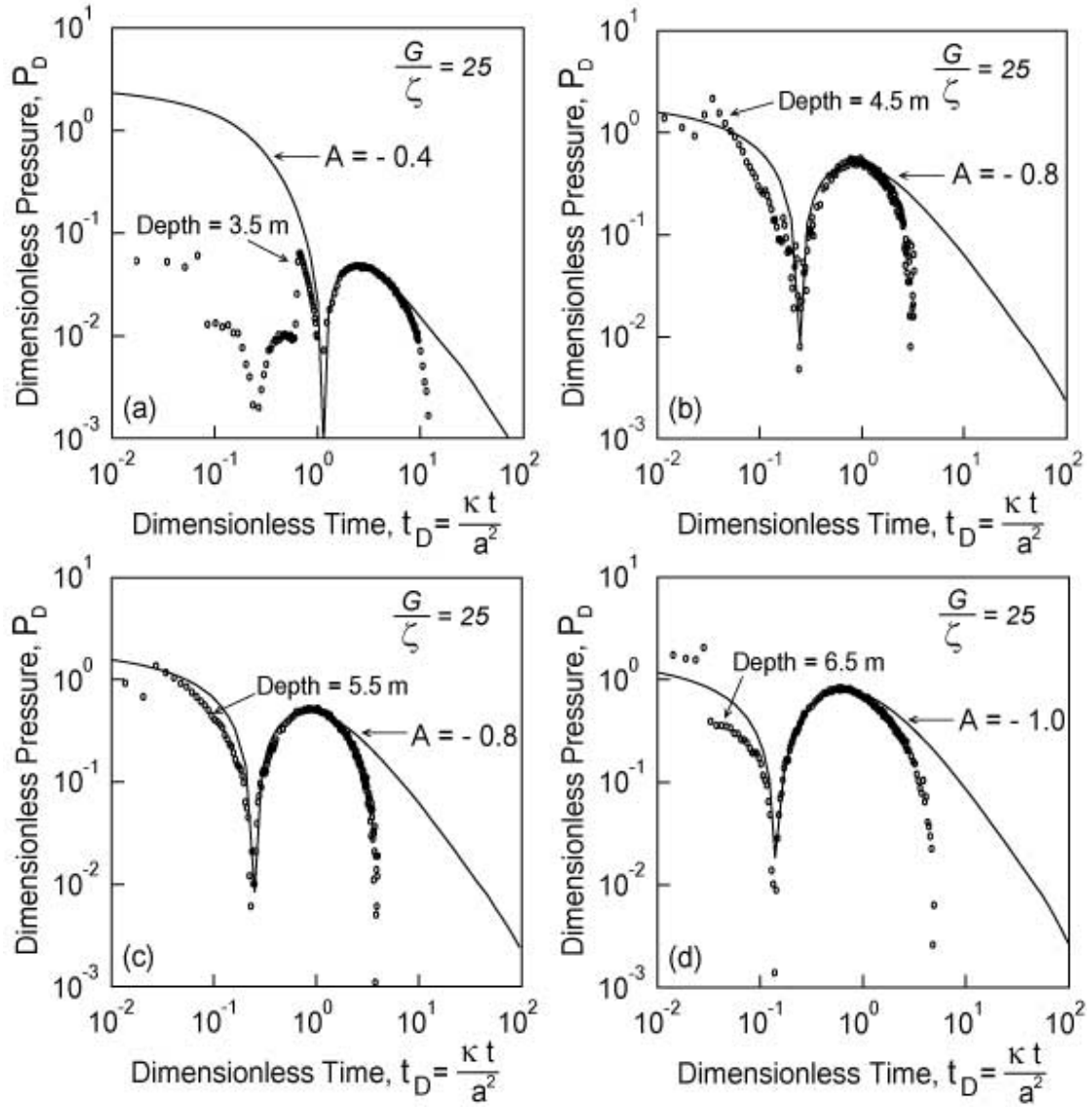
Figure 2.9: Pressure dissipation data of Figure 2.7 are shown (open circles) on the log-log type curves (solid line) of Figure 2.6. The four dissipation tests are from Figure 2.6 (right).

The type curves may be used to recover material properties by fitting with the data. The unique shape of the pressure response curves identifies $A_f \sim -0.4 \text{ to} -1.0$ and $G/\zeta \sim 20-30$ as illustrated in the remarkably consistent form of Figure 2.8 and Figure 2.9. The undrained strength (ζ) may be independently evaluated by matching the peak dimensionless excess pressure ($P_D = (p - p_0)/\zeta = 0.1 \text{ to} 1$) with the field-measured peak excess negative pore pressure ($p - p_0 = 7 \text{ to} 10\,kPa$) to yield $\zeta = 10-100\,kPa$. Correspondingly, the negative pressure peak (trough) occurs at $t_D = 1$ and corresponds to an actual time of $t = 60-112\,s$. From $t_D = \kappa t / a^2$, and for $a = 1.78 \times 10^{-2}\,m$ this yields a consolidation coefficient of $\kappa = 2.8 \times 10^{-6}\,to\,5.2 \times 10^{-6}\,m^2/s$ ($\sim 2.8 - 5.2\,mm^2/s$).Since the matches are for $G/\zeta \sim 25-30$, these correspond to effective shear moduli in the range $0.18 - 3.1\,MPa$.

These large strain magnitudes of shear modulus correspond to a moderate-strain modulus of 50 MPa recovered from dilatometer tests, and a small-strain modulus of 150 MPa recovered from shear wave velocity measurements, as identified in Table 2.1. This increase in magnitude with a reduction in the level of disturbance is as expected. Magnitudes of undrained strength are also recovered from the dilatometer tests, and at 200 – 400 kPa, these are broadly congruent with the upper-range strengths recovered from the dissipation tests at depth (Table 2.1).

2.4.3   Data for Overconsolidated Clays

Dissipation histories for uCPT penetration in clays ranging in overconsolidation ratio from 1.4 to 26 are compared against the results of this model. The collected data (Burns and Mayne 1998), for the eight sites exhibit only monotonic pore pressure dissipation in

Table. 2.1. Magnitudes of shear modulus, consolidation coefficient, and shear strength derived from dissipation and end bearing tests (this work), compared with independent evaluations from DMT and shear wave velocities.

	Dissipation Test	DMT	Shear Wave Velocity
Undrained Shear Modulus, G (*MPa*)	0.2 ~ 3	50	150
Consolidation Coefficient, κ (*mm^2 / s*)	2.8 ~ 5.2	–	–
Undrained Shear Strength, ς (*kPa*)	10 ~ 100	200 ~ 400	–

the long-term, and are readily fit to semi-log representations of the dissipation response, illustrated in Figure 2.10 for magnitudes of G/ζ of 2, 20, and 200. Of these anticipated responses only that for $G/\zeta = 200$ is absent sub-hydrostatic pore pressures in the very long-term, close to the termination of the record. Correspondingly, the data are fitted to the response for $G/\zeta = 200$ shown in Figure 2.10 (c). The behavior for lightly overconsolidated clays and silts (OCR 1-1.4) is shown in Figure 2.11 (a), and for more heavily overconsolidated clays and silts (OCR 3.5-26) in Figure 2.11 (b). These resulting fits are for positive magnitudes of the Skempton Parameter A, and enable magnitudes of consolidation coefficient to be determined from the matched t_{50} magnitude. Since all dissipation type-curves are similar, matching the observed t_{50} with the range of dimensionless t_{D50} magnitudes yields a range in consolidation coefficient magnitudes, κ. The non-dimensional magnitudes of t_{D50} range from 2×10^0 $(A = 1)$ to 3×10^{-1} $(A = 0)$, and result in a bounded range of predicted magnitudes of consolidation coefficient. These predicted magnitudes are compared with laboratory measured magnitudes in Table 2.2 and show favorable agreement.

2.5 Conclusions

Anomalous pore pressure dissipation records, recovered from uCPT tests in silty sands are explained in terms of pore pressures developed as a result of undrained dilation in the soil within the tip process zone. Observed pore pressures are typically first sub-hydrostatic, transit to supra-hydrostatic, and then return to sub-hydrostatic before slowly equilibrating to the in situ pore pressure. The timing of these different peaks and troughs in the pore pressure response (Figure 2.7) can be considered to reflect the distance of the
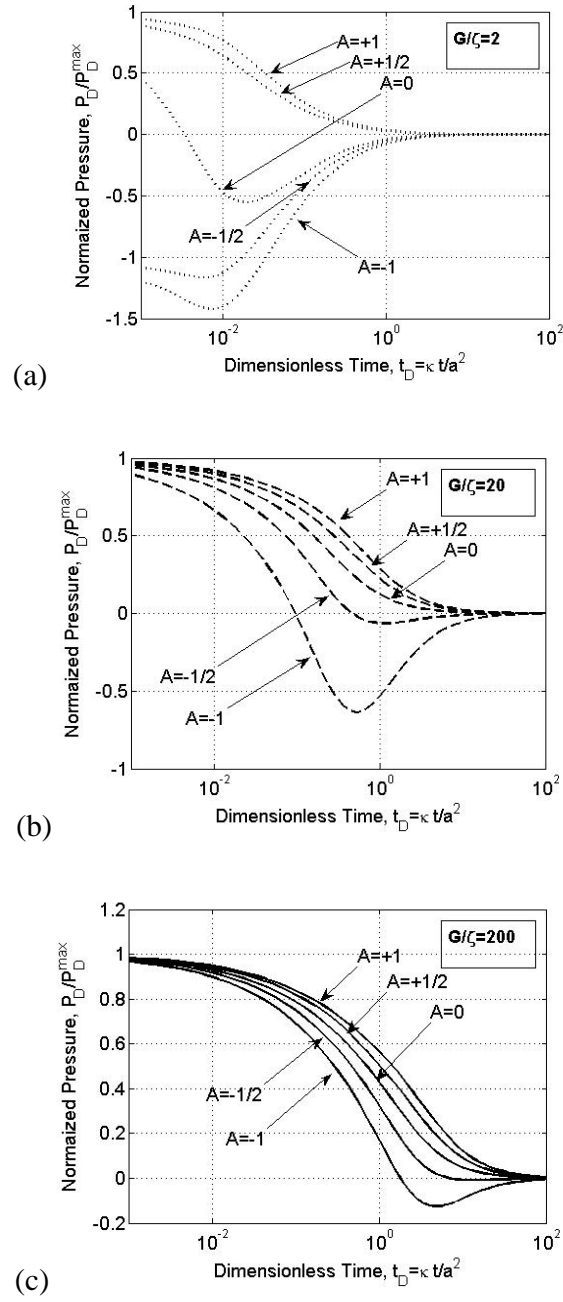
Figure 2.10: Normailzed pore pressure dissipation histories. Normailzed relative to pressure at $t_D = 0$. Distributions are for shear modulus to undrained strength ratios (G/ζ) of (a) 2, (b) 20, and (c) 200.

(a)

(b)
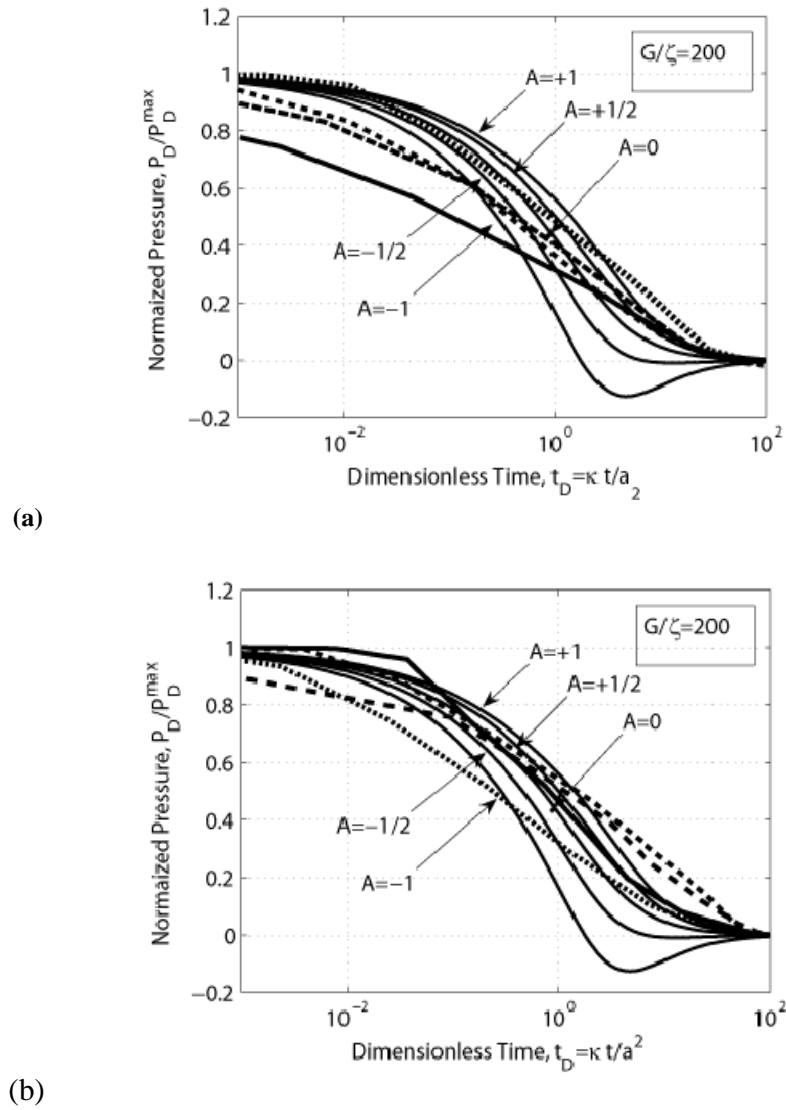
Figure 2.11: Matches between dissipation histories recovered from this method, and monotonic pore pressure changes recorded in dilatory soils at sites worldwide. Citations for the original data are reported in Table 2 for (a) lightly and (b) heavily overconsolidated soils. Responses are for (a) Bothkennar, UK (solid); Drammen, Norway (long-dashed); McDonald Farm, B.C. (short-dashed); St. Alban, Quebec (intermediate-dashed). (b) Amherst, Massachusetts (solid); Canon's Park, UK (long-dashed); St. Lawrence Seaway, N.Y. (short-dashed); Taranto, Italy (intermediate-dashed).

Table 2.2. Comparison of consolidation coefficients determined from this method with results of dissipation tests in dilatant materials (Burns and Mayne 1998).

Site	Depth (m)	OCR	t_{50} (s)	Laboratory Measured c_v or κ (mm^2/s)	Dissipation Test Measured c_v or κ (this study) (mm^2/s)	Comments	Reference
Bothkennar, U.K.	12.0	1.4	1000	0.32	0.13 ~ 0.48	Soft clay	(Nash et al. 1992)
Bothkennar, U.K.	12.0	1.4	1000	0.08 ~ 0.13	0.13 ~ 0.48	Soft clay	(Jacobs and Coutts 1992)
Drammen, Norway	19.5	1.1	700	0.53 ~ 1.52	0.18 ~ 0.68	Marine clay	(Lacasse 1982)
McDonald Farm, B.C.	20.0	1.1	200	1.8 ~ 5.5	0.64 ~ 2.38	Lean insensitive clayey silt	(Sully 1991)
Saint Alban, Quebec	4.6	1.2	800	0.30	0.16 ~ 0.59	Sensitive clay	(Roy et al. 1981)
Amherst, Mass.	3.0	7.0	200	0.07 ~ 0.10	0.64 ~ 2.38	Crust of soft clay	(DeGroot 1994; Lally 1993)
Canon's Park, U.K.	5.7	14.0	9000	0.01 ~ 0.03	0.12 ~ 0.43	102 mm pile in London Clay	(Jardine 1989)
St. Lawrence Seaway, N.Y.	6.1	3.5	600	0.25 ~ 0.80	0.21 ~ 0.79	Crust of soft clay	(Lutenegger 1987)
Taranto, Italy	9.0	26.0	1000	0.10 ~ 0.25	0.13 ~ 0.48	Cemented clay	(Battaglio 1986; Bruzzi 1987)

affected zone from the recording location, i.e. the u2-mounted transducer at the tip. The earliest events record the pore pressures diffusing from soil closest to the tip, and the latest events, telegraph the response from further away.

A model which represents the undrained pore pressure response of the soil to changes in applied spherical and deviatoric stresses is capable of replicating the intermediate- and late-time portion of this observed pore pressure response. If Skempton pore pressure parameters may be used to define the undrained response to spherical and deviatoric loads, then constitutive equations may be defined in terms of total stresses, and substituted into the spherically symmetric equilibrium conditions to determine the distribution of stresses and pore pressures which develop around an inflated spherical cavity. Importantly, the resulting total-stress constitutive equations are purely "cohesive," enabling both the total stress and undrained pore pressure distribution to be straightforwardly determined. Within the failure zone, and as a consequence of this model, the induced mean stress is shown to decline log-linearly with increasing radius from the cavity and potentially to become sub-hydrostatic remote from the cone face, while the deviatoric stress remains constant with radius. Induced pore pressures generated from these combined loading modes diminish with radius from the cavity wall, and may indeed become negative in the furthest extent of the failure zone. In the elastic region, beyond the failure zone, the undrained pore pressures are null. It is this resulting distribution of induced positive pore pressures close to the tip, and negative pore pressures at the outer extent of the failure zone, which results in both the first supra-hydrostatic peak and the final sub-hydrostatic trough, observed in the field dissipation response. Not explained by this model, are the initial highly negative pore pressures recorded at very early times.

These are suggested to result from intense tip-local shearing, that is not accommodated in the simple representation of penetromter advance as an expanding cavity (Burns and Mayne 1998).

In addition to explaining the general form of the pressure response, the analysis allows important parameters representing the mechanical and transport properties of the soil to be determined directly from the dissipation response. The parameters of shear modulus and undrained shear strength, accommodated in the analysis, are independently confirmed by measurements using the dilatomter test and through measurements of shear wave velocity. These independent measurements of modulus and strength are similar to the magnitudes recovered from the dissipation tests, but show a usual inverse trend in increasing modulus with a decrease in measurement strain.

Acknowledgements

References

Auxt, J. A., and Wright, D. (1995). "Environmental site characterization in the United States using the cone penetrometer." *Proc. CPT'95*, 387-392.

Baligh, M. M. (1985). "Strain path method." *Journal of Geotechnical Engineering*, 111(9), 1108-1136.

Baligh, M. M., and Levadoux, J. N. (1986). "Consolidation after undrained piezocone penetration. II: Interpretation." *Journal of Geotechnical Engineering*, 112(7), 727-745.

Battaglio, M., Bruzzi, D., Jamiolkowski, M., Lancellotta, R. "Interpretation of CPTs and CPTUs: undrained penetration of saturated clays." *4th Internatinal Geotechnical Seminar, Field Instrumentation and In Situ Measurements*, Singapore, 129-156.

Battaglio, M., Jamiolkowski, M., Lancellotta, R., and Maniscalco, R. "Piezometer probe test in cohesive deposits." *International Conference on Numerical Methods in Geomechanics*.

Berg., v. d. (1994). " Analysis of Soil Penetration," Ph.D. Thesis, Delft University, Netherlands.

Bruzzi, D., Battaglio, M. "Pore pressure measurements during cone penetration tests." *I quadermi dell'ISMES [Experimental Institute for Models and Structures]*, Milan, Italy.

Burns, S. E., and Mayne, P. W. (1998). " Monotonic and dilatory pressure decay during piezocone tests in clay." *Canadian Geotechnical Journal*, 35(6), 1063-1073.

Campanella, R. G., and Robertson, P. K. "Current status of the piezocone test." *Penetration Testing 1988*, Orlando, 93-116.

Chiang, C. Y., Loos, K. R., and Klopp, R. A. (1992). "Field determination of geological/chemical properties of an aquifer by cone penetrometry and head-space analysis." *Ground Water*, 30(3), 428-436.

Cividini, A., and Gioda, G. (1988). "A simplified analysis of pile penetration." *Proc. 6th Int. Conf. Num. Meth. Geomech*, 1043-1049.

Danziger, F. A. B., Almeida, M. S. S., and Sills, G. C. (1997). "The significance of the strain path analysis in the interpretation of piezocone dissipation data." *Geotechnique*, 47(5), 901-914.

DeGroot, D. J., Lutenegger, A.J. "A comparison between field and laboratory measurements of hydraulic conductivity in a varved clay." *Hydraulic Conductivity and Waste Containment Transport in Soil.*, 300-317.

Douglas, B. J., and Olsen, R. S. "Soil classification using electric cone penetrometer." *Symposium on cone penetration testing and experience*, St. Louis, 209-227.

Elsworth, D. (1991). "Dislocation analysis of penetration in saturated porous media." *Journal of Engineering Mechanics*, 117(2), 391-408.

Elsworth, D. (1993). " Analysis of piezocone dissipation data using dislocation methods." *Journal of Geotechnical Engineering*, 119(10), 1601-1623.

Elsworth, D. (1998). "Indentation of a sharp penetrometer in a poroelastic medium." *International Journal of Solids and Structures*, 35(34-35), 4895-4904.

Elsworth, D., and Lee, D. S. (2004). "Permeability determination from On-the-fly piezocone sounding." *Journal of Geotechnical and Geoenvironmental Engineering*, In press.

Elsworth, D., and Lee, D. S. (2005). "Permeability determination from on-the-fly

piezocone sounding." *Journal of Geotechnical and Geoenvironmental Engineering*, 131(5), 643-653.

Elsworth, D., and Lee, D. S. (2006). "Limits in determining permeability from on-the-fly uCPT soundings." *Submitted for publication*, 131, 30.

Gribb, M. M., Limunek, J., and Leonard, M. F. (1998). "Development cone penetrometer method to determine soil hydraulic properties." *Journal of Geotechnical and Geoenvironmental Engineering*, 124(9), 820-829.

Hill, R. (1983). *The mathematical theory of plasticity*, Clarendon Press, Oxford Univerity Press, New York.

Hryciw, R. D., Shin, S., and Ghalib, A. M. "High resolution site characterization by visCPT with application to hydrogeology." *Proc. 12th Panamerican Conf. on Soil Mechs.*, Boston, 293-298.

Jacobs, P. A., and Coutts, J. S. (1992). "A Comparison of Electric Piezocone Tips at the Bothkennar Test Site." *Geotechnique*, 42(2), 369-375.

Jardine, R. J., Bond, A.J. "Behaviour of diplacement piles in heavily overconsolidated clay." *12th Int. Conf. Soil Mechs. and Foundation Eng.*, Rio de Janiero, 1147-1151.

Kiousis, P. D., and Voyiadjis, G. Z. (1985). "Lagrangian continuum theory for saturated porous media." *Journal of Engineering Mechanics*, 111(10), 1277-1288.

Konrad, J. M., and P., F. "The piezocone-permeameter probe: A promising tool." *Proc. Geoenvir. 2000, Charact., Contain., Remed. and Perform. Environ. Geotechnics, GSP*, 123-137.

Kurup, P. U., Voyiadjis, G. Z., and Tumay, M. T. (1994). "Calibration chamber studies of

piezocone tests in cohesive soils." *Journal of Geotechnical Engineering*, 120(1), 81-107.

Lacasse, S., Lunne, T. "Penetration tests in two Norweigian clays." *2nd European Symposium on Penetration Testing.*, Amsterdam, 661-669.

Lally, M. J. (1993). "A field and laboratory investigation of geotechnical properties for design of a seasonal heat strorage facility," University of Massachusetts at Amhers.

Levadoux, J. N., and Baligh, M. M. (1986). "Consolidation after undrained piezocone penetration. I: Prediction." *Journal of Geotechnical Engineering*, 112(7), 707-725.

Lowry, B. (1998). "Cone Permeameter In-Situ Permeability Measurements with Direct Push Techniques." Science and Engineering Associates, Inc.

Lunne, T., Robertson, P. K., and Powell, J. J. M. (1997). *Cone Penetration Testing in Geotechnical Practice*, Blackie Academic.

Lutenegger, A. J., Kabir, M.J. (1987). "Pore pressures generated by two penetrometers in clays." *87-2*, Department of Civil Engineering, Clarkson University, Potsdam, NY.

Manassero, M. (1994). "Hydraulic conductivity assessment of slurry wall using piezocone test." *Journal of Geotechnical Engineering*, 120(10), 1725-1746.

Mitchell, J. K., and Brandon, T. L. "Analysis and use of CPT in earthquake and environmental engineering." *Geotechnical Site Characterization*, 69-96.

Nash, D. F. T., Powell, J. J. M., and Lloyd, I. M. (1992). "Initial Investigations of the Soft Clay Test Site at Bothkennar." *Geotechnique*, 42(2), 163-181.

Randolph, M. F., and Wroth, C. P. (1979). "Analytical Solution for the Consolidation around a Driven Pile." *International Journal for Numerical and Analytical*

Methods in Geomechanics, 3(3), 217-229.

Robertson, P. K., Campanella, R. G., Gillespie, D., and Greig, J. "Use of piezometer cone data." *Proc. ASCE Spec. Conf. In Situ '86. Use of In Sit Tests in Geotechnical Engineering*, Blacksburg.

Robertson, P. K., Sully, J. P., Woeller, D. J., Lunne, T., Powell, J. J. M., and Gillespie, D. G. (1992). "Estimating coefficient of consolidation from piezocone tests." *Canadian Geotechnical Journal*, 29(4), 539-550.

Roy, M., Blanchet, R., Tavenas, F., and Larochelle, P. (1981). "Behavior of a Sensitive Clay During Pile Driving." *Canadian Geotechnical Journal*, 18(1), 67-85.

Scaturo, D. M., and Wissowson, M. A. (1997). "Experimental evaluation of a drive-point ground-water sampler for hydraulic conductivity measurement." *Ground Water*, 35(4), 713-720.

Schmertmann, J. H. (1978). "Guidelines for cone penetration test: Performance and design."

Skempton, A. W. (1954). "The pore pressure coefficients A and B." *Geotechnique*, 4, 143 - 147.

Smythe, J. M., Bedient, P. B., Klopp, R. A., and Chiang, C. Y. "An advanced technology for the in situ measurement of heterogeneous aquifers." *Proc. Conf. New Field Tech. Quant. Phys.Chem. Prop. Heter. Aquifers*, 605-628.

Sully, J. P. (1991). "Measurement of in situ lateral stress during full-displacement penetration tests.," Ph.D. Thesis, University of British Columbia, Vancouver, B.C.

Teh, C., and Houlsby, G. (1991). "An analytical study of the cone penetration test in clay." *Geotechnique*, 41, 17-34.

Torstensson, B. A. (1977). "The pore pressure probe."

Vesic, A. S. (1972). "Expansion of cavities in infinete soil mass." *Journal of the Soil Mechanics and Foundations Division*, 98, 265-290.

Voyiadjis, G. Z., and Abu-Farsakh, M. Y. (1997). "Coupled theory of mixtures for clayey soils." *Computers and Geotechnics*, 20(3/4), 195-222.

Voyiadjis, G. Z., and Song, C. R. (2000). "Finite strain ansiotropic Cam Clay model with plastic spin. II: Application to piezocone test." *Journal of Engineering Mechanics*, 126(10), 1020-1026.

Voyiadjis, G. Z., and Song, C. R. (2003). "Determination of hydraulic conductivity using piezocone penetration test." *International Journal of Geomechanics*, 3(2), 217-224.

Chapter 3: Direct Evaluation of Hydraulic Conductivity from uCPT Profiles: Validation Against Data from the Nauen Test Site, Germany

Abstract

Solutions have recently been reported for the fluid pressure field that develops around an advancing penetrometer. Those solutions show that, under certain conditions, peak pore pressures are strongly controlled by the in-situ hydraulic conductivity (K), presenting the possibility that pore pressures recorded by a sensor on a uCPT probe could be used to obtain K profiles without needing to stop probe advancement. The inclusion of a pore-pressure sensor on a CPT probe is not universal. Thus, the possibility of K estimation using traditional CPT cone and friction resistance parameters is also explored. The non-dimensional CPT parameters, cone resistance, sleeve resistance, and the pore pressure ratio, are used in paired combinations to estimate hydraulic conductivity. The proposed methods are assessed using uCPT profiles completed at an unusually well characterized site at Nauen, Germany. Hydraulic conductivity predictions based on pore-pressure data compare reasonably with independent measurements of K from slug tests, direct-push permeameter (DPP) profiling, and grain-size correlations over a limited range of hydraulic conductivities. The overall average of the uCPT K estimates was only 6% higher than that from the DPP profile. However, the average absolute difference between values obtained over the same depth interval with these two approaches was 16% larger than the average uCPT-predicted K value. The K range for the majority of the intervals used in this assessment was $10^{-4} \sim 10^{-3}$ m/s, potentially near the upper end of the theoretical range of applicability of the proposed methodology. Given that the approach was applied in the vicinity of the upper end of its range of applicability, the results of this

comparison must be considered promising. Hydraulic conductivity prediction in the absence of pore-pressure data appears less promising. The empirical classification charts of (Robertson 1990) appear to be the best alternative in the absence of pore-pressure data.

3.1 Introduction

Cone penetration testing (uCPT) is a reliable and rapid method for determining the mechanical properties of unconsolidated materials (Mitchell and Brandon 1998). In a uCPT test, a cone-shaped probe (penetrometer) at the end of a string of steel rods is pushed into the ground at a constant rate ($2\, cm/s$). Near-continuous with depth measurements are made of the resistance to penetration of the cone, the resistance along a trailing sleeve, and the induced pore-fluid pressure immediately adjacent to the cone (Lunne et al. 1997). These data are used to determine media properties, either through empirical correlations (Douglas and Olsen 1981; Robertson et al. 1986) or by inversion using mechanistic models (Campanella and Robertson 1988). A considerable amount of work has been directed at the use of uCPT data to estimate hydraulic conductivity (K), a critical parameter for ground-water investigations. Current uCPT methods for determining K are primarily based on the dissipation test, which involves temporarily suspending penetrometer advancement and monitoring the dissipation of the penetration-induced pore pressures to background conditions (Robertson et al. 1992). Hydraulic conductivity is then calculated from $K = \gamma_w m_v c_v$, where c_v is the coefficient of consolidation determined from the analysis of the dissipation data, m_v is the empirically determined volumetric compressibility of the media, and γ_w is the unit weight of water. Estimates of K obtained in this manner, however, are questionable because of the large

uncertainty introduced through the determination of m_v using one of many possible empirical equations (Lunne et al. 1997).

The pore pressures generated during penetration are a function of the hydraulic conductivity of the medium. Thus, measurements of pore pressures and other uCPT parameters could potentially be the basis of a useful method of determining K on-the-fly, i.e. without the need to suspend advancement and perform a dissipation test (Elsworth 1993). However, a lack of understanding of pore-fluid pressures and local stresses that develop around the tip of the cone, combined with the paucity of collocated measurements of K and uCPT parameters, has made it difficult to assess the potential of such an approach. In this paper, we compare uCPT-derived K values with independent estimates obtained from slug tests, direct-push permeameter profiling, and grain-size correlations in an attempt to gain insight into that potential.

3.2   Test Site Nauen, Germany

Direct and indirect methods for determining hydraulic conductivity have been extensively evaluated at the Nauen test site near Berlin, Germany (Dietrich et al. 2003). The shallow subsurface at the Nauen site consists of fine to medium grained sands overlying glacial till. Hydraulic conductivity estimates from slug tests, direct-push permeameter (DPP) profiling, and correlations with grain-size data have been obtained from a group of closely spaced boreholes (Figure 3.1). Slug tests have been performed at four different depths in three direct-push probe holes using the methods described by Butler et al. (2002) and Butler (2002). A near-continuous (spacing~0.5m) DPP profile of K was obtained from a single direct-push probe hole. The DPP involves pushing a screened tool to a depth at which information is desired and then monitoring the pressure
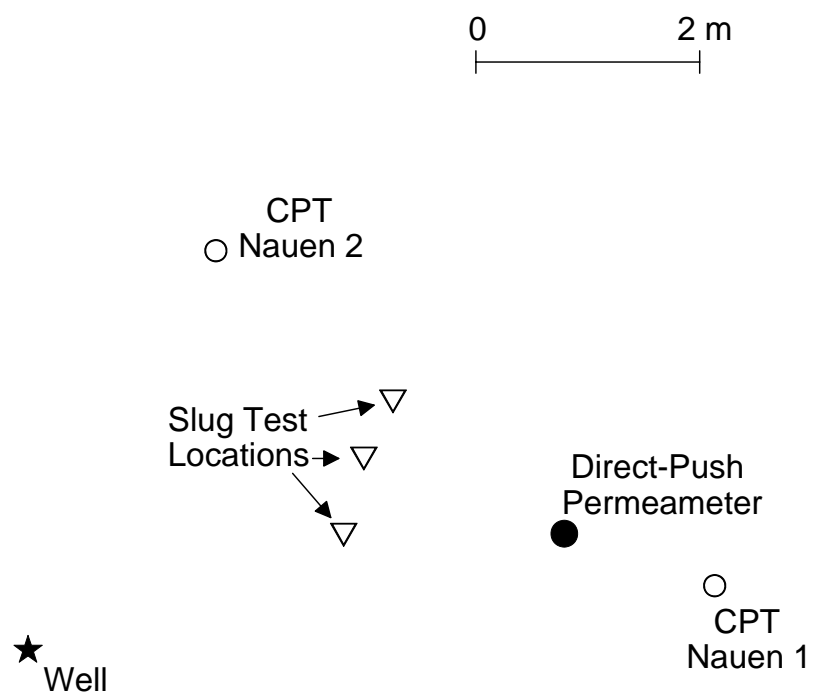
Figure 3.1: Areal view of profile locations (cores for grain-size analyzes obtained at well).

response to water injection through the screen while the tool is stationary (Figure 3.2). Water pressures are recorded at two axial locations along the tool shaft, enabling K to be determined from the prescribed injection rate and the induced fluid pressure (Butler and Dietrich 2004; Butler 2005). Measurements from the DPP are available only to relatively shallow depths ($\sim 15\,m$) at the Nauen site because the specific tool used in the study could only be advanced with a small direct-push unit (Geoprobe) and the down hole pressure transducers precluded the hammer-assisted forms of direct-push technology normally used with that unit. A continuously cored borehole provided grain-size data that were used to estimate K from empirical correlations with grain-size distributions (Hazen 1930). In a later section, this suite of K data is used to evaluate the quality of hydraulic conductivity predictions obtained from the two uCPT logs performed at the site. In both cases, the logs were obtained without suspending penetration for dissipation testing.

3.3   On-the-fly Hydraulic Conductivity Evaluation

The idea behind on-the-fly evaluations (Elsworth 1993; Elsworth and Lee 2005) is that hydraulic conductivity can be determined from the pore-fluid pressures measured immediately adjacent to the cone during probe advancement. The rate of dissipation of pore pressures generated around the tip of an advancing probe is controlled by the hydraulic conductivity of the media. Low conductivities impede drainage, resulting in higher pore pressures. This behavior may be represented by linear poroelastic models of the partially drained mechanical response around a moving blunt penetrometer (Elsworth 1990; Elsworth 1991; Elsworth 1992; Elsworth 1993) or around a tapered tip (Elsworth 1998; Lee and Elsworth 2004), or by a more realistic large-strain coupled theory of
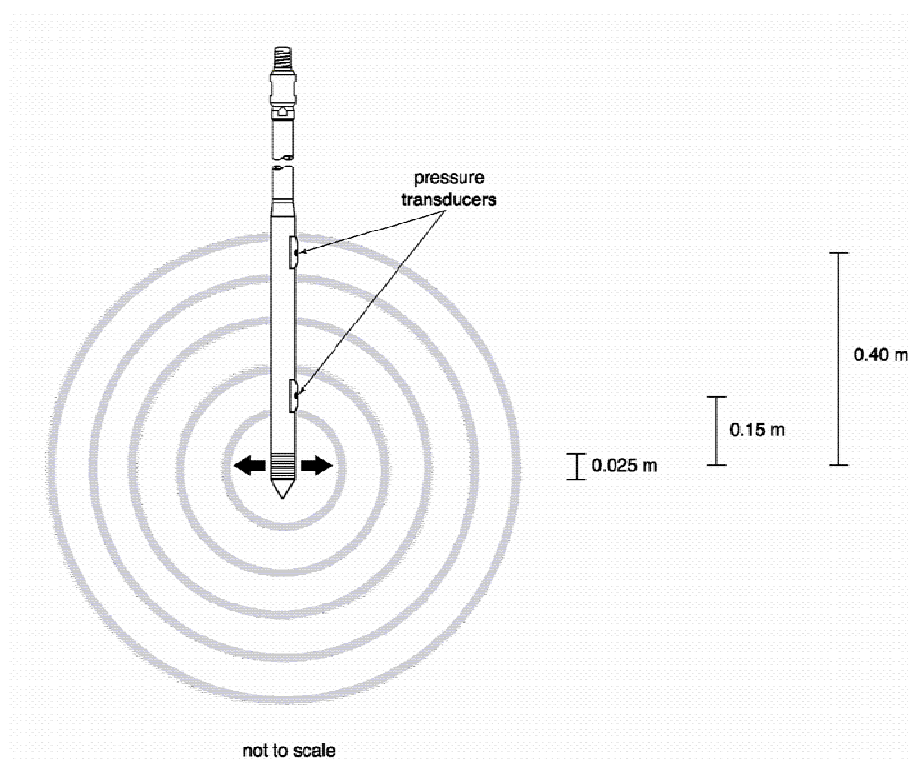
Figure 3.2: Schematic of direct-push permeameter (after Butler 2005).

mixtures formulation (Song et al. 1999; Voyiadjis and Song 2000; Voyiadjis and Song 2003). The pore pressures that develop around a moving penetrometer have been shown to be related to hydraulic conductivity under certain conditions (Elsworth and Lee 2005). In partially-drained penetration, K is inversely proportional to the excess pore pressure generated at the tip (p - p_s, where p is the total pore pressure and p_s is the static pore pressure) and directly proportional to the penetration rate (U), i.e. $K \propto U/(p - p_s)$. This relationship indicates that there is potential for estimating K during probe advancement without needing to stop and monitor the dissipation of pore pressures. Analysis methods based on this functional relation are described in the following section. The viability of these methods is then assessed through comparisons with independently obtained K estimates from the Nauen site.

3.4 Analysis

If the pore pressures that develop around the penetrometer tip during advancement can be linked to the hydraulic conductivity of the medium, it should be possible to relate K to the various quantities measured during a uCPT profile (henceforth, cone metrics). The prediction of K from pore pressures and other cone metrics is the objective of the on-the-fly methods investigated here. The theory underlying these methods is described in this section.

3.4.1 On-the-fly Methods

The pore pressure response to the advancement of a penetrometer may be approximated by a moving volumetric dislocation of infinitesimal size migrating within a saturated porous medium (Elsworth 1990). The steady fluid pressure distribution that

develops around the cone is equivalent to the pressure field produced by the continuous injection of fluid into the porous medium surrounding a spherical cavity (Figure 3.3). The constant injection of fluid volume per unit time is equivalent to the penetrometer advancement rate per unit time. For a penetrometer of diameter $2a$ advanced at rate U, the fluid volume injected per unit time (dV) is equal to $\pi a^2 U$. This flux is injected on the hemispherical shell of the cavity, at $r = a$, with the condition of no change in fluid pressure in the far field, or $p = p_s$ at $r \to \infty$ (Figure 3.3). Solving the spherically symmetric flow problem yields the following relationship (Elsworth and Lee 2005):

$$p - p_s = \frac{\gamma_w}{4\pi Ka} dV = \frac{Ua\gamma_w}{4K} \tag{3.1}$$

Equation (3.1) simply represents the pressure induced by fluid injection across the interior surface of the hemispherical shell at a rate equivalent to the displacement volume per unit time of the penetrometer (Figure 3.3). This solution is similar to that obtained for a moving point dislocation (Elsworth 1990), but improves upon that solution by including the critical effect of a finite size penetrometer. Note that this solution is unable to differentiate between pore pressures measured on the tip, shoulder, or shaft of the cone-shaped probe, as the actual probe geometry is not represented. Despite that limitation, however, the simplicity of the expression warrants further investigations of its potential for inclusion in an on-the-fly procedure for determination of hydraulic conductivity.

3.4.2 Cone Metrics

In a uCPT profile, pore fluid pressure, p, cone resistance, q_c, and sleeve friction, f_s, are measured continuously with depth (Figure 3.4). By convention, these three quantities are defined in dimensionless form as the pore pressure ratio, B_q, cone
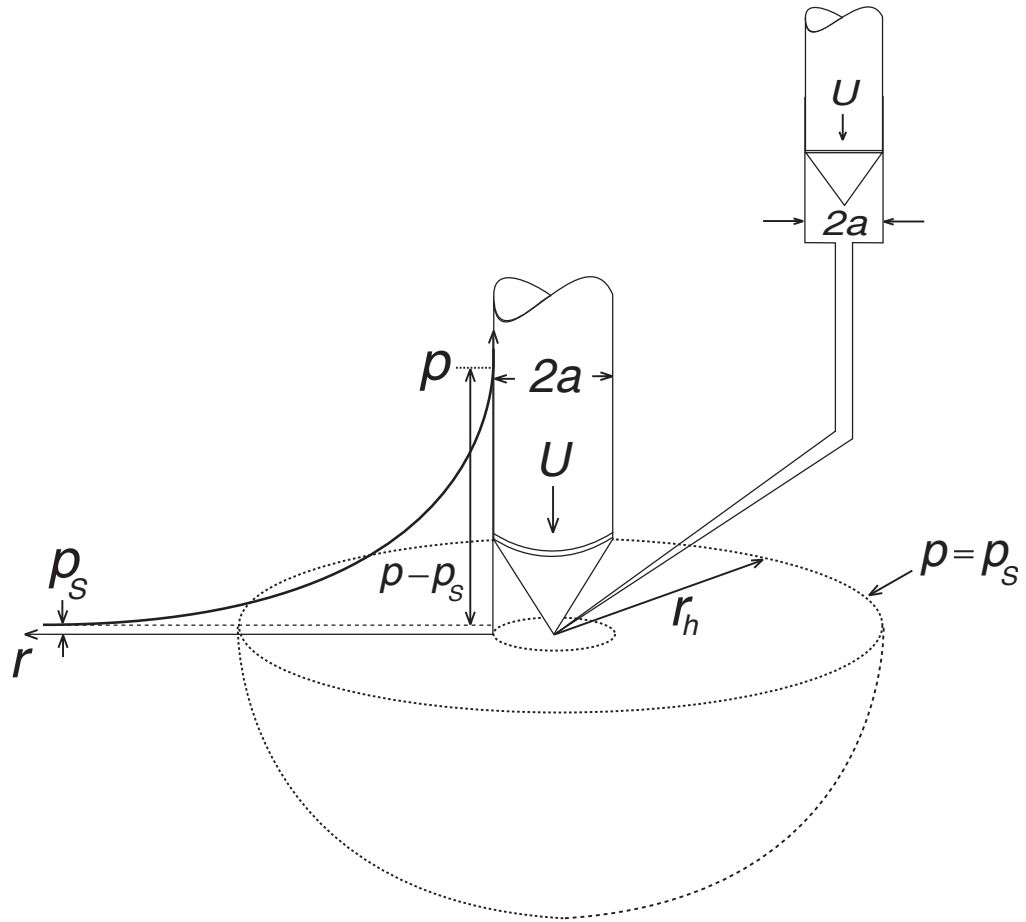
Figure 3.3: Geometry of the process zone surrounding an advancing penetrometer. Hydraulic behavior defined with pressure, p, induced at the tip, and remote pressure, p_s, at radius, ∞.
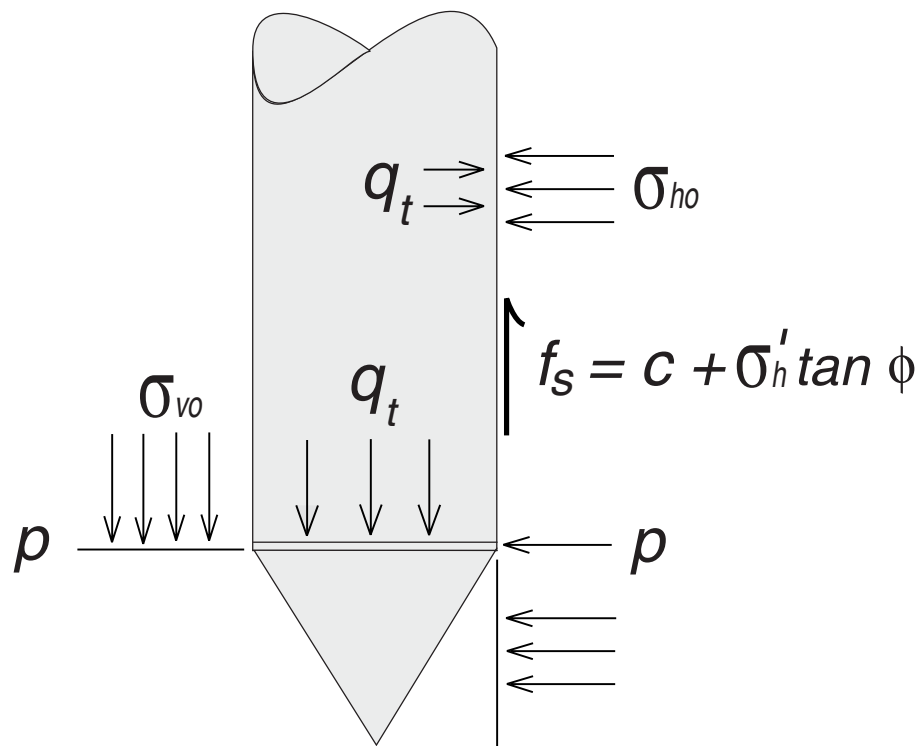
Figure 3.4: Tip local conditions. Cone expansion stress is q_t.

resistance, Q_t, and sleeve friction, F_r:

$$B_q = \frac{p - p_s}{q_t - \sigma_{vo}}; \qquad Q_t = \frac{q_t - \sigma_{vo}}{\sigma'_{vo}}; \qquad F_r = \frac{f_s}{q_t - \sigma_{vo}} \tag{3.2}$$

where q_t is the corrected cone resistance, f_s is the sleeve friction defined in units of

stress, σ_{vo} is the initial in situ vertical stress, and the prime denotes effective stress.

An expression for hydraulic conductivity in terms of these dimensionless parameters

can be obtained by manipulating equation (3.1). The penetration-induced excess pore

pressure, $p - p_s$, can be normalized by the initial vertical effective stress (Elsworth and

Lee 2005):

$$\frac{p - p_s}{\sigma'_{vo}} = \frac{Ua\gamma_w}{4K\sigma'_{vo}} = \frac{1}{K_D} \tag{3.3}$$

where K_D is the dimensionless hydraulic conductivity index ($K_D = (4K\sigma'_{vo})/(Ua\gamma_w)$).

The ratio $(p - p_s)/\sigma'_{vo}$ can be expressed in terms of the cone metrics of equation (3.2)

as

$$\frac{p - p_s}{\sigma'_{vo}} = \frac{p - p_s}{q_t - \sigma_{vo}} \frac{q_t - \sigma_{vo}}{\sigma'_{vo}} = B_q Q_t = \frac{1}{K_D} \tag{3.4}$$

This expression relates the pore pressure ratio, B_q and cone resistance, Q_t, to the

dimensionless hydraulic conductivity, K_D. Equation (3.4) can be rearranged as

$$K_D^{B_q - Q_t} = \frac{1}{B_q Q_t} \tag{3.5}$$

where the superscript designates the dimensionless cone metrics utilized in the relation.

Equation (3.5) can be used to develop cross plots of B_q and Q_t that can be contoured

for K_D as discussed later and shown in Figures 3.6 (a) and 3.7 (a). If B_q and Q_t are

known, hydraulic conductivity can be estimated from the K_D values as shown in the figures. The initial in-situ effective stress is the only unknown parameter required for estimation of K from these plots, and it can be calculated from the initial vertical stress and the static pore pressure. However, uncertainty can be introduced into the calculation because p_s may significantly deviate from the commonly assumed hydrostatic trend as will be discussed in a later section.

3.4.3 Controls on Tip-Local Stresses

Equation (3.5) is simply a rearrangement of equation (3.1) into a form utilizing conventional cone metrics. It is of interest to examine if other combinations of cone metrics can provide additional information about K. In particular, the derivation of an expression for K in terms of Q_t and F_r would be of value because the inclusion of a pore-pressure sensor on a CPT probe is not universal. This latter issue requires that the analysis for fluid flow around the penetrometer tip be extended to accommodate the cavity expansion stresses that accompany penetrometer advancement and that are embodied in Q_t and F_r. Two assumptions are selected as representative of field behavior for this extended analysis. The first is that lateral stresses at the sleeve are equal to the cavity expansion stress (Figure 3.5 (a)), i.e. $\sigma_h = q_t$. The second is that vertical total stresses in the tip process zone remain invariant with penetration (Figure 3.5 (b)), i.e. $\Delta\sigma_v = 0$ or $\sigma_v = \sigma_{vo}$. Analysis methods based on each of these assumptions are developed in the following sections.
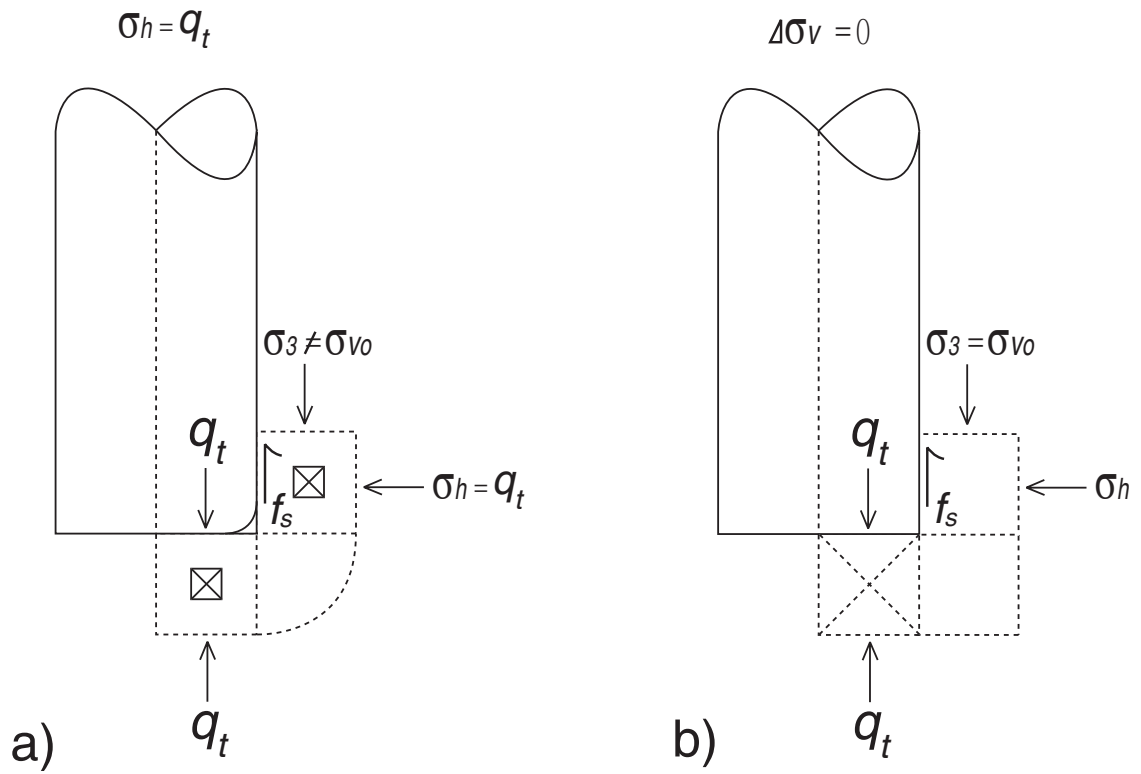
Figure 3.5: Geometry of tip-local stress. Two assumptions: (a) Horizontal stresses equal to cavity expansion stress, $\sigma_h = q_t$, and (b) Vertical stresses remain invariant, $\Delta\sigma_v = 0$.
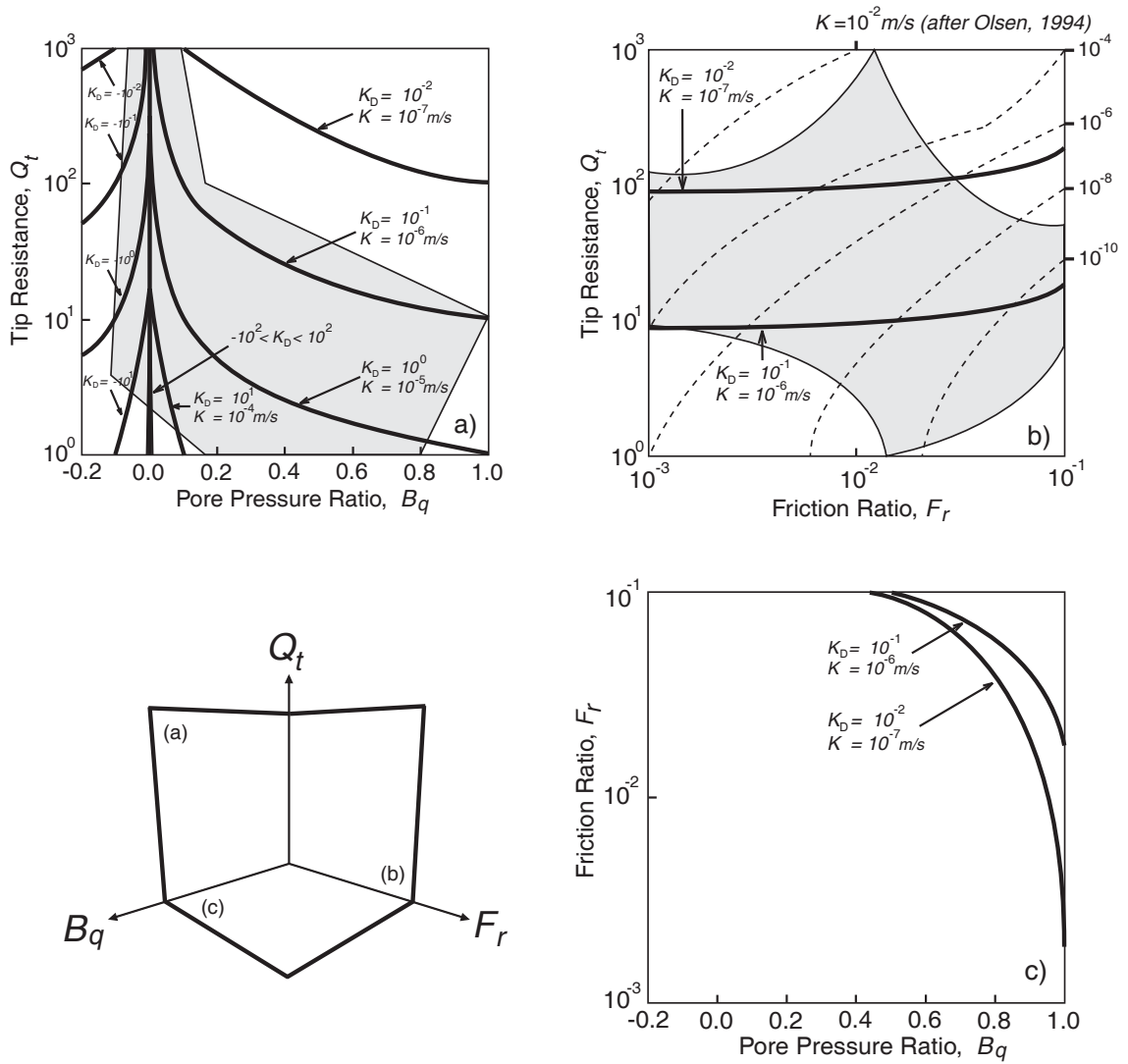
Figure 3.6: Plots of (a) $B_q - Q_t$, (b) $F_r - Q_t$, and (c) $B_q - F_r$ contoured for K_D for the assumption of horizontal stresses equal to the cavity expansion stress. Values of K are shown for a standard cone with $\sigma_{vo} = 100\,kPa$, and $U = 2\,cm/s$. The empirical results of (Olsen 1994) are shown dashed in (b), and the solid ranges of (Robertson 1990) are shown shaded in (a) and (b).

3.4.3.1 Horizontal Stresses Equal to Cavity Expansion Stress

For a frictional media ($c \rightarrow 0$), normalized sleeve friction, F_r, may be related to pore pressure by noting that $f_s = c + (\sigma_h - p)\tan\phi$, where c and ϕ are the material strength parameters. The insertion of the probe changes the horizontal stress. We assume that the total horizontal stress, σ_h, cannot exceed the cavity expansion stress, q_t, applied at the cone tip. Thus, $f_s = \frac{1}{N}(q_t - p)\tan\phi$, which substituted into equation (3.2) yields

$$F_r = \left(1 + \frac{1}{Q_t} - B_q\right)\frac{\tan\phi}{N} \tag{3.6}$$

where $N = \sigma_1'/\sigma_3'$, and σ_1' and σ_3' are the maximum and minimum principal stresses. Equation (3.6) enables the friction angle, ϕ, to be determined as a function of depth. As will be shown in section 5, field data indicate that the actual friction angle is severely under-predicted using equation (3.6). This suggests that the assumption that lateral stresses reach the cone expansion stress is an overestimate of the actual lateral stress.

In theory, measurements of sleeve friction may be used to further constrain estimates of hydraulic conductivity. Using $1/Q_t = B_q K_D$ from equation (3.5) enable equation (3.6) to be rewritten in terms of $B_q - F_r$ as

$$K_D^{B_q - F_r} = 1 + \frac{1}{B_q}\left(\frac{F_r N}{\tan\phi} - 1\right) \tag{3.7}$$

Similarly, substituting $B_q = 1/Q_t K_D$ into equation (3.6) yields

$$K_D^{F_r-Q_t} = \frac{1}{1-Q_t\left(\dfrac{F_r N}{\tan\phi}-1\right)}$$

(3.8)

Thus, , equations (3.5), (3.7), and (3.8) provide estimates of K_D derived from the three potential pairs of conventional cone metrics: $B_q - Q_t$, $B_q - F_r$, and $F_r - Q_t$. Cross plots of these parameters are given in Figure 3.6 for an assumed friction angle of $30°$.

3.4.3.2 Vertical Stresses Remain Invariant

For a frictional soil, where the cohesion has been destroyed by large deformations ($c \to 0$), the sleeve friction, f_s, may be defined as $f_s = (\sigma_h - p)\tan\phi$. Consistent with the destruction of cohesion in the process zone, the Mohr-Coulomb strength criterion may be defined in terms of principal stresses as $\sigma_1' = N\sigma_3' + 2c\sqrt{N}$ which reduces to $\sigma_1' = N\sigma_3'$ where $N = (1+\sin\phi)/(1-\sin\phi)$. Simple considerations of lower bound perfect plasticity yield $f_s = N(\sigma_{vo} - p)\tan\phi$, as identified in Figure 3.5 (b), and result in an alternative definition of sleeve friction:

$$F_r = N\tan\phi\left(\frac{1}{Q_t} - B_q\right).$$

(3.9)

The friction angle, ϕ, may be determined with probe depth using equation (3.9). As will be shown in the following section, field data indicate that more realistic predictions of friction angle can be obtained with equation (3.9) than with equation (3.6). Similar to the previous section, $1/Q_t = B_q K_D$ can be used to rewrite equation (3.9) in terms of $B_q - F_r$ as

$$K_D^{B_q-F_r} = \frac{F_r}{B_q N \tan \phi} + 1 .$$

<div align="right">(3.10)</div>

Substituting $B_q = 1/Q_t K_D$ into equation (3.9) yields

$$K_D^{F_r-Q_t} = \frac{1}{1 - \dfrac{F_r Q_t}{N \tan \phi}} .$$

<div align="right">(3.11)</div>

Thus, equations (3.5), (3.10), and (3.11) provide estimates of K_D derived from the three potential pairs of cone metrics. Cross plots of these three pairs of metrics are given in Figure 3.7 for an assumed friction angle of $30°$. Although a K estimate obtained from the $F_r - Q_t$ relationship does not explicitly depend on pore-pressure data, it will in practice because of the need to estimate the friction angle using equation (3.9).

Regardless of which assumption is used, the resulting cross plots indicate that there is a range of about three to four orders of magnitude (10^{-7} to $>10^{-4}$ m/s) over which K could potentially be determined with the on-the-fly approach. The lowermost limit is set by a physical limitation – for $K < 10^{-7} m/s$ pore pressures are generated by undrained loading of the soil – a process that does not involve the steady dissipation response around the tip and therefore cannot index hydraulic conductivity. However, the upper limit is ill-defined, as this is set only by the measurement resolution for excess pore pressures, and is not a limitation *per se*. Assessment of the viability of these predictive relationships requires comparison of K estimates derived from the cone metrics with estimates obtained using other approaches in the vicinity of the uCPT profiles. Such a comparison is described in the following section.
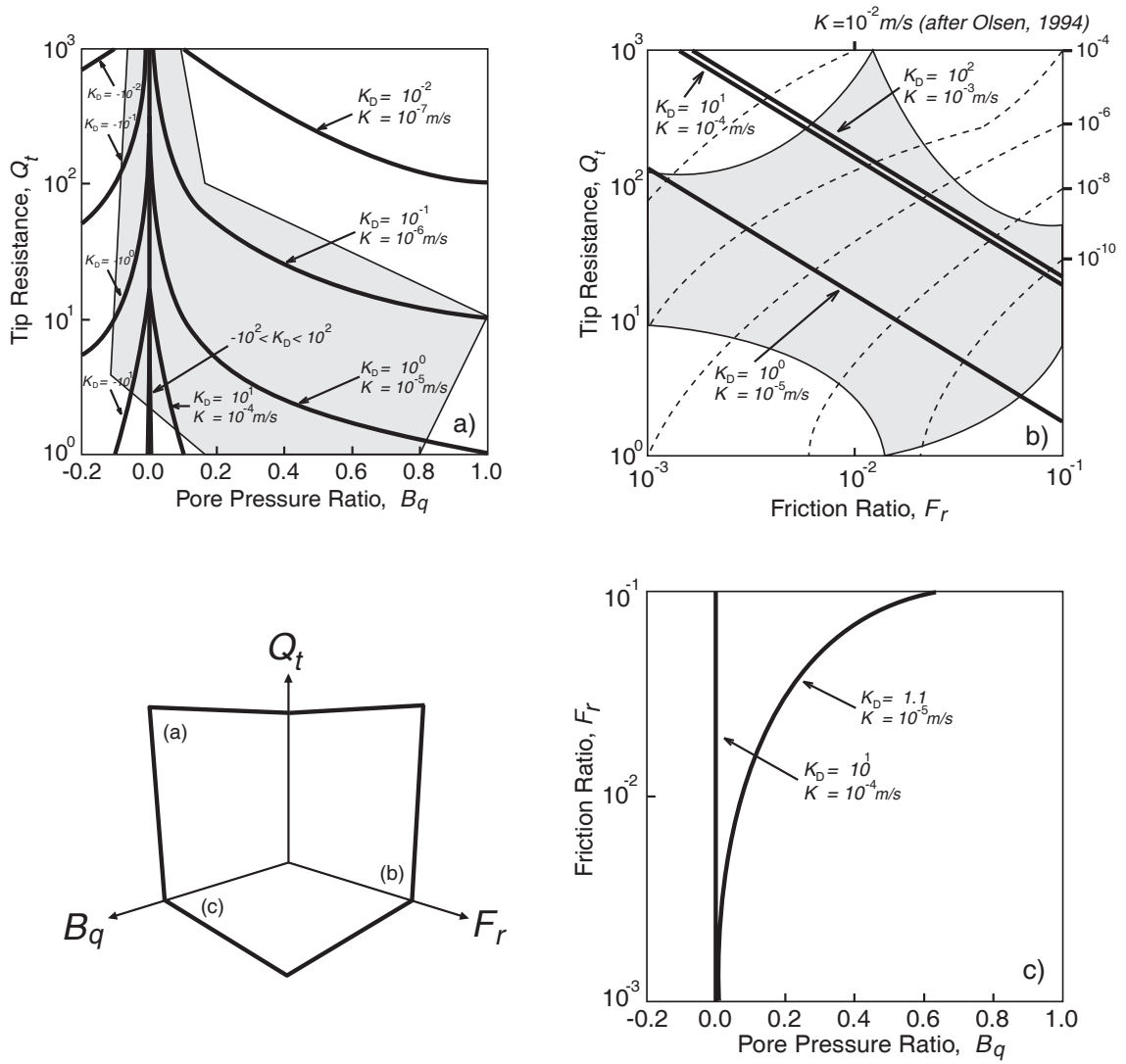
Figure 3.7: Plots of (a) $B_q - Q_t$, (b) $F_r - Q_t$, and (c) $B_q - F_r$ contoured for K_D for the assumption of vertical stresses remain invariant. Values of K are shown for a standard cone with $\sigma_{vo} = 100\,kPa$, and $U = 2\,cm/s$. The empirical results of (Olsen 1994) are shown dashed in (b), and the solid ranges of (Robertson 1990) are shown shaded in (a) and (b).

3.5   Available uCPT Data - Nauen Test Site

The two uCPT profiles performed at the Nauen test site, denoted Nauen 1 and Nauen 2, are presented in Figure 3.8. Both profiles were performed at the standard CPT advancement rate of 2 cm/s. As shown in Figure 3.9, friction angle, ϕ, estimates determined with equations (3.6) and (3.9) consistently under predict ϕ values obtained using empirical correlations based on results from a calibration chamber (Robertson and Campanella 1983).   However, the ϕ values determined with equation (3.9) are significantly closer to those calculated from the empirical correlations, indicating that the assumption of invariant vertical stresses may be more appropriate than that regarding horizontal stresses at the Nauen site. Therefore, in the following section, K profiles will be determined using relationships based on the assumption of an invariant vertical stress: $B_q - Q_t$ (equation (3.5)), $F_r - Q_t$ (equation (3.11)), and $B_q - F_r$ (equation (3.10)). These profiles will be compared to in-situ estimates of K (henceforth, K measurements) independently obtained at the Nauen site. In addition, K values determined using the traditional CPT classification charts (Robertson 1990) will be presented.

3.5.1   Comparison with Field Data

The profiles of cone resistance, sleeve friction, and pore pressure (measured immediately behind the cone in the cone-shoulder or u_2 position) presented in Figure 3.8 can be used to calculate dimensionless cone metrics. This requires information about the initial in-situ vertical stress (σ_{vo}) and the static pore pressure (p_s). The initial vertical stress is determined assuming a constant dry unit weight (γ_d) above the water table
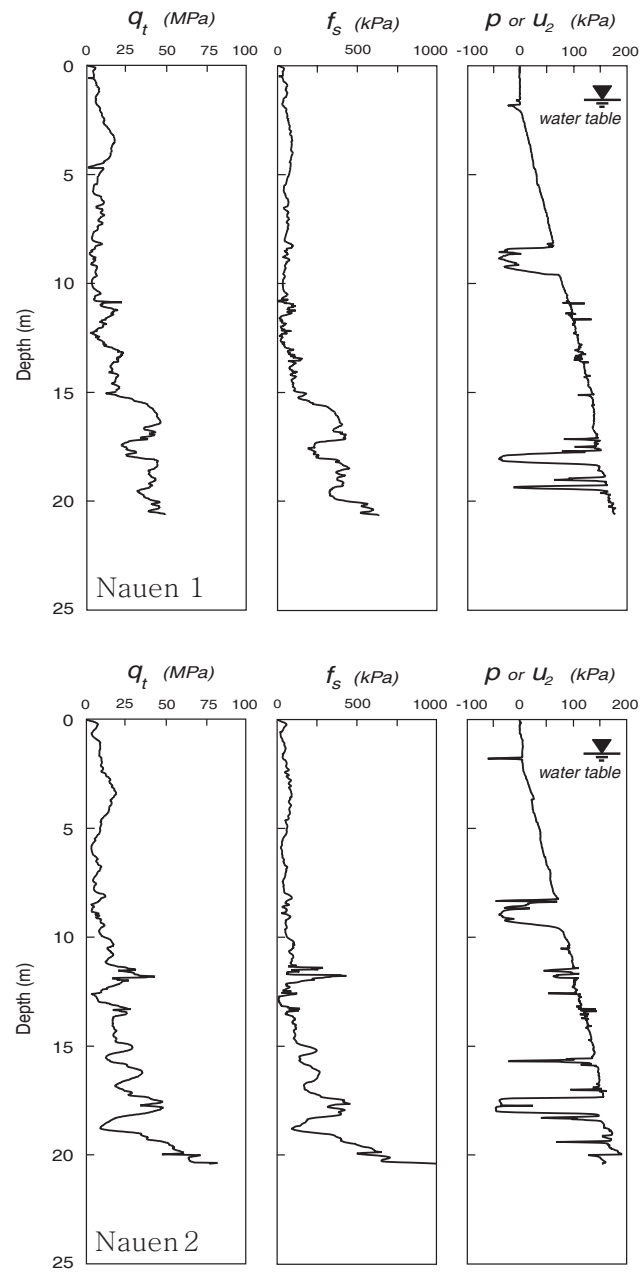
Figure 3.8: Profile data from the Nauen Test Site, Germany, defined by measured cone resistance, q_t, sleeve friction, f_s, and total pore pressure measured at the cone shoulder (u_2, or p in this analysis).
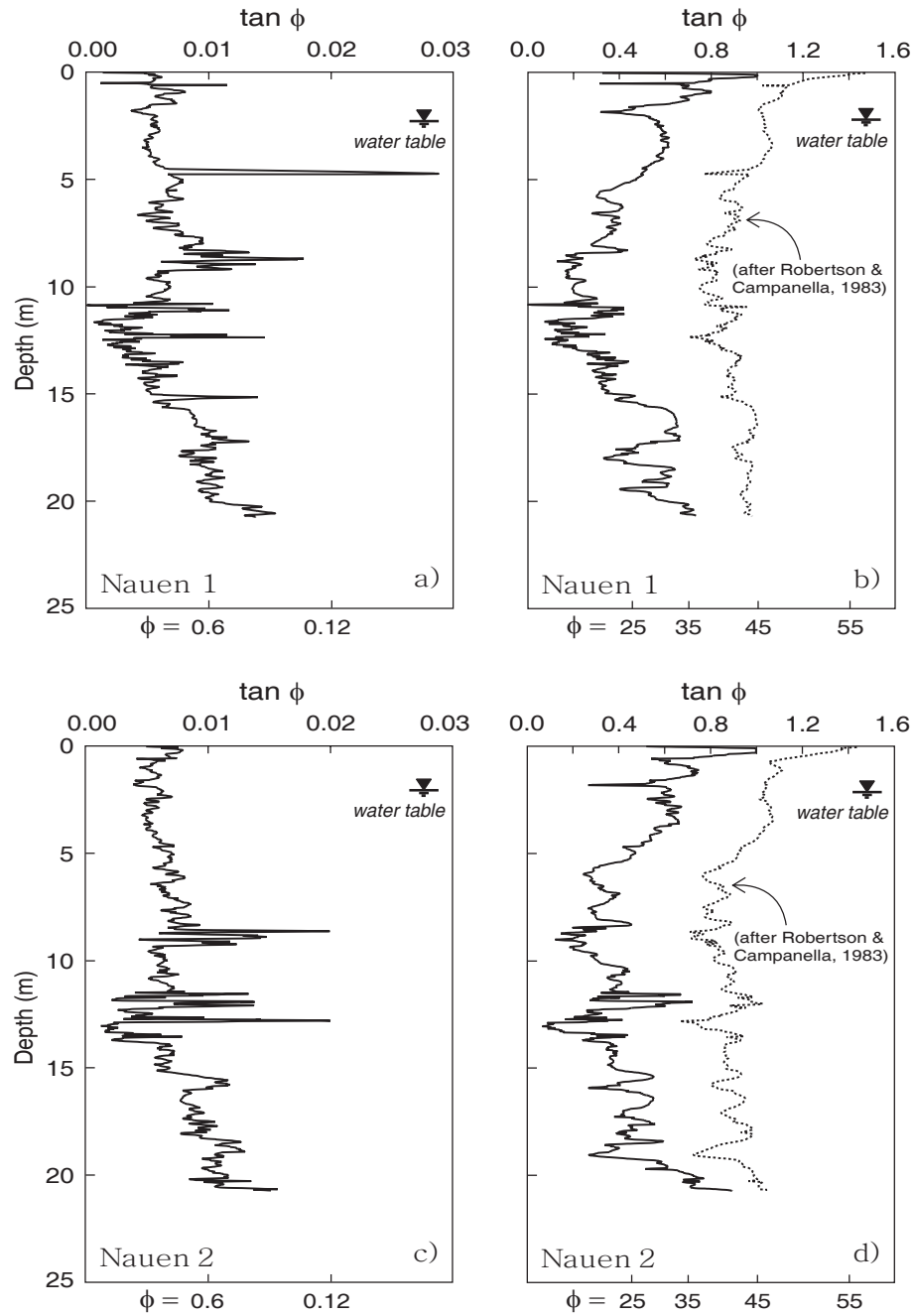
Figure 3.9: Plots of predicted friction angle (ϕ) with depth at the Nauen Test Site. Friction angle profiles are determined through equation (3.6) for (a) and (c) and equation (3.9) for (b) and (d). Dotted lines in (b) and (d) represent friction angle determined from empirical correlations based on calibration chamber test results (Robertson and Campanella 1983).

(assumed 1.82 m below land surface) and a constant saturated unit weight (γ_s) below. A hydrostatic pressure trend is additionally assumed for the calculation of p_s. The dimensionless cone metrics are used to determine the dimensionless hydraulic conductivity index, K_D, from the $B_q - Q_t$ (equation (3.5)), $F_r - Q_t$ (equation (3.11)), and $B_q - F_r$ (equation (3.10)) relationships, with the friction angle arbitrarily set to a constant value of $30°$ for the latter two relationships. Hydraulic conductivity can then be calculated from the definition of K_D. The K values calculated in this manner are plotted in Figures 3.10 and 3.11 for profiles Nauen 1 and Nauen 2, respectively. Note that there are intervals in both profiles for which no K values could be determined using the $B_q - Q_t$ and $B_q - F_r$ relationships as a result of negative excess pore pressures. These calculated negative excess pressures were primarily due to three factors: 1) dilatant silts; 2) uncertainty in the water-table position; and 3) negative deviations from the assumed hydrostatic pressure trend with depth. The negative excess pressures produced by dilant silts are particularly pronounced at depths of 9 and 18 m in both profiles (Figure 3.8).

Hydraulic conductivity measurements obtained from slug tests, DPP profiling, and correlations with grain-size data are also plotted in Figures 3.10 and 3.11. These values lie mostly between 10^{-4} to 10^{-3} m/s, except in the vicinity of the apparent dilant silt layer at around 9 m where slug test and DPP values of 10^{-7} m/s were obtained. The K range given by the classification charts of Robertson (1990) is also plotted for both profiles.
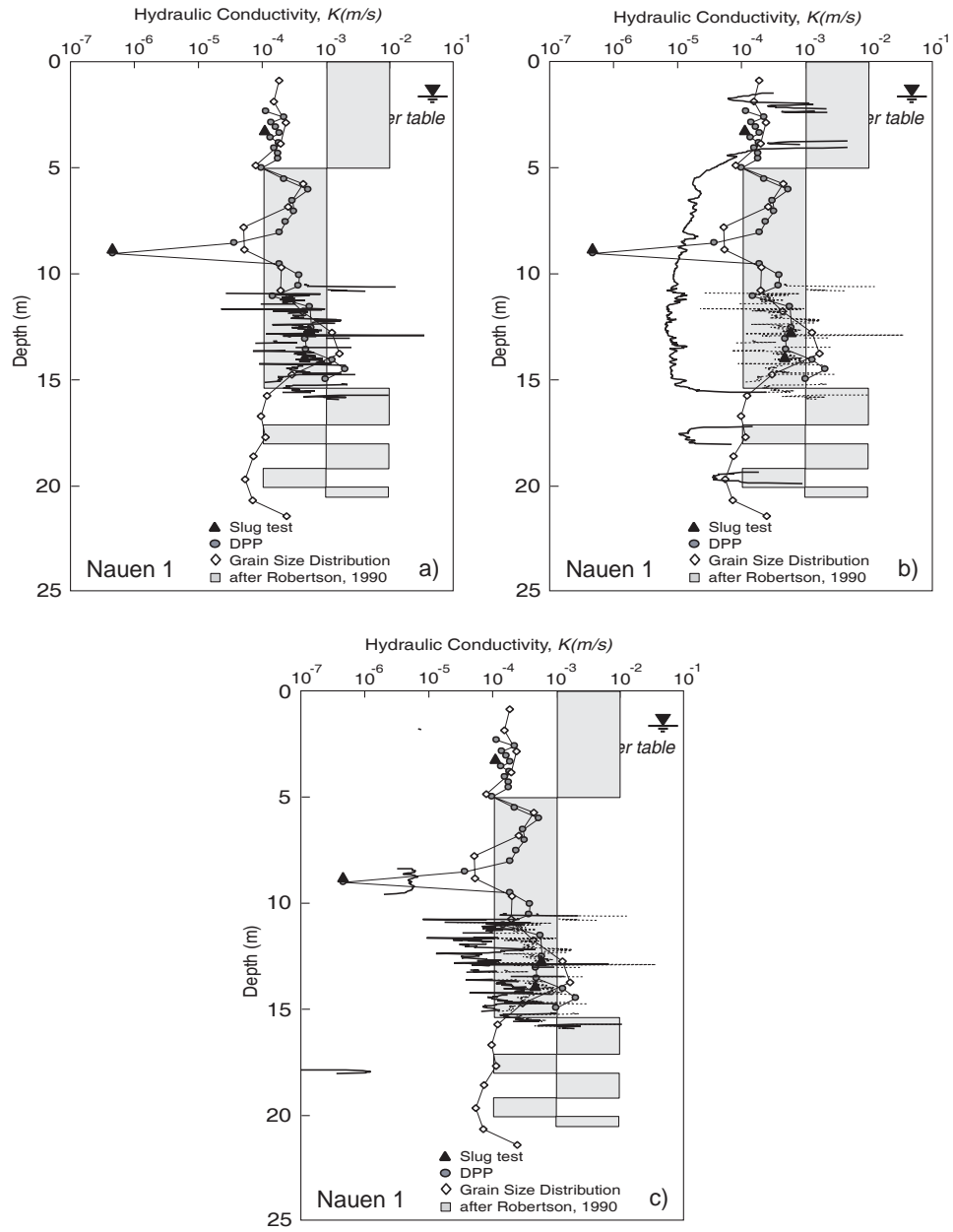
Figure 3.10: Plots of predicted hydraulic conductivity with depth at the Nauen Test Site, Nauen 1. hydraulic conductivity profiles are determined from the data pairs (a) $B_q - Q_t$ (equation (3.5)), (b) $F_r - Q_t$ (equation (3.11)), and (c) $B_q - F_r$ (equation (3.10)) for assumed $\phi = 30^o$ (solid line). Dotted lines in (b) and (c) represent hydraulic conductivity determined for friction angles obtained using equation (3.9).
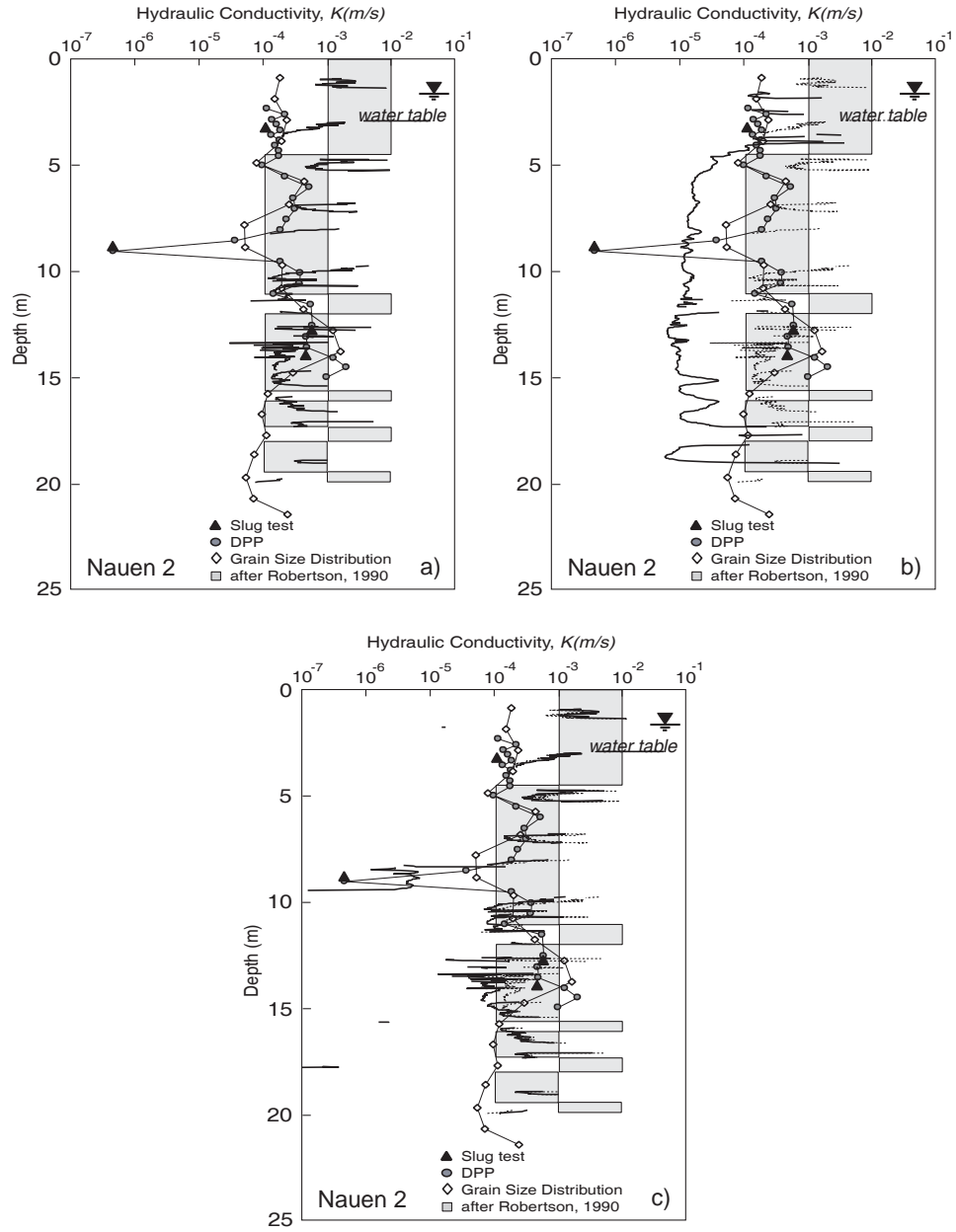
Figure 3.11: Plots of predicted hydraulic conductivity with depth at the Nauen Test Site, Nauen 2. hydraulic conductivity profiles are determined from the data pairs (a) $B_q - Q_t$ (equation (3.5)), (b) $F_r - Q_t$ (equation (3.11)), and (c) $B_q - F_r$ (equation (3.10)) for assumed $\phi = 30^o$ (solid line). Dotted lines in (b) and (c) represent hydraulic conductivity determined for friction angles obtained using equation (3.9).

3.5.1.1 Nauen 1 Comparison

No K estimates could be obtained above 8 m using the $B_q - Q_t$ or $B_q - F_r$ relationships for the Nauen 1 profile. Uncertainty about the position of the water table and the pressure trend with depth are undoubtedly the primary reasons for the absence of K estimates based on pore-pressure data. Below the apparent dilant silt interval at 9 m, the uCPT-derived estimates of K span the range of the in-situ K measurements but are primarily lower than those measurements. No uCPT K estimates could be obtained below 16 m for the Nauen 1 profile. Negative deviations from the assumed hydrostatic pressure trend are considered most likely responsible for the absence of K estimates in this interval.   Hydraulic conductivity estimates obtained from the $F_r - Q_t$ relationship are significantly lower than the in-situ measurements, indicating that little information can be gained about K with this relationship. Estimates based on the $B_q - F_r$ and $F_r - Q_t$ relationships were obtained for a friction angle arbitrarily set to $30°$.   If equation (3.9) is used to determine the friction angle, the K estimates are the same as those obtained from the $B_q - Q_t$ relationship, as shown by the dashed line in Figures 3.10 (b) and 3.10 (c) and as would be expected from the theoretical development described earlier. Estimates based on the classification charts are within one order of magnitude of the in-situ measurements over much of the profile. The largest difference occurs in the vicinity of the dilatant silt.

3.5.1.2 Nauen 2 Comparison

Estimates of hydraulic conductivity could be obtained for some intervals above 8 m using the $B_q - Q_t$ or $B_q - F_r$ relationships in the Nauen 2 profile. These estimates are

almost all higher than the in-situ measurements. Below the dilant silt interval at around 9 m, the uCPT-derived estimates of K again span the range of the in-situ K measurements. Between 12 and 15 m, these estimates are primarily lower than those measurements. In the other intervals, the estimates are primarily higher. In contrast to the Nauen 1 profile, uCPT K estimates could be obtained for some intervals below 16 m. Estimates obtained from the $F_r - Q_t$ relationship are again significantly lower than the in-situ measurements, reinforcing the point that little information about K can be gained with this relationship in the absence of pore-pressure data. Estimates based on the classification charts are again within one order of magnitude of the in-situ measurements over much of the profile.

3.5.1.3 Overall Comparison

A quantitative comparison between on-the-fly K estimates and in-situ measurements requires information at equivalent depths. The DPP measurements are assumed to represent the average hydraulic conductivity of the 0.25-m interval between the two transducers (Figure 3.2) with the reported depth being the midpoint of that interval. The uCPT K estimates, however, are reported at 0.02-m intervals. Thus, for comparison purposes, the arithmetic average of the uCPT estimates is taken over the interval of the DPP measurement (comprised of 13 uCPT estimates). Figure 3.12 displays DPP-measured K values with the average uCPT estimates from equation (3.5) for those same intervals. Only intervals for which at least one-half (7 or more) of the 13 potentially available uCPT estimates could be calculated were considered. There were only a total of 19 intervals from the two uCPT profiles that could be used in the comparison because of the negative excess pressures discussed earlier. Table 3.1 presents
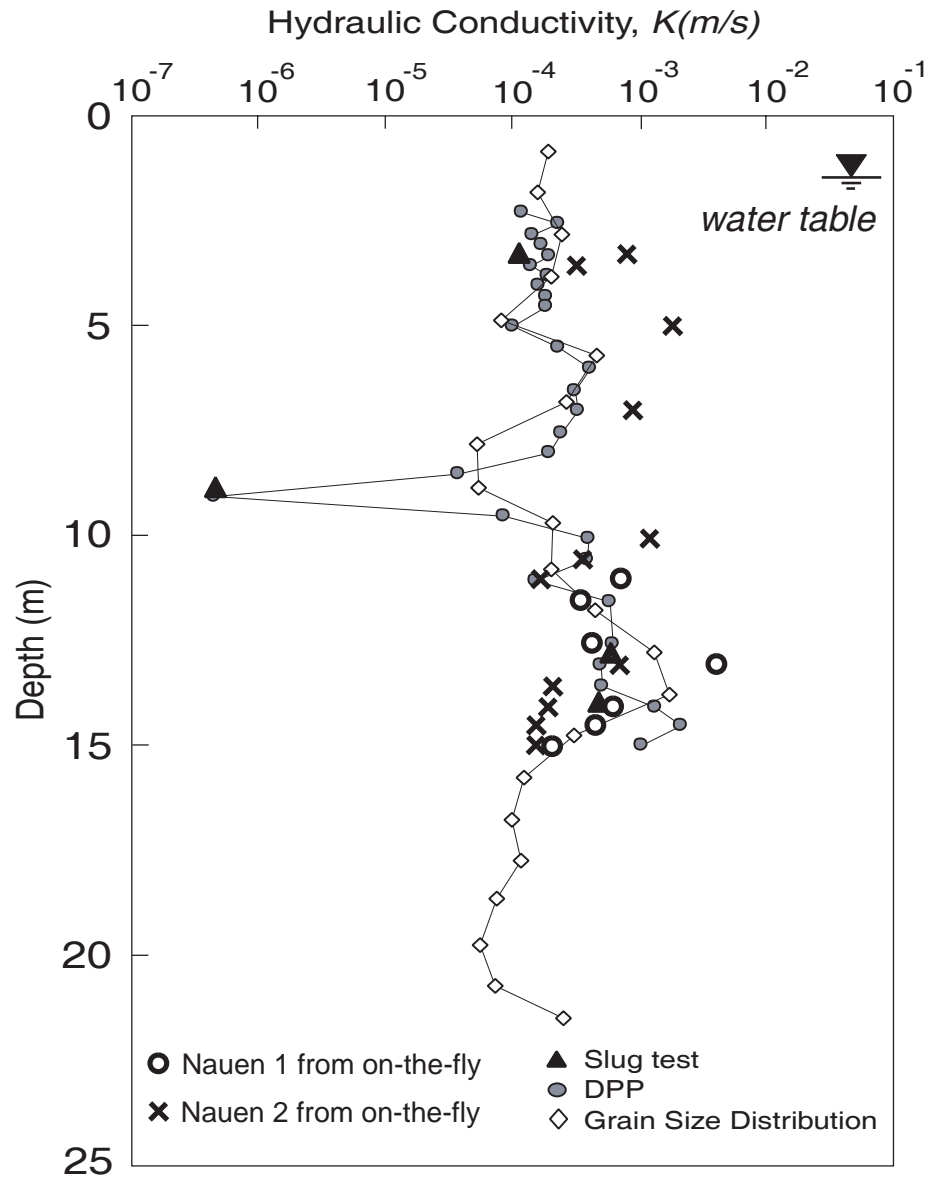
Figure 3.12: Hydraulic conductivity measurements determined by the direct-push permeameter (DPP) versus depth at the Nauen Test Site. Nauen 1 and Nauen 2 *K* estimates determined from equation (3.5) for the same intervals are plotted where available. Vertical dimension of plotted symbols is equal to the averaging interval (0.25 m).

Table 3.1 Comparison of Profile and Overall Averages

	Number of Test Intervals	Average On-the-fly K Estimates (m/s)	Average of DPP K Estimates (m/s)	Average of Absolute Differences of On-the-fly and DPP K (m/s)
Nauen 1	7	1.1×10^{-3}	9.8×10^{-4}	1.2×10^{-3}
Nauen 2	12	6.3×10^{-4}	6.4×10^{-4}	7.7×10^{-4}
Overall	19	8.6×10^{-4}	8.1×10^{-4}	1.0×10^{-3}

the details of the comparison. On average, the K predicted from the on-the-fly methodology is close to that of the DPP measurements (overall average uCPT-predicted K is 6% higher than the average DPP-predicted K). However, the prediction of K at any given depth is much less congruent between DPP and uCPT methods as shown by the overall average absolute difference that is 16% larger than the average uCPT-predicted K.

3.5.2 Discussion

Figures 3.6 and 3.7, consistent with earlier work (Elsworth 1993; Voyiadjis and Song 2003; Elsworth and Lee 2005), indicate that on-the-fly methods have potential for estimation of K in the interval from 10^{-7} to $>10^{-4}$ m/s. The vast majority of the K measurements available at the Nauen site are at the upper end of this range. In addition, the K measurements at the lower end of the interval were obtained in an apparent dilant silt layer for which the proposed methodology is not valid. Thus, the Nauen data are not ideal for examining this methodology over its full range of potential applicability. Despite that limitation, some insight can be obtained regarding the potential and limitations of the proposed approach.

Hydraulic conductivities recovered from the DPP tests can be compared systematically with those predicted from $K_D = 1/B_q Q_t$ for the Nauen 1 and 2 soundings, as illustrated in Figure 3.13 (a) and (b). DPP measured hydraulic conductivities, converted to $K_D = (4K\sigma'_{vo})/(Ua\gamma_w)$, are plotted on the horizontal ordinate. Measurements cluster around the relation $K_D = 1/B_q Q_t$, with the data for the closer Nauen 1 sounding being most tightly clustered (Figure 3.13 (a)). All data are within a one order-of-
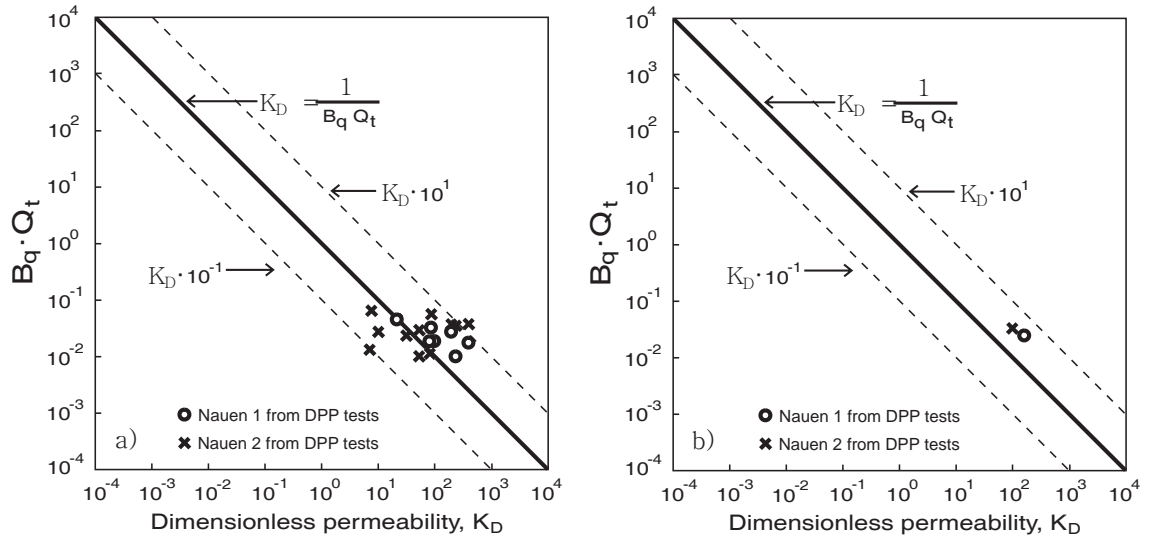
Figure 3.13: a) Selected hydraulic conductivity magnitudes determined from DPP tests adjacent to soundings Nauen 1 (circles) and Nauen 2 (crosses), compared with the relation $K_D = 1/B_q Q_t$. b) Ensemble data of (a) represented as mean magnitudes.

magnitude spread either side of the theoretical relation, $K_D = 1/B_q Q_t$. These show general agreement with the relation $K_D = 1/B_q Q_t$, illustrating a strong correlation between the calculated K_D values evaluated from $B_q Q_t$, and those measured by DPP. The predictions yielded by the data pair $B_q - Q_t$ provide the most robust evaluation in this comparison, as apparent in Figures 3.10 (a) and 3.11 (a).

The similarity of the K averages reported in Table 3.1 indicates that some useful information about hydraulic conductivity can be gained from an on-the-fly evaluation approach based on equation (3.5). Outside of dilant silt intervals, the primary limitation of the approach appears to be the need for information about the static pressure in the formation. Currently, the water table position and an assumed hydrostatic pressure trend with depth are used to estimate p_s. That approach, however, will introduce considerable uncertainty into K estimates for relatively permeable intervals in vertically heterogeneous sequences and/or in the presence of a significant component of vertical flow. In heterogeneous unconsolidated sequences, it is not uncommon to have pressure head differences much greater than hydrostatic over thin intervals of relatively low hydraulic conductivity that serve as confining layers. For example, Schulmeister et al. (2003) report a greater than 0.9-m pressure head difference over a 1-m thick clay layer. Similarly, pressure head changes significantly different from hydrostatic can be found in the vicinity of ground-water discharge and recharge areas (Hubbert 1940). Such differences can introduce considerable uncertainty into K estimates for the range observed at the Nauen site because of the relatively small pressures generated during probe advancement. One approach to reduce this uncertainty is to periodically suspend penetration and monitor the dissipation of pressures back to static conditions, i.e. perform a dissipation test, in the relatively permeable intervals. This additional step would not

add much time to the profiling procedure because the pressures would return to static in a matter of seconds or, at most, a few minutes. In less-permeable intervals, the uncertainty in p_s is of little importance because of the large pressures generated during probe advancement.

The results of the Nauen comparison also indicate that little information about hydraulic conductivity can be obtained from the cone-metric relationships without use of pore-pressure data. For CPT profiles performed without a pressure sensor, the classification charts of Robertson (1990) appear to provide K estimates that are, on average, more consistent with the K measurements at the Nauen site than estimates obtained from equation (3.11) in the absence of pore-pressure data.

Further work is clearly needed to fully assess the potential of the proposed on-the-fly methodology. In particular, a comparison is needed in sequences in which K primarily lies in the $10^{-7} \sim 10^{-4}$ m/s range. As was done at the Nauen site, the comparisons should involve in-situ measurements that have been carefully performed. Butler (2005) describes one site that has considerable potential for use in such a comparison.

3.6 Conclusions

Recently, solutions have been proposed for the pressure field that develops in the vicinity of an advancing penetrometer. These solutions can serve as the basis of a method for predicting hydraulic conductivity (K) from the pore pressures recorded by a sensor on a uCPT probe without the need for suspending probe advancement. Theoretical developments have shown that this "on-the-fly" methodology for estimation of K could potentially be applied over a range in K from $10^{-7} \sim >10^{-4}$ m/s. The viability of this approach was evaluated at an unusually well characterized field site near Berlin,

Germany. Hydraulic conductivity estimates based on pore-pressure data from a uCPT probe compared reasonably with independent measurements of K taken from slug tests, direct-push permeameter (DPP) profiling, and grain-size correlations. The overall average of the uCPT K estimates was only 6% higher than that from the DPP profile. However, the average absolute difference between values obtained over the same depth interval with these two approaches was 16% larger than the average uCPT-predicted K value, indicating that there is a measurable difference in these predictions for any given interval. The K range for the majority of the intervals used in this assessment was $10^{-4} \sim 10^{-3}$ m/s, near the upper end of the theoretical range of applicability of the proposed methodology. Given that the approach was applied in the vicinity of the upper end of its range of applicability, the results of this comparison must be considered promising. Estimation of hydraulic conductivity in the absence of pore-pressure data appears less promising. In that case, the classification charts of Robinson were found to be the best option for obtaining K estimates from CPT data collected on-the-fly.

In addition to the assumptions underlying the theoretical development on which the method is based, the major uncertainty in the uCPT K estimates was introduced by the lack of information about the pressure trend with depth. This uncertainty can be reduced by periodically suspending penetrometer advancement in relatively permeable intervals and determining the static pressure. Cessation of advancement will not be necessary in less permeable intervals because the magnitude of the uncertainty in the static pressure will be very small in comparison to the magnitude of the pressure induced by probe advancement. This field comparison indicates that the "on-the-fly" approach has promise for providing reasonable estimates of small-scale variations in K over a limited range

of hydraulic conductivity.

Acknowledgements

Notation

$a = $ penetrometer radius; L

$c = $ cohesion; FL^{-2}

$c_v = $ coefficient of consolidation; L^2T^{-1}

$dV = $ volume change per unit time in the tip process zone; L^3T^{-1}

$f_s = $ magnitude of sleeve friction; FL^{-2}

$K = $ hydraulic conductivity; LT^{-1}

$m_v = $ coefficient of volume compressibility, $F^{-1}L^2$

$N = $ coefficient which describe the relation between maximum and minimum principal stress; -

$p = $ absolute pore fluid pressure (u_2); FL^{-2}

$p_s = $ initial static fluid pressure; FL^{-2}

$p - p_s = $ excess pore pressure; FL^{-2}

$q_c = $ measured cone resistance; FL^{-2}

$q_t = $ corrected cone resistance, $q_c + (1 - a_n)(p - p_s)$; FL^{-2}

$U = $ penetrometer penetration rate; LT^{-1}

$\gamma_d = $ dry unit weight of water; FL^{-3}

$\gamma_s = $ saturated unit weight of water; FL^{-3}

$\gamma_w = $ unit weight of water; FL^{-3}

$\sigma_h = $ total horizontal stress; FL^{-2}

σ_v = total vertical stress; FL^{-2}

$\sigma_{ho}, \sigma'_{ho}$ = initial horizontal stress and effective stress; FL^{-2}

$\sigma_{vo}, \sigma'_{vo}$ = initial vertical stress and effective stress; FL^{-2}

σ'_1, σ'_3 = maximum and minimum principal stress; FL^{-2}

ϕ = friction angle; −

B_q = dimensionless pore pressure ratio, $(p - p_s)/(q_t - \sigma_{vo})$; −

K_D = dimensionless hydraulic conductivity, $(4K\sigma_{vo})/(Ua\gamma_w)$; −

$K_D^{B_q - Q_t}$ = dimensionless hydraulic conductivity determined from $B_q - Q_t$ data; −

$K_D^{F_r - Q_t}$ = dimensionless hydraulic conductivity determined from $F_r - Q_t$ data; −

$K_D^{B_q - F_r}$ = dimensionless hydraulic conductivity determined from $B_q - F_r$ data; −

Q_t = dimensionless cone resistance, $(q_t - \sigma_{vo})/\sigma_{vo}$; −, and

F_r = dimensionless friction factor, $f_s/(q_t - \sigma_{vo})$. −

References

Butler, J. J. (2002). "A simple correction for slug tests in small-diameter wells." Ground Water 40(3): 303-307.

Butler, J. J. (2005). Hydrogeological methods for estimation of hydraulic conductivity. in Hydrogeophysics, edited by Y. Rubin and S. Hubbard, Kluwer, in press.

Butler, J. J. and P. Dietrich (2004). New methods for high-resolution characterization of spatial variations in hydraulic conductivity. International Symposium on Hydrogeological Investigation and Remedial Technology, National Central University, Jhongli, Taiwan.

Butler, J. J., J. M. Healey, et al. (2002). "Hydraulic tests with direct-push equipment." Ground Water 40(1): 25-36.

Campanella, R. G. and P. K. Robertson (1988). Current status of the piezocone test. Penetration Testing 1988, Orlando.

Dietrich, P., J. J. Butler, et al. (2003). Field comparison of direct-push approaches for determination of K profiles. American Geophysical Union, San Francisco.

Douglas, B. J. and R. S. Olsen (1981). Soil classification using electric cone penetrometer. Symposium on cone penetration testing and experience, St. Louis, Geotechnical engineering division, ASCE.

Elsworth, D. (1990). " Theory of partially drained piezometer insertion." Journal of Geotechnical Engineering 116(6): 899-914.

Elsworth, D. (1991). "Dislocation analysis of penetration in saturated porous media." Journal of Engineering Mechanics 117(2): 391-408.

Elsworth, D. (1992). "Pore pressure response due to penetration through layered media."

International Journal for Numerical and Analytical Methods in Geomechanics 16: 45-64.

Elsworth, D. (1993). " Analysis of piezocone dissipation data using dislocation methods." Journal of Geotechnical Engineering 119(10): 1601-1623.

Elsworth, D. (1998). "Indentation of a sharp penetrometer in a poroelastic medium." International Journal of Solids and Structures 35(34-35): 4895-4904.

Elsworth, D. and D. S. Lee (2005). "Permeability determination from On-the-fly piezocone sounding." Journal of Geotechnical and Geoenvironmental Engineering 131(5): 643-653.

Hazen, A. (1930). Water supply. New York, Wiley.

Hubbert, M. K. (1940). "The theory of ground-water motion." Journal of Geology 48(8): 785-944.

Lee, D. S. and D. Elsworth (2004). "Indentation of a Free-Falling Sharp Penetrometer into a Poroelastic Seabed." Journal of Engineering Mechanics 130(2): 170-179.

Lunne, T., P. K. Robertson, et al. (1997). Cone Penetration Testing in Geotechnical Practice, Blackie Academic.

Mitchell, J. K. and T. L. Brandon (1998). Analysis and use of CPT in earthquake and environmental engineering. Geotechnical Site Characterization, Balkema, Rotterdam.

Robertson, P. K. (1990). "Soil classification using the cone penetration test." Canadian Geotechnical Journal 27(1): 151-158.

Robertson, P. K. and R. G. Campanella (1983). "Interpretation of cone penetration tests: Part I: Sand." Canadian Geotechnical Journal 20(4): 719-733.

Robertson, P. K., R. G. Campanella, et al. (1986). Use of piezometer cone data. Proc. ASCE Spec. Conf. In Situ '86. Use of In Sit Tests in Geotechnical Engineering, Blacksburg, 1263-1280.

Robertson, P. K., J. P. Sully, et al. (1992). "Estimating coefficient of consolidation from piezocone tests." Canadian Geotechnical Journal 29(4): 539-550.

Schulmeister, M. K., J. J. Butler, Jr., et al. (2003). "Direct-push electrical conductivity logging for high-resolution hydrostratigraphic characterization." Ground Water Moint. and Remed 23(3): 52-62.

Song, C. R., V. G. Z., et al. (1999). "Determination of permeability of soils using the multiple piezo-element penetrometer." International Journal for Numerical and Analytical Methods in Geomechanics 23(13): 1609-1629.

Voyiadjis, G. Z. and C. R. Song (2000). "Finite strain anisotropic Cam Clay model with plastic spin. II: Application to piezocone test." Journal of Engineering Mechanics 126(10): 1020-1026.

Voyiadjis, G. Z. and C. R. Song (2003). "Determination of hydraulic conductivity using piezocone penetration test." International Journal of Geomechanics 3(2): 217-224.

Chapter 4: Hydraulic Conductivity Measurement from On-the-fly uCPT Sounding and from VisCPT

Abstract

Detailed profiles of hydraulic conductivity are recovered from the deployment of direct-push permeameters at the Geohydrologic Experimental and Monitoring Site (GEMS), Kansas. Measurements with thin tapered tips, and with standard uCPT tips, show only minor differences, suggesting that sample disturbance effects are small, and that routine uCPT measurements are therefore representative of pristine conditions. Permeameter measurements are correlated against co-located uCPT measurements, estimates of permeability from on-the-fly correlations, and from grain size correlations derived from both VisCPT and from cone metrics. On-the-fly evaluations of hydraulic conductivity require that the tip-local pressure field is both steady and partially drained. Continuous penetration is shown to yield pore pressures sufficiently close to steady to enable conductivities to be determined, directly. Cone metrics of end bearing, of sleeve friction, and of pore pressure ratio, are shown sufficient to discriminate between partially drained and undrained behavior, and therefore to define the permissible regime where conductivities may be determined from on-the-fly data. Estimates of hydraulic conductivities from on-the-fly data are shown to correlate closely with independently measured magnitudes. Hydraulic conductivities are consistently under-predicted, suggesting that storage effects, the inability to reach a steady state, or the effects of dilation may influence the response. Profiles of hydraulic conductivities evaluated from the on-the-fly method also correlate well with the permeameter measurements. Predictions from soil classification, and from VisCPT methods are also capable of

estimating conductivities, with soil classifications giving the closest correlations in this particular suite of data.

4.1 Introduction

Cone penetration testing (uCPT) is a rapid and robust method for determining the mechanical and transport properties of soils, and the distribution of contaminants in the ground (Mitchell and Brandon 1998). In a standard uCPT test, a conically-tipped probe (penetrometer) is pushed into the ground at a constant penetration rate of $2\,cm/s$. Depth-continuous measurements are made of the resistance to penetration, q_t, of the frictional resistance of a trailing sleeve, f_s, and of the penetration-induced pore-fluid pressure, p, immediately above the cone tip (Lunne, Robertson et al. 1997). The vision cone penetration test (VisCPT) (Raschke and Hryciw 1997; Hryciw, Ghalib et al. 1998) significantly improves the resolving capabilities of the uCPT by providing a continuous visual record of the penetration log. Current uCPT methods for determining hydraulic conductivity in the soil are primarily based on the dissipation test (Robertson, Sully et al. 1992; Burns and Mayne 1998), which involves temporarily suspending penetrometer advance and monitoring the dissipation of the penetration-induced pore pressures. Dissipation tests are complemented by other direct-push methods of deploying permeameters, and of then conducting, slug tests (Butler 2002; Butler 2005), constant-head injection tests (CHIT) (Cardenas and Zlotnik 2003), and direct-push permeameter tests (DPP) (Butler and Dietrich 2004). Although capable of recovering accurate measurements of hydraulic conductivity profiles with depth, they do not allow the concurrent measurement of traditional cone metrics, nor visual profiling with depth, and are typically laborious and time consuming.

The pore pressures generated during uCPT penetration are a function of the hydraulic conductivity of the surrounding medium. Thus, measurements of pore pressures and other uCPT parameters could potentially be the basis of a useful method of determining hydraulic conductivity, on-the-fly, i.e. without the need to suspend advance and to perform a dissipation test (Elsworth 1993). Approximate steady solutions for the pore pressures developed around an advancing penetrometer enable hydraulic conductivity to be determined (Elsworth and Lee 2005), and the limits for which these correlations are appropriate may be defined (Elsworth and Lee 2006). Despite the utility of such correlations between cone metrics and permeability, a lack of uCPT soundings, co-located with independent in-situ measurements of hydraulic conductivity has made it difficult to asses the accuracy and value of such an approach. This study reports unusually well-resolved measurements of hydraulic conductivity gathered from newly developed in-situ permeameters, co-located with uCPT measurements and VisCPT observations. These measurements examine the potential role of sample disturbance, and independently examine the relative accuracy of hydraulic conductivity determinations derived from soil classification (Robertson 1990), from visual VisCPT measurements, and from on-the-fly measurements of pore pressures.

4.2   Field Site

This work was performed at the Geohydrologic Experimental and Monitoring Site (GEMS). This is a research site of the Kansas Geological Survey located in the floodplain of the Kansas River just north of Lawrence, Kansas, in the central portion of the United States (Figure 4.1). GEMS has been the site of extensive research on flow and transport in heterogeneous formations (e.g., Bohling 1999; Butler, McElwee et al. 1999a; Bohling,
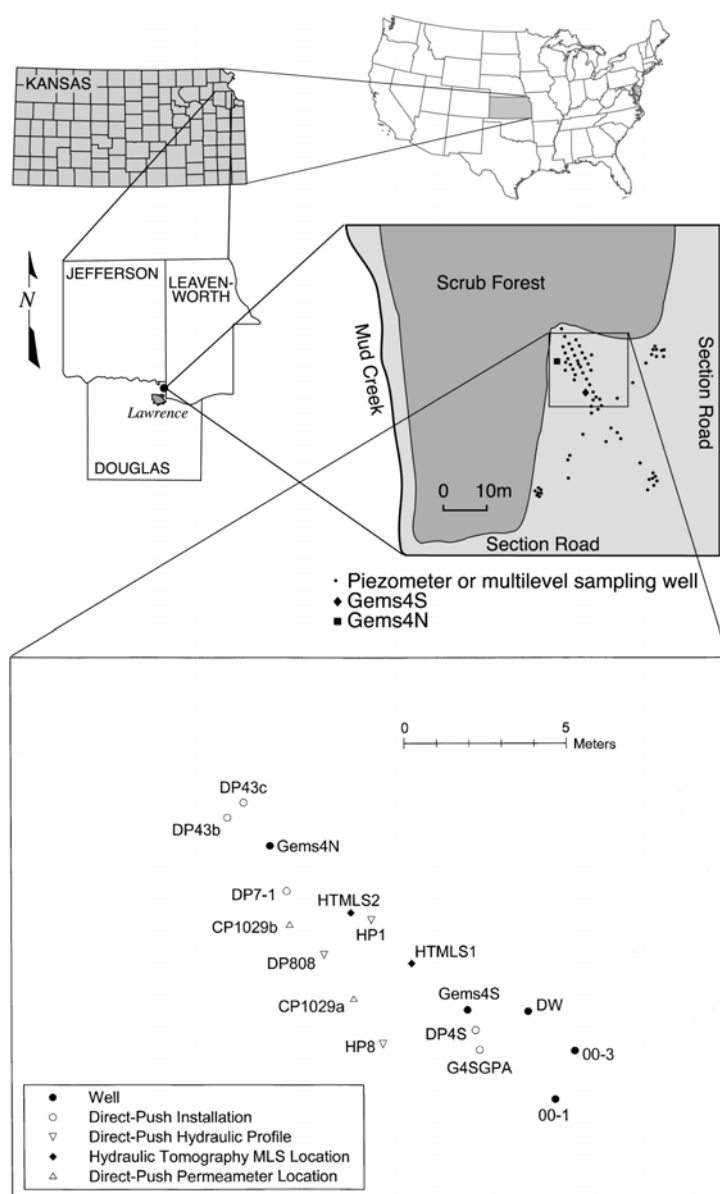
Figure 4.1: Area view of profile locations (Geohydrologic Experimental and Monitoring Site (GEMS), KS)

Zhan et al. 2002; Butler 2002; Butler 2005; McElwee, Butler et al. 1991; Butler, McElwee et al. 1999a; Butler, Healey et al. 1999b; McCall, Butler et al. 2002; Schulmeister, Butler et al. 2003a; Schulmeister, Healey et al. 2003b; Sellwood, Healey et al. 2005). This previous work has enabled the techniques discussed here to be evaluated in a relatively controlled field setting. The shallow subsurface at GEMS consists of $22\,m$ of unconsolidated Holocene sediments of Kansas River alluvium that overlie and are adjacent to materials of Pennsylvanian and late Pleistocene age, respectively. Figure 4.2 displays a cross-sectional view of the shallow subsurface with electrical conductivity logging data obtained from a direct-push probe (Butler, Healey et al. 1999b), and a geologic interpretation from core and logging data. As shown in that figure, the heterogeneous alluvium at GEMS consists of $11.5\,m$ of primarily clay and silt overlying $10.7\,m$ of sand and gravel, which is hydraulically confined by the overlying materials.

The sub area of GEMS used in this work is depicted in the inset of Figure 4.1. This inset displays the locations of conventional wells and of various direct-push probes. The direct-push installations are short screened temporary wells at which slug tests were performed (Butler 2002; Butler, Healey et al. 2002; Butler, Garnett et al. 2003). The DP hydraulic profiles are locations where the hydrostratigraphic profiling method of Sellwood, Healey et al. 2005 was performed. The uCPT, VisCPT, and in-situ permeameter soundings were performed as part of the work reported here.
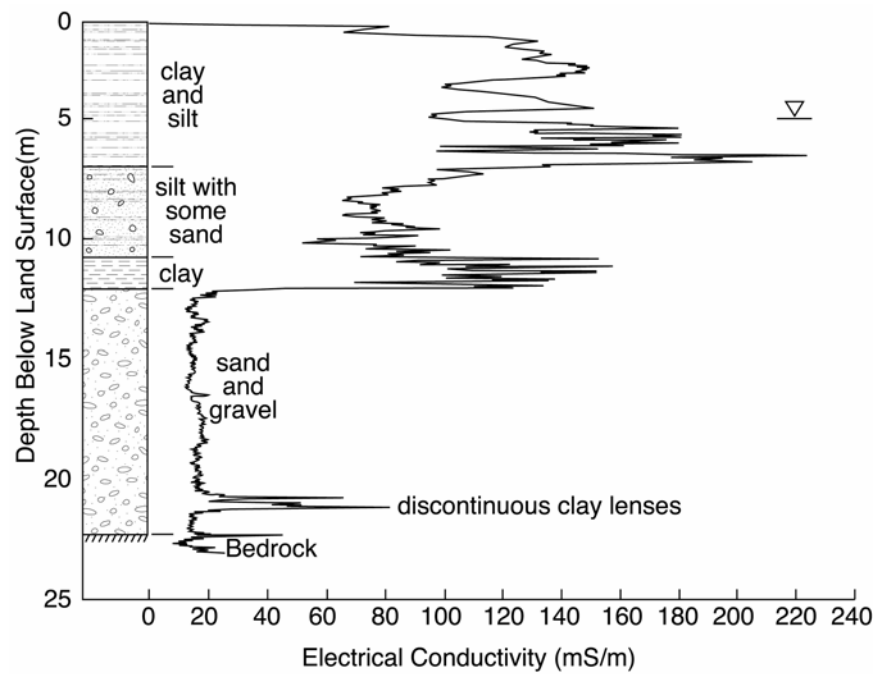
Figure 4.2: Generalized GEMS stratigraphy with electrical conductivity log from G4SGPA (after Butler, Healey et al. 1999b; inverted triangle marks position of water table, head in the sand and gravel interval is approximately one meter lower)

4.3　Methods

Profiles of hydraulic conductivities determined from in-situ permeameters were compared with independently measured magnitudes determined from correlations with grain size distributions, with soil classifications, and from pore pressures determined on-the-fly, as noted in Table 4.1. The six soundings included continuous uCPT (OTF#4), VisCPT (OTF#2), dissipation test (ORF#1), and permeameter test (OTF#2&3) deployments, supplemented by seismic (OTF#4), vibrocone (OTF#5) and dilatometer (OTF#6) tests. The latter three are unused in this analysis. These different methods for evaluating hydraulic conductivities are documented in the following.

4.3.1　In-Situ Permeameter Tests

An in-situ permeameter was fabricated and then deployed to obtain independent evaluations of in-situ hydraulic conductivities along the cone sounding path. To quantify the effects of disturbance in the testing zone, tips of variable diameter ($2a = 3.7\,cm$ and $1.2\,cm$) and taper were developed, as illustrated in Figure 4.3. The sharp cone tip is similar in form to piezoprobes (Ostermeier, Pellerier et al. 2001; Whittle, Sutabutr et al. 2001a; Whittle, Sutabutr et al. 2001b; Dejong, DeGroot et al. 2003), comprising a thin advance probe extending $0.15\,m$ (25 radii) beyond the penetrometer tip, as shown in Figure 4.3 (b). Screens were fabricated with a slot size of $0.3\,mm$, corresponding to a No. 10 screen, at diameters and lengths of $3.7\,cm$ and $1.2\,cm$ for the large tip, and of $4.5\,cm$ and $1.2\,cm$, for the sharp tip. These permeameter tips were deployed in two parallel soundings separated laterally by $0.6\,m$ (OTF #3; $1.2\,cm$ length screen (sharp tip)) and $0.9\,m$ (OTF #2; $4.5\,cm$ length screen) from the uCPT test hole (OTF #4),

Table 4.1 Plan of the in-situ tests and test holes (Geohydrologic Experimental and Monitoring Site, KS)

Test Hole	uCPT	VisCPT	Dissipation Test	Permeameter Test	Seismic Test	Vibrocone Test	Flat Dilatometer Test
OTF #1							
OTF #2				($3.7\,cm$ Screen)			
OTF #3				(Sharp Tip)			
OTF #4							
OTF #5							
OTF #6							
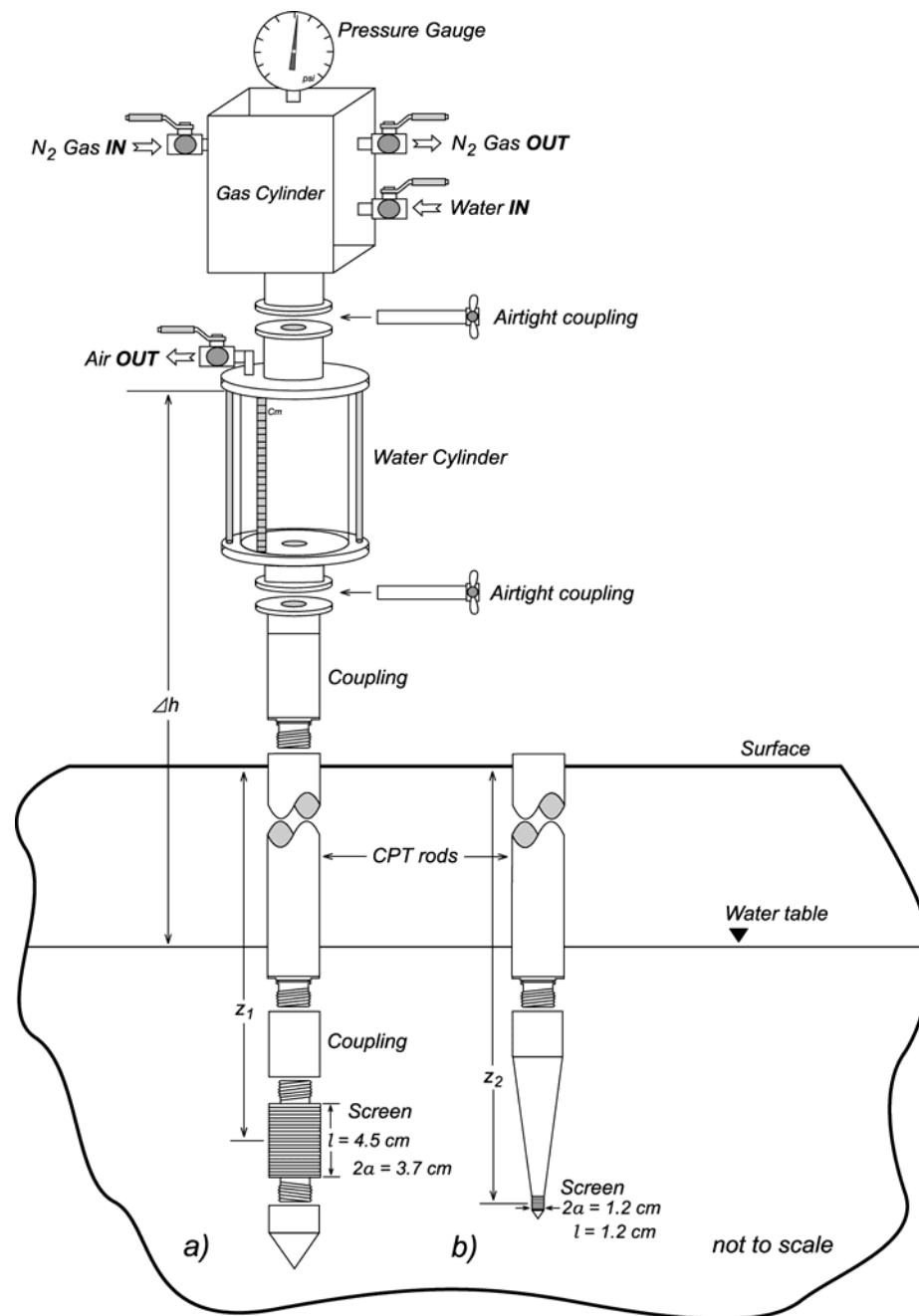
Figure 4.3: In-situ permeameter tests using two different diameter probe tips ((a) $2a = 3.7\,cm$ and (b) $1.2\,cm$), injection fluids through fabricated screens

respectively, as illustrated in Figure 4.1. The in-situ permeameter test involved pressurizing the water column in the above-ground reservoir via compressed nitrogen gas, and measuring the rate of reservoir discharge under constant pressure. Water discharge into the formation was through the perforated screen (Figure 4.3). Flow rate, Q, was measured manually as a volume discharged over a measured time, with the test initiated by rapidly pressurizing the water column. Staged measurements were made in two parallel incremented advances using the fabricated probes. In-situ permeameter tests were completed in the upper $12\,m$ at intervals of $1.0\,m$, and below $12\,m$ at intervals of $0.25\,m$.

Screen clogging was avoided by pressurizing the penetrometer column, and tip, prior to advance. Penetration through the upper $6\ m$ was by pre-advance with a solid-tipped cone, withdrawal, and then secondary advance of the permeameter tip through the remnant hole. To confirm free-flowing conditions at the tip outflow screen, multiple in-situ permeameter tests were performed at each arrest depth using incremented pressures. The linearity between head drop, Δh, and flow rate, Q, was confirmed, with excess heads limited to avoid hydraulic fracturing of the soil.

Hydraulic conductivity magnitudes, K, were recovered from the applied excess head, Δh, and measured volumetric flow rate, Q, through the spherical form of Darcy's Law:

$$K = \frac{Q}{4\pi\Delta h a_s} \tag{4.1}$$

where a_s is an effective radius of the spherical injection zone. This is the radius of a sphere with a specific surface area equal to the flowing area of the cylindrical screen with

an impervious top and bottom. The equivalent radius is

$$a_s = \sqrt{\frac{1}{2}al} \qquad (4.2)$$

where a is radius of the screen, and l is length of the screen. In addition to this characterization, the appropriateness of the equivalent radius was checked against the results of calibration chamber tests. Permeameter tests were conducted in two different geometries ($H \times D = 21cm \times 10cm$ for the sharp tip and $H \times D = 22cm \times 26cm$ for the large $4.5cm$ screen) for known hydraulic conductivities. Calibration chamber measured conductivities were within factors of 1.09 (sharp permeameter) and 1.21 ($4.5cm$ permeameter) of mean measured hydraulic conductivity magnitudes of the soil specimen. Correspondingly, the measured magnitudes of in-situ hydraulic conductivity are used with confidence.

4.3.2   Soil Classifications (Vision Cone Penetration Testing (VisCPT))

uCPT metrics may be used to determine soil characteristics (Douglas and Olsen 1981, Robertson, Campanella et al. 1986) based on grain-size distributions. The metrics of pore pressure ratio, B_q, friction ratio, F_r, and cone resistance, Q_t, may be used to define soil type, and the hydraulic conductivity of the soil may be approximated from its type or related grain size distribution (Robertson 1990), as shown in Table 4.2. As an alternative to the use of traditional cone metrics, the vision cone penetration test (VisCPT) may be used to directly capture a continuous real-time image of the soil. A total of 1500 images are captured per meter of advance (Hryciw, Shin et al. 2003), with this completed along one cone sounding (OTF #1). Through image analysis, the VisCPT is used to define the soil grain size, with hydraulic conductivities computed using the Hazen formula (Hazen

Table 4.2 Hydraulic conductivity predictions from soil classifications (Robertson 1990 and VisCPT).

Depth (m)	Soil classification (Robertson 1990)		Soil Classification (VisCPT)		
	Soil classification	Presumed Hydraulic Conductivity (m/s)	Average number of pixels per (soil particle) diameter (PPD) $(pixels/diameter)$	Diameter of soil particle (D) (mm)	Presumed Hydraulic Conductivity (m/s)
12.7	Sand	10^{-4}	10	0.20	4.8×10^{-4}
13.7	Gravelly sand and sand	10^{-3}	12	0.24	6.9×10^{-4}
14.7	Sand	10^{-4}	15	0.29	1.1×10^{-3}
15.7	Sand	10^{-4}	18	0.35	1.6×10^{-3}
16.7	Sand and silt sand	10^{-4}	28	0.55	3.8×10^{-3}
17.7	Sand	10^{-4}	26	0.51	3.3×10^{-3}
18.7	Sand	10^{-4}	9	0.18	3.9×10^{-4}

1930), based on diameter of the soil particles (Hryciw, Shin et al. 2003) (Table 4.2). The camera for the VisCPT record images at a magnification of 51 pixels/mm. The average number of pixels per (soil particle) diameter (PPD) was used to represent the "relative" size of soil particles within an image. The diameter of the soil particles can then be computed from the magnification (51 pixels/mm) and the number of pixels per diameter (PPD), as shown in Table 4.2, using the following equation (Shin and Hryciw, 2004):

$$D\,(mm\,/\,diameter) = \frac{PPD\,(pixels\,/\,diameter)}{magnification\,level\,(pixels\,/\,mm)} \tag{4.3}$$

These characterizations are later compared with independently measured magnitudes of hydraulic conductivity, recovered from the permeameter tests.

4.3.3   On-the-fly Method

Changes in pore pressure resulting from the advance of the penetrometer may be approximated by a moving volumetric dislocation of finite size migrating within a saturated porous medium (Elsworth 1990; Elsworth and Lee 2005). The steady fluid pressure distribution that develops around the cone is equivalent to the pressure field produced by the continuous injection of fluid into the porous medium surrounding a spherical cavity. This constant injection of fluid volume per unit time is equivalent to the product of penetrometer advance rate per unit time and penetrometer cross-sectional area. For a penetrometer of diameter $2a$ advanced at rate U, the fluid volume injected per unit time (dV) is equal to $\pi a^2 U$. This flux is injected on the spherical shell of the cavity with the condition of no change in fluid pressure in the far field, or $p = p_s$. Solving the spherically symmetric flow problem yields the following relationship (Elsworth and Lee 2005):

$$p - p_s = \frac{\gamma_w}{4\pi K a} dV = \frac{U a \gamma_w}{4K} \tag{4.4}$$

where p_s is the hydrostatic pore fluid pressure, relative to the pressure measured at the penetrometer face, a is the radius of the penetrometer, and U is the penetration rate. Equation (4.4) simply represents the pressure induced by fluid injection across the interior surface of the spherical shell at a rate equivalent to the displacement volume per unit time of the penetrometer.

In a uCPT profile, pore fluid pressure, p, cone resistance, q_t, and sleeve friction, f_s, are measured continuously with depth. By convention, these three quantities are defined in dimensionless form as the pore pressure ratio, B_q, cone resistance, Q_t, and sleeve friction, F_r:

$$B_q = \frac{p - p_s}{q_t - \sigma_{vo}}; \qquad Q_t = \frac{q_t - \sigma_{vo}}{\sigma'_{vo}}; \qquad F_r = \frac{f_s}{q_t - \sigma_{vo}} \tag{4.5}$$

where q_t is the corrected cone resistance, f_s is the sleeve friction defined in units of stress, σ_{vo} is the initial in-situ vertical stress, and the prime denotes effective stress. An expression for hydraulic conductivity in terms of these dimensionless parameters can be obtained by manipulating equation (4.4). The penetration-induced excess pore pressure, $p - p_s$, can be normalized by the initial vertical effective stress (Elsworth and Lee 2005):

$$\frac{p - p_s}{\sigma'_{vo}} = \frac{U a \gamma_w}{4K \sigma'_{vo}} = \frac{1}{K_D} \tag{4.6}$$

where K_D is the dimensionless hydraulic conductivity index ($K_D = (4K\sigma'_{vo})/(U a \gamma_w)$). The ratio $(p - p_s)/\sigma'_{vo}$ can be expressed in terms of the cone metrics of equation (4.5)

as

$$\frac{p-p_s}{\sigma'_{vo}} = \frac{p-p_s}{q_t-\sigma_{vo}}\frac{q_t-\sigma_{vo}}{\sigma'_{vo}} = B_q Q_t = \frac{1}{K_D}. \tag{4.7}$$

This expression relates the pore pressure ratio, B_q and cone resistance, Q_t, to the dimensionless hydraulic conductivity, K_D. Equation (4.7) can be rearranged as

$$K_D = \frac{1}{B_q Q_t}. \tag{4.8}$$

Equation (4.8) can be used to develop cross plots of B_q and Q_t that can be contoured for K_D as shown in Figure 4.4 (a). If B_q and Q_t are known, hydraulic conductivity, K, can be estimated from the K_D values as shown in the figures. Cross plots of these three pairs of metrics, $B_q - Q_t$, $F_r - Q_t$, and $B_q - F_r$, are given in Figure 4.4 for an assumed friction angle of 30^0 (Elsworth, Lee et al. 2005). Importantly, this observationally confirmed relation enables hydraulic conductivity to be recovered during active penetration without arresting penetration and waiting for the pore pressure to dissipate. Appropriate analyses are compared with independently measured hydraulic conductivity estimates from GEMS.

4.4   Observations

Direct-push permeameter tests allow highly reliable measurements of hydraulic conductivity to be recovered for the full vertical profile. These measurements are the most repeatable of the suite of tests considered here, and in this work are considered the control data. Hydraulic conductivities recovered from the in-situ permeameter tests will be compared systematically with those predicted from uCPT on-the-fly, soil classification
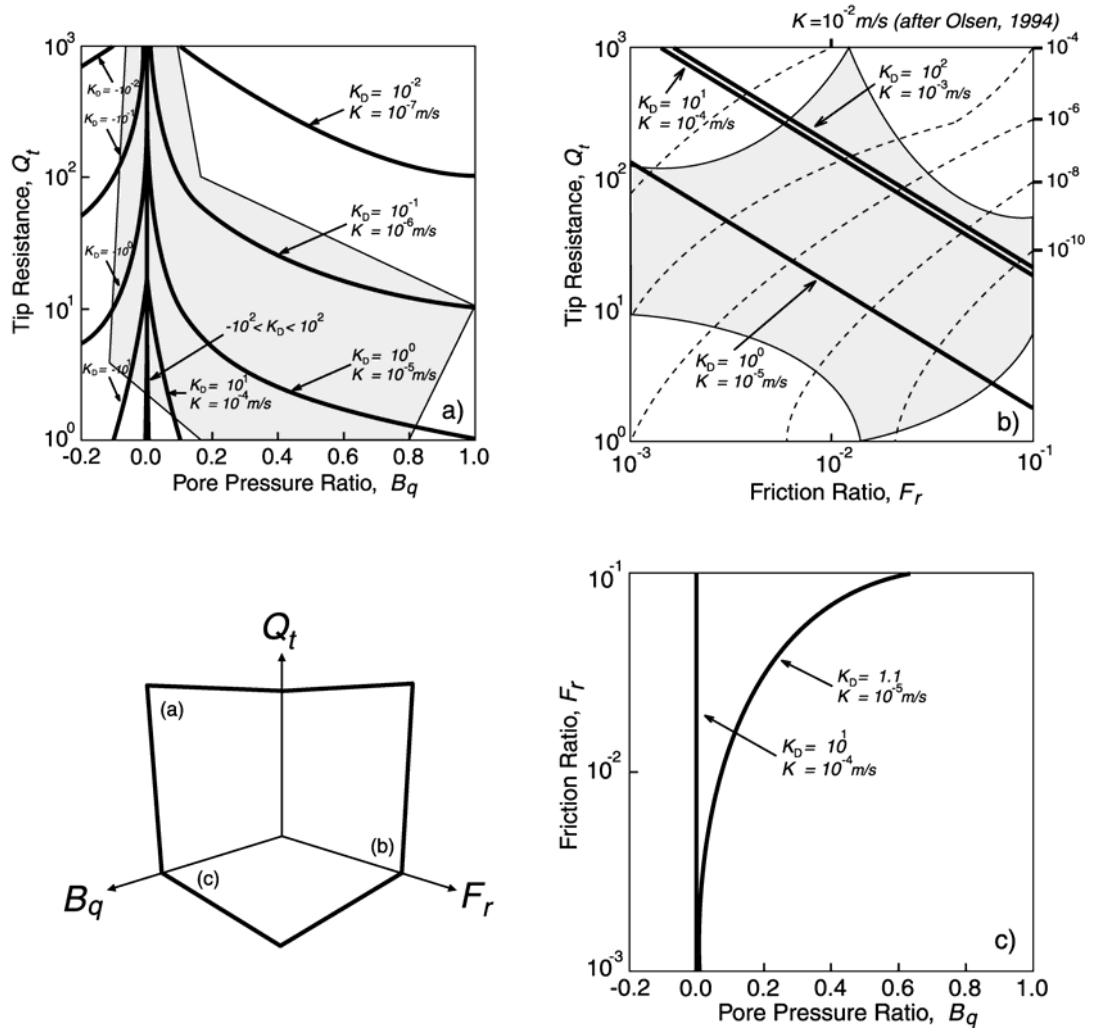
Figure 4.4: Plots of (a) $B_q - Q_t$, (b) $F_r - Q_t$, and (c) $B_q - F_r$ contoured for K_D for the assumption of vertical stresses remain invariant. Values of K are shown for a standard $10\,cm^2$ cone with $\sigma_{vo} = 100\,kPa$, and $U = 2\,cm/s$. The empirical results of Olsen 1994 are shown dashed in (b), and the solid ranges of Robertson (1990) are shown shaded in (a) and (b).

(Robertson 1990) and VisCPT methods.

4.4.1 In-Situ Permeameter Measurements

Measurements of hydraulic conductivities from the deployment of the twin permeameters in parallel soundings are illustrated for the GEMS site in Figure 4.5. Hydraulic conductivity measurements were observed to be in the range 10^{-5} to $10^{-4} \, m/s$, except in the clay and silt layer above $12 \, m$ depth where conductivities are in the range 10^{-9} to $10^{-8} \, m/s$ (Figure 4.5 (a)). Although the profiles are measured with different diameter probes, and therefore with anticipated different degrees of sample disturbance, they show largely similar results. Below the apparent sand and gravel layer at around $\sim 14.5 \, m$, the $4.5 \, cm$ length-screen permeameter-derived measurements of hydraulic conductivity are higher than the sharp permeameter measurements (except above $12 \, m$) (Figure 4.5 (b)). Importantly, these results suggest only a very minor influence of sample disturbance, and hence the feasibility of measuring hydraulic conductivity magnitudes from standard CPT tip configurations. These resulting, and independently measured hydraulic conductivity profiles are used in the following for comparison against alternate methods of determining conductivities.

4.4.2 On-the-fly method

Penetration at the standard rate of 2 cm/s may result in the development of a steady pressure distribution around the cone tip, and this steady magnitude may be used to define the magnitude of the hydraulic conductivity. To be used in this manner, the generated pressures must be both steady state, and partially-drained. They must not be undrained, as this indexes pore pressures to strength, rather than with hydraulic

Figure 4.5: Hydraulic conductivity measurements determined by the in-situ permeameter tests ($4.5\,cm$ screen (squares) and sharp tip (circles)) versus depth at the GEMS, KS

conductivity. These requirements are examined in the following.

4.4.2.1 Steady State

The on-the-fly method of evaluating hydraulic conductivity requires that the pore fluid pressures that develop around the tip be at steady state. In this state, the steady pore pressure results from a balance between the rate of pore fluid generation (controlled by the mean strain-rate imposed by the advancing cone) and the rate of pore pressure dissipation (controlled by the hydraulic conductivity). Two sets of sounding data (OTF #1 and OTF #4) are available to depths of $\sim 19\,m$, and characteristic of different penetrometer-rod change-out characteristics. The first is completed with dissipation tests conducted at each new rod addition, and the second with continuous rod advance, as noted in Figure 4.6. The first profile (OTF #1) is used to measure the hydrostatic pressure distribution, and to determine the location of the position of the water table ($6.0\,m$). The second excess pore pressure profile (OTF #4) is considerably higher than the first profile, indicating that the first profile did not reach steady state. The steady excess pore pressure ($p - p_s$) that develops around the penetrometer tip may be directly linked to the hydraulic conductivity of the surrounding soil. Where pore pressure profile (OTF #1) is excluded, the continuous profiling of penetration-induced pore pressure (OTF #4) during steady penetration is used for estimation of on-the-fly hydraulic conductivity in the following.

4.4.2.2 Undrained Response

The pore fluid pressures generated following standard uCPT sounding in materials ranging from clays to sands (OTF #4) exhibit both undrained and partially-drained
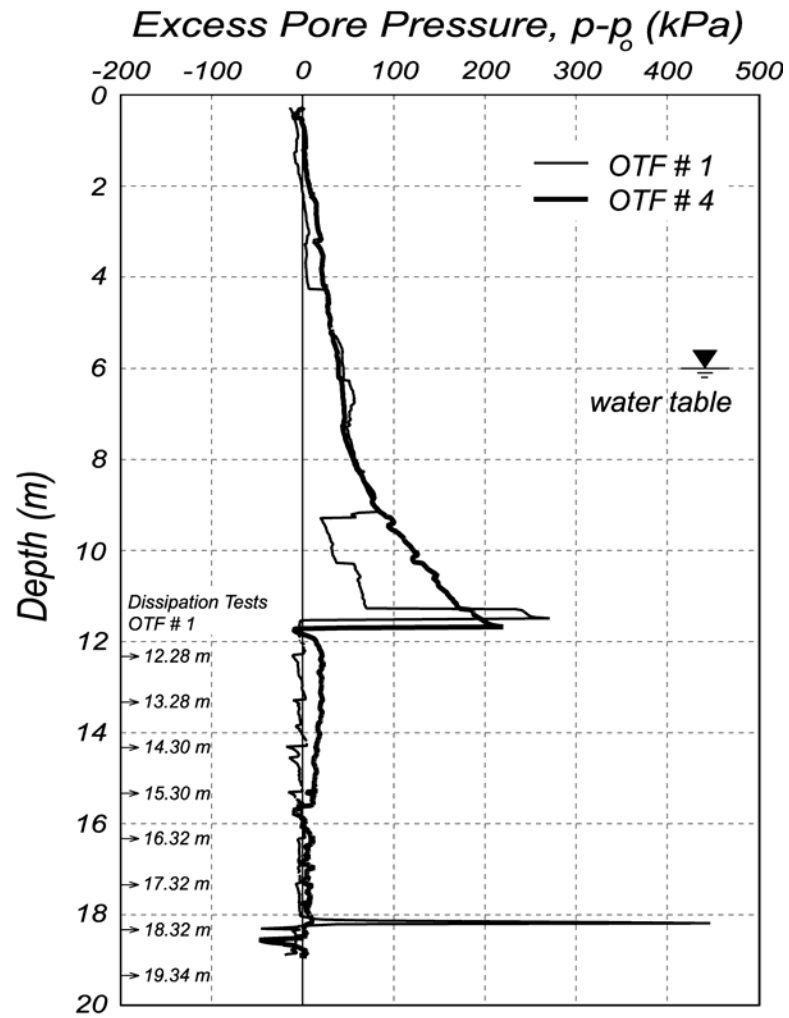
Figure 4.6: The two excess pore pressure profiles: The steady pore pressure were continuously recorded under steady penetration (OFT #4) and the pore pressure, completed with arresting penetration for pore pressure dissipation tests (OFT #1)

response. Since undrained response can only provide information on the tip-local failure conditions, it is important to be able to discriminate this response from the partially-drained behavior that we use to define hydraulic conductivity. The transition from partially-drained to undrained response may be defined in terms of the transition bounds as $B_q Q_t < 1.0 \text{ to } 6.0$, $Q_t F_r < 0.3 \text{ to } 0.7$, and $B_q / F_r < 4.0 \text{ to } 8.0$ (Elsworth, Lee et al. 2005), as illustrated in Figure 4.7. These are represented on the standard plots of cone metrics as (a) $B_q - Q_t$, (b) $F_r - Q_t$, and (c) $B_q - F_r$ in representing the uCPT data (OTF #4) from GEMS in Figure 4.7 (a) through (c). However, these data enable the bounds to be more tightly defined as $B_q Q_t < 0.2$, $F_r Q_t < 2.0$ and $F_r = 0.02$, and $B_q / F_r < 0.8$, respectively for the cone metrics (Figure 4.7). These limits restrict the plausible range for partial drainage and only these partially-drained data can be used to determine hydraulic conductivity magnitudes, on-the-fly. The limiting hydraulic conductivity predictions may be recovered for partially-drained response using the relation $K_D = 1 / B_q Q_t$, on-the-fly, where presumed undrained data, black circles in Figure 4.7, are excluded. Hydraulic conductivity magnitudes may be defined in terms of the cone metric pair that indexes the transition from partially drained to undrained behavior. The hydraulic conductivities recovered from partially-drained behavior are examined in the following.

4.4.2.3 Prediction

Hydraulic conductivity may be recovered during steady uCPT penetration within the defined limits of partial drainage response. An alternative method of validating the on-the-fly method is to compare each magnitudes of hydraulic conductivity measured by the in-situ permeameter tests, using the two fabricated probe tips, with a paired prediction
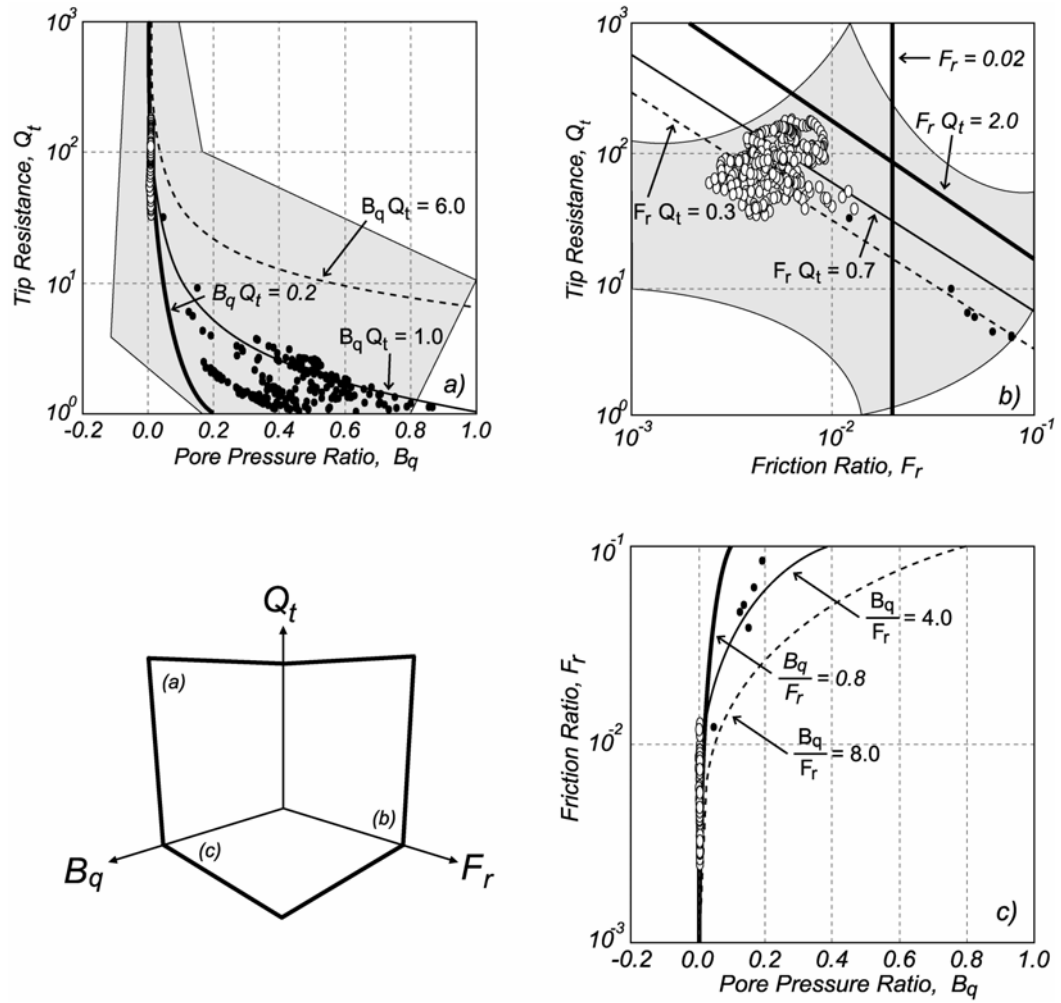
Figure 4.7: Plots of cone metrics (a) $B_q - Q_t$, (b) $Q_t - F_r$, and (c) $B_q - F_r$ with the limits (range of transition given by solid and dashed lines) of undrained penetration identified. Shaded regions in (a) and (b) denote defined ranges of material types (Robertson 1990). Symbols denote data from undrained (black circles) and partially-drained (white circles) response at the GEMS

from $K_D = 1/B_q Q_t$ at an equivalent depth, as illustrated in Figure 4.8 (a) and (b). Hydraulic conductivities systematically recovered from $K_D = 1/B_q Q_t$ are compared with those measured from the permeameter tests. The in-situ permeameter tests measure hydraulic conductivities, and these are converted to $K_D = (4K\sigma'_{vo})/(Ua\gamma_w)$, and are plotted on the horizontal ordinate. The permeameter measurements are assumed to represent the average hydraulic conductivity within an interval centered on the screen length ($l = 4.5\,cm$ and $1.2\,cm$) (Figure 4.3). For purposes of comparison, the arithmetic average of the uCPT estimates is taken over the interval of the permeameter measurements (comprising 32 permeameter measurements). The presumed undrained data (the 4 permeameter measurements) are furthest from the theoretical relation, $K_D = 1/B_q Q_t$. Where undrained data are excluded, there are 28 remaining data points, representing partially drained uCPT estimates in the sand and gravel layers (below a depth $12\,m$) (Elsworth, Lee et al. 2005). The predictions recovered from the relation $K_D = 1/B_q Q_t$ yield consistent evaluations of hydraulic conductivity, as shown in Figure 4.8: (a) and (b). Most of the measurements from the permeameter tests ($4.5\,cm$ screen) which satisfy the requirements of partial-drainage, plot below the relation, $K_D = 1/B_q Q_t$. This represents that the induced pore pressures are smaller than those predicted by this relation, and that this under-generation may result either from dilation around the tip, or from pore pressures being sub-steady state (Figure 4.8 (a)). The data for the sharp-tip permeameter measurements cluster more closely around the on-the-fly relationship, as illustrated in Figure 4.8 (b). All data are within a one order-of-magnitude spread either side of the theoretical relation, $K_D = 1/B_q Q_t$.
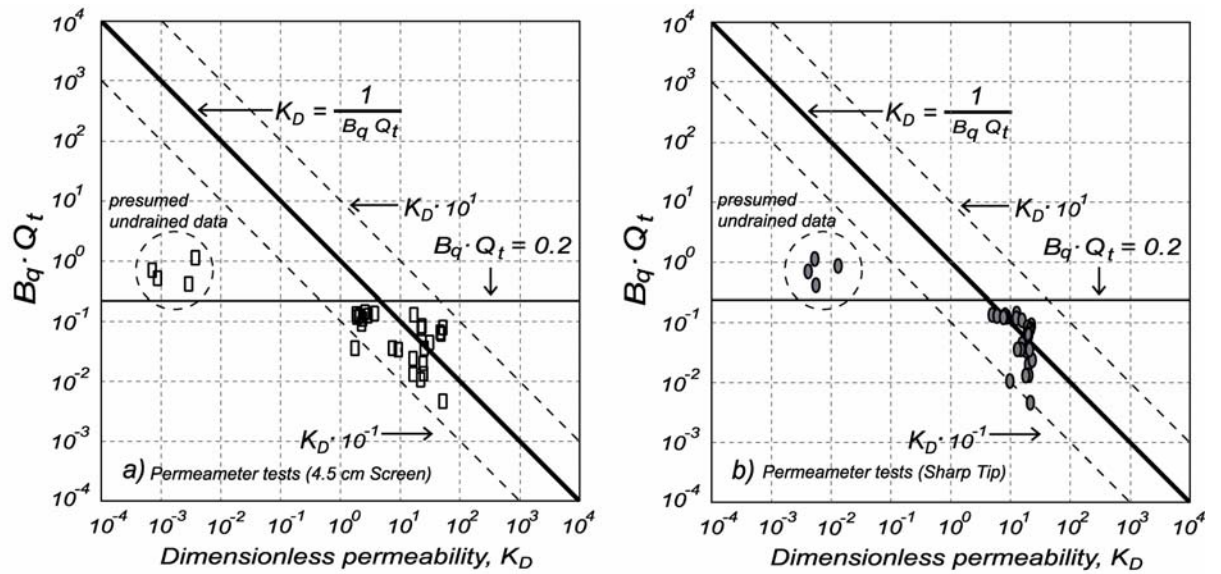
Figure 4.8: a) Selected hydraulic conductivity magnitudes determined from in-situ permeameter test ($3.7\,cm$ screen) adjacent to OTF # 4 (squares), compared with the relation $K_D = 1/B_q Q_t$ b) Selected hydraulic conduvtity magnitudes determined from in-situ permeameter test (sharp tip) adjacent to OTF # 4 (circles), compared with the relation $K_D = 1/B_q Q_t$

4.4.3 Profiles

Another method of determining hydraulic conductivity profiles is in using correlations with soil classification schemes (Robertson 1990) and VisCPT, and in then linking these with quantitative estimates of hydraulic conductivity. Profiles of hydraulic conductivity determined from the large tip and sharp tip permeameters, and from on-the-fly, and soil classification predictions, are shown in Figure 4.9. Negative magnitudes of excess pore pressures result in inadmissible predictions of hydraulic conductivity for estimation using $B_q - Q_t$ and the pore pressure model cannot accommodate negative pore pressures. Magnitudes of hydraulic conductivity, K, predicted directly from $K_D = 1/B_q Q_t$ were compared with the independent permeameter-measured profiles and extended to examine the traditional uCPT classification charts (Robertson 1990) and direct observation from high-quality VisCPT. Estimates of hydraulic conductivity using the ensemble suite of metrics, $B_q - Q_t$ are within two orders of magnitude of the estimates, 10^{-4} to $10^{-5} \, m/s$, especially in the sand and gravel layers below $12 \, m$ depth. The estimates from $B_q - Q_t$ provide higher and scattered estimates especially below $16 \, m$ depth, where measured induced pore pressure magnitudes are small. In this presumed higher hydraulic conductivity zone, induced pore pressures dissipate as quickly as they are developed in the penetration process. uCPT classification charts (Robertson 1990) provide values (filled rectangles) of $10^{-4} \, m/s$ over much of the profile (Figure 4.9). The estimates from $B_q - Q_t$ are uniformly lower than those evaluated from the soil classification method (Robertson 1990) in the upper layers ($12 \, m \sim 16 \, m$ depth), but
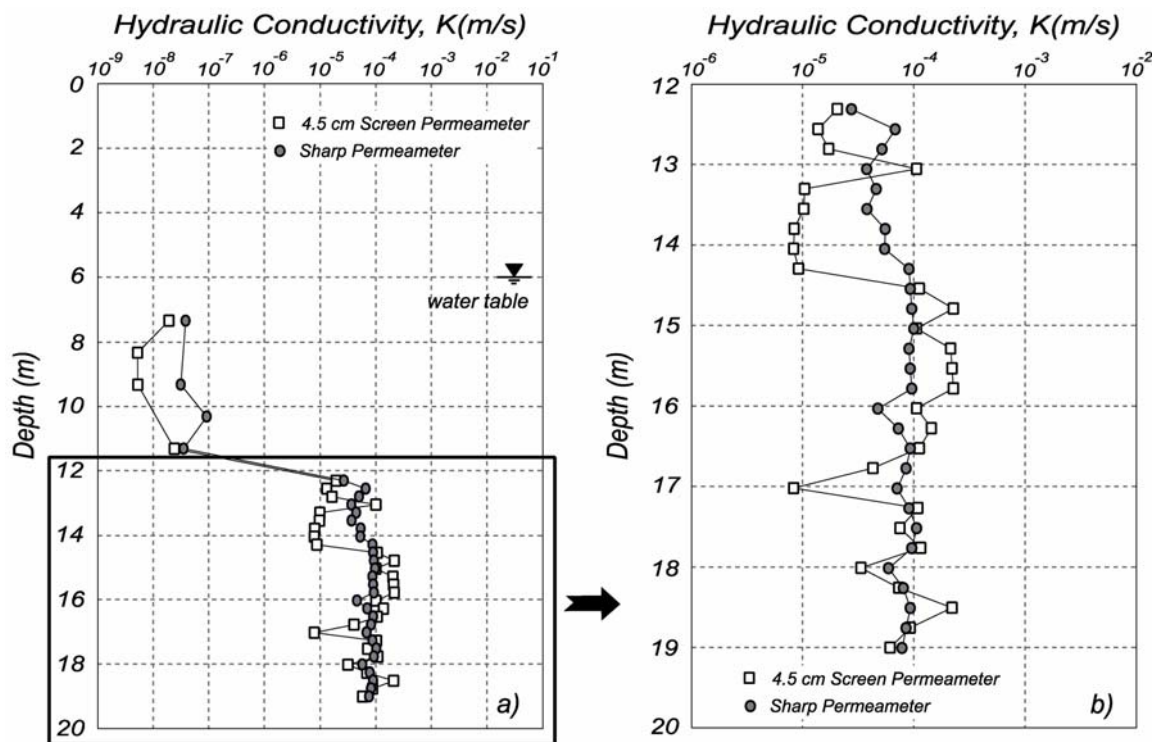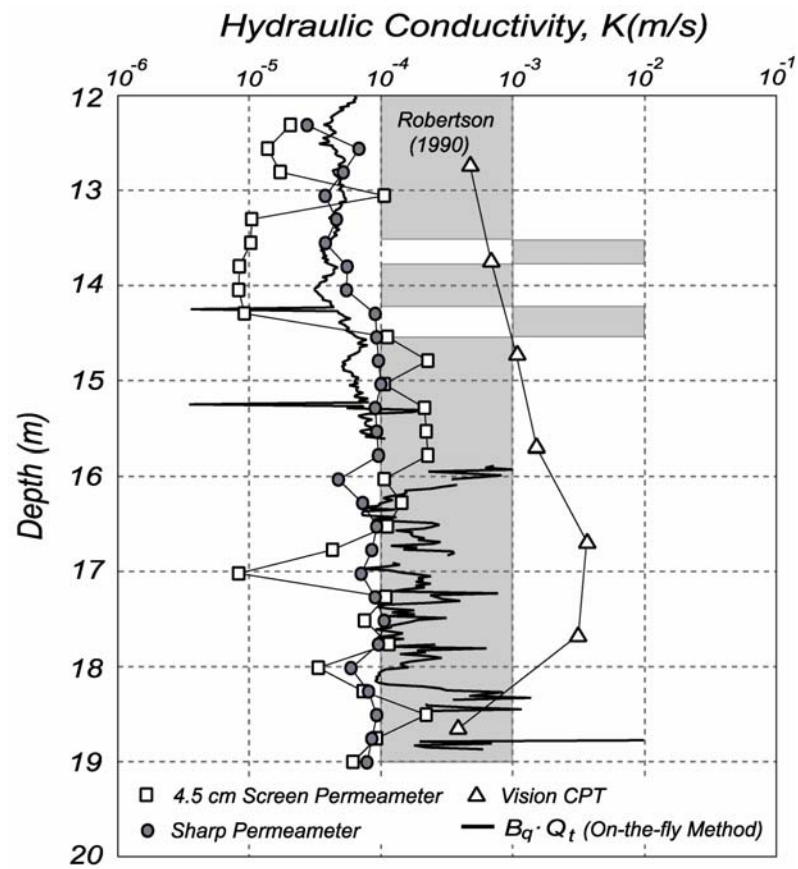
Figure 4.9: Hydraulic conductivity measurements determined by the in-situ permeameter tests ($4.5\,cm$ screen (squares) and sharp tip (circles)) and soil classifications (shade rectangle Robertson 1990 and triangles (VisCPT)) versus depth at the GEMS, KS. Hydraulic conductivity estimates determined from the data pairs $B_q - Q_t$ (solid line) (equation (4.8))

yield close and consistent evaluations of hydraulic conductivity in the lower layer ($16m \sim 19m$ depth). The magnitudes of hydraulic conductivity from VisCPT (triangles in Figure 4.9) are much larger than the other results. The larger differences are likely due to both inaccuracies in the Hazen formula (Hazen 1930) and the visual resolution of finer soil particles in a coarser particle matrix – correspondingly, these estimates may be considered as an upper bound – lager than actual values. The in-situ permeameter test data provide the most reliable measurements of hydraulic conductivity, determined for influences of penetration-induced disturbance using two fabricated probe tips from adjacent uCPT boreholes (OTF #4). The predictions of hydraulic conductivity recovered from magnitudes of $B_q - Q_t$ are higher than those independently measured by permeameter, especially below a depth of $16m$. However, these predictions and measurements from the sharp tip are consistently closer in the zone between $12m$ and $16m$, as illustrated in Figure 4.9. The consistency between estimates recovered from $B_q - Q_t$ and sharp permeameter is taken as reasonable predictions of the hydraulic conductivity. These comparisons indicate that uCPT predictions of hydraulic conductivity from soundings (OTF #4) exhibit close agreement with those measured from in-situ permeameter tests below $12m$. Especially, measurements of hydraulic conductivity from the sharp tip permeameter test are closest to predictions recovered from the pair $B_q - Q_t$, as illustrated in Figure 4.9. The predictions from the larger tip, although not so close as for the sharp tip, exhibit a similar trend. The predictions yielded by the data pair $B_q - Q_t$ provide the most robust evaluation in this comparison, as apparent in Figure 4.9. These show strong correlation between the predicted hydraulic conductivity, K, values and

those measured by the permeameters, as apparent in Figure 4.9.

4.5   Conclusion

Profiles of hydraulic conductivity are measured at the GEMS site through the deployment of direct-push permeameters of two different configurations – one with a standard CPT-like tip, and the second with a thin tapered tip to minimize tip-local disturbance. Measurements of permeability were consistent between the closely correlated suite of measurements using the two tips, suggesting that sample disturbance around a standard cone is not significant. Consequently, permeameter measurements taken through a standard penetrometer tip, or via on-the-fly or dissipation measurements, are expected to be representative of pristine hydraulic conductivity magnitudes.

The extensive suite of in-situ permeameter measurements enabled benchmarking of a variety of methods of evaluating hydraulic conductivity from direct-push methods. These included on-the-fly methods using the uCPT metrics ($B_q - F_r - Q_t$), high-quality observations of soil structure (VisCPT) and correlations with soil classifications derived from uCPT measurements. The feasibility of on-the-fly methods to determine hydraulic conductivity requires that tip-local pore pressures are both steady, and partially drained. The condition of steady behavior is reached where penetration is continuous and uninterrupted. Cone metrics are shown to be capable of distinguishing the threshold between conditions of partial drainage and of undrained behavior. This is apparent where $B_q Q_t < 0.2$, $F_r Q_t < 2.0$ and $F_r = 0.02$, and $B_q / F_r < 0.8$, respectively.

Where undrained data are excluded, the hydraulic conductivity profile may be determined from magnitudes of the induced tip-local pore pressures, where the data represent

remarkably close agreement with the relation $K_D = 1/B_q Q_t$, at the equivalent depth, as illustrated in Figure 4.8 (b) and Figure 4.9. These analyses show that the relation $K_D = 1/B_q Q_t$ exhibits promise as a practical means of accurate prediction of hydraulic conductivity within feasible ranges where the penetration response is both partially-drained and steady. The results indicate the potential to directly recover hydraulic conductivity during active steady penetration and without arresting penetration and waiting for the pore pressure to dissipate.

Acknowledgement

Notation

$a =$ penetrometer radius; L

$dV =$ volume change per unit time in the tip process zone; L^3T^{-1}

$f_s =$ magnitude of sleeve friction; FL^{-2}

$K =$ hydraulic conductivity; LT^{-1}

$p =$ absolute pore fluid pressure (u_2); FL^{-2}

$p_s =$ initial static fluid pressure; FL^{-2}

$p - p_s =$ excess pore pressure; FL^{-2}

$q_c =$ measured cone resistance; FL^{-2}

$q_t =$ corrected cone resistance, $q_c + (1 - a_n)(p - p_s)$; FL^{-2}

$U =$ penetrometer penetration rate; LT^{-1}

$\gamma_w =$ unit weight of water; FL^{-3}

$\sigma_v =$ total vertical stress; FL^{-2}

$\sigma_{vo}, \sigma'_{vo} =$ initial vertical stress and effective stress; FL^{-2}

$B_q =$ dimensionless pore pressure ratio, $(p - p_s)/(q_t - \sigma_{vo})$; $-$

$K_D =$ dimensionless hydraulic conductivity, $(4K\sigma_{vo})/(Ua\gamma_w)$; $-$

$K_D^{B_q - Q_t} =$ dimensionless hydraulic conductivity determined from $B_q - Q_t$ data; $-$

$K_D^{F_r - Q_t} =$ dimensionless hydraulic conductivity determined from $F_r - Q_t$ data; $-$

$K_D^{B_q - F_r} =$ dimensionless hydraulic conductivity determined from $B_q - F_r$ data; $-$

$Q_t =$ normalized cone resistance, $(q_t - \sigma_{vo})/\sigma_{vo}$; $-$, and

F_r = normalized friction factor, $f_s/(q_t - \sigma_{vo})$. –

References

Bohling, G. C. (1999). Evaluation of an induced gradient tracer test. Lawrence, University of Kansas: 224.

Bohling, G. C., X. Zhan, J. J. Butler and L. Zheng (2002). "Steady-shape analysis of tomographic pumping tests for characterization of aquifer heterogeneities." Water Resources Research 38(12): 1324.

Burns, S. E. and P. W. Mayne (1998). " Monotonic and dilatory pressure decay during piezocone tests in clay." Canadian Geotechnical Journal 35(6): 1063-1073.

Butler, J. J. (2002). "A simple correction for slug tests in small-diameter wells." Ground Water 40(3): 303-307.

Butler, J. J. (2005). Hydrogeological methods for estimation of hydraulic conductivity. Hydrogeophysics.

Butler, J. J. and P. Dietrich (2004). New methods for high-resolution characterization of spatial variations in hydraulic conductivity. International Symposium on Hydrogeological Investigation and Remedial Technology, National Central University, Jhongli, Taiwan.

Butler, J. J., E. J. Garnett and J. M. Healey (2003). "Analysis of slug tests in formations of high hydraulic conductivity." Ground Water 41(5): 620-630.

Butler, J. J., J. M. Healey, G. W. McCall, E. J. Garnett and I. S.P. Loheide (2002). "Hydraulic tests with direct-push equipment." Ground Water 40(1): 25-36.

Butler, J. J., J. M. Healey, L. Zheng, G. W. McCall and M. K. Schulmeister (1999b). Hydrostratigraphic characterization of unconsolidated alluvium with direct-push sensor technology, Kansas Geological Survey.

Butler, J. J., D. D. McElwee and G. C. Bohling (1999a). "Pumping tests in networks of multilevel sampling wells: Motivation and methodology." Water Resources Research 35(11): 3553-3560.

Cardenas, M. B. and V. A. Zlotnik (2003). "A simple constant-head injection test for streambed hydraulic conductivity estimation." Ground Water 41(6): 867-871.

Dejong, J. T., D. J. DeGroot, N. J. Yafrate and J. Jakubowski (2003). Detection of soil layering using a miniature piezoprobe. Soil and Rock America 2003, Cambridge, Massachusetts, Verlag Gluckauf Essen.

Douglas, B. J. and R. S. Olsen (1981). Soil classification using electric cone penetrometer. Symposium on cone penetration testing and experience, St. Louis, Geotechnical engineering division, ASCE.

Elsworth, D. (1990). " Theory of partially drained piezometer insertion." Journal of Geotechnical Engineering 116(6): 899-914.

Elsworth, D. (1993). " Analysis of piezocone dissipation data using dislocation methods." Journal of Geotechnical Engineering 119(10): 1601-1623.

Elsworth, D. and D. S. Lee (2005). "Permeability determination from On-the-fly piezocone sounding." Journal of Geotechnical and Geoenvironmental Engineering 131(5): 1-11.

Elsworth, D., D. S. Lee 2005). "Methods and limits of determining permeability from On-the-fly CPT sounding." Geotechnique. In review.

Hazen, A. (1930). Water supply. New York, Wiley.

Hryciw, R. D., A. M. Ghalib and S. A. Raschke (1998). In-situ characterization by VisCPT. Proceedings of the first international conference on site characterization

(ISC'98), Balkema press.

Hryciw, R. D., S. Shin and A. M. Ghalib (2003). High resolution site characterization by VisCPT with application to hydrogeology. Soil and Rock America 2003, Cambridge, Massachusetts, Verlag Gluckauf Essen.

Lunne, T., P. K. Robertson and J. J. M. Powell (1997). Cone Penetration Testing in Geotechnical Practice, Blackie Academic.

McCall, G. W., J. J. Butler, J. M. Healey, A. A. Lanier, S. M. Sellwood and E. J. Garnett (2002). "A dual-tube direct-push method for vertical profiling of hydraulic conductivity in unconsolidated formations." Environmental and Engineering Geoscience 8(2): 75-84.

McElwee, D. D., J. J. Butler and J. M. Healey (1991). "A new sampling system for obtaining relatively undisturbed cores of unconsolidated coarse sand and gravel." Ground Water Monit. Rev 11(3): 182-191.

Mitchell, J. K. and T. L. Brandon (1998). Analysis and use of CPT in earthquake and environmental engineering. Geotechnical Site Characterization, Balkema, Rotterdam.

Olsen, R. S. (1994). Normalization and prediction of geotechnical properties using the cone penetrometer test. Technical Report GL-94-29. Vicksburg, US Army Corps of Engineers, WES: 322.

Ostermeier, R. M., J. H. Pellerier, C. D. Winker and J. W. Nicholson (2001). "Trends in shallow sediment pore pressures - Deepwater Gulf of Mexico." Society of petroleum engineering SPE/IADC 67772.

Parez, L. and R. Fauriel (1988). "The piezocone improvement in the soil investigation."

Rev. Franc. Geotech 44: 13-27.

Raschke, S. A. and R. D. Hryciw (1997). "Vision cone penetrometer (VisCPT) for direct subsurface soil observation." Journal of Geotechnical and Geoenvironmental Engineering 123(11): 1074-1076.

Robertson, P. K. (1990). "Soil classification using the cone penetration test." Canadian Geotechnical Journal 27(1): 151-158.

Robertson, P. K., R. G. Campanella, D. Gillespie and J. Greig (1986). Use of piezometer cone data. Proc. ASCE Spec. Conf. In Situ '86. Use of In Sit Tests in Geotechnical Engineering, Blacksburg, 1263-1280.

Robertson, P. K., J. P. Sully, D. J. Woeller, T. Lunne, J. J. M. Powell and D. G. Gillespie (1992). "Estimating coefficient of consolidation from piezocone tests." Canadian Geotechnical Journal 29(4): 539-550.

Schulmeister, M. K., J. J. Butler, J. M. Healey, L. Zheng, D. A. Wysocki and G. W. McCall (2003a). "Direct-push electrical conductivity logging for high-resolution hydrostratigraphic characterization." Ground Water Monit. and Remed 23(5): 52-62.

Schulmeister, M. K., J. M. Healey, J. J. Butler and G. W. McCall (2003b). "Direct-push geochemical profiling for assessment of inorganic chemical heterogeneity in aquifers." Journal of Contaminant Hydrology 69(3-4): 215-232.

Sellwood, S. M., J. M. Healey, S. R. Birk and J. J. Butler (2005). "Direct-push hydrostratigraphic profiling." Ground Water 43(1): 19-29.

Shin, S. and R. D. Hryciw (2004). "Wavelet analysis of soil mass images for particle size determination." Journal of computing in civil engineering 18(1): 19-27.

Whittle, A. J., T. Sutabutr, J. T. Germaine and A. Varney (2001a). "Prediction and interpretation of pore pressure dissipation for a tapered piezoprobe." Geot chnique 51: 601-617.

Whittle, A. J., T. Sutabutr, J. T. Germaine and A. Varney (2001b). Predition and interpretation of pore pressure dissipation for a tapered piezoprobe. Offshore technology conference, Houston.

Appendix A

Lee, D.S. and Elsworth, D (2004). Indentation of a Free-Falling Sharp Penetrometer into a Poroelastic Seabed - ASCE Journal of Engineering Mechanics Vol 130, No 2. 170 - 179.

Indentation of a Free-Falling Sharp Penetrometer into a Poroelastic Seabed

Dae Sung Lee[1] and Derek Elsworth[2]

Abstract: A solution is developed for the buildup, steady, and postarrest dissipative pore fluid pressure fields that develop around a conical penetrometer that self-embeds from free-fall into the seabed. Arrest from free-fall considers deceleration under undrained conditions in a purely cohesive soil, with constant shear strength with depth. The resulting decelerating velocity field is controlled by soil strength, bearing capacity factors, and inertial components. At low impact velocities the embedment process is controlled by soil strength, and at high velocities by inertia. With the deceleration defined, the solution for a point normal dislocation migrating in a poroelastic medium is extended to incorporate the influence of a tapered tip. Dynamic steady pressures, P_D, develop relative to the penetrating tip geometry with their distribution conditioned by the nondimensional penetration rate, U_D, incorporating impacting penetration rate, consolidation coefficient, and penetrometer radius, and the nondimensional strength, N_D, additionally incorporating undrained shear strength of the sediment. Pore pressures may develop to a steady peak magnitude at the penetrometer tip, and drop as $P_D = 1/x_D$ with distance x_D behind the tip and along the shaft. Induced pore pressures are singular in the zone of tip taper for the assumed zero radius of the penetrometer, negating the direct evaluation of permeability magnitudes from pressures recorded on the cone face. However, peak induced pressure magnitudes may be correlated with sediment permeabilities, postarrest dissipation rates may be correlated with consolidation coefficients, and depths of penetration may be correlated with shear strengths. The magnitudes of fluid pressures evaluated on the shaft may be correlated with sharp penetrometer data (reported by Urgeles et al. in 2000) to independently evaluate magnitudes of strength and transport parameters.

Introduction

Tethered and untethered penetrometers are widely used for the determination of seabed (Richards et al. 1975, for example) and lakebed (Lee 1977; Harvey et al. 1997, for example) characteristics. Of prime interest here is the determination of fluid, mass (chemical), and thermal fluxes on continental margins and in abyssal sediments (Schultheiss and Noel 1986, for example), with ancillary interest in strength parameters that define stability against submarine slope failure (Watts and Masson 1995, for example). Mass, chemical, and thermal fluxes may be evaluated from differential fluid pressures, species concentrations, or temperatures with depth along the embedded lance axis; these data must be combined with Darcy's, Fick's, or Fourier's laws, respectively. Implicit in the evaluation is that permeability of the sediments may be independently defined to enable fluid mass flux to be accurately determined, with potential coupling to advective components of chemical or thermal fluxes.

Current methods of determining the permeability of the penetrated sediments involve first evaluating hydraulic diffusivity from the dissipation rate of the penetration-induced pore fluid pressures (Torstensson 1977; Robertson et al. 1986; Levadoux and Baligh 1986; Baligh and Levadoux 1986; Robertson et al. 1992). This requires that the strain field around the penetrometer be defined by analytical (Ladanyi 1963; Vesic 1972; Baligh and Scott 1976; Drescher and Kang 1987) or numerical (Baligh 1985; Tumay et al. 1985; Acar and Tumay 1986) methods, and pore pressures estimated by coupling with an appropriate constitutive model (Skempton 1954; Biot and Willis 1957). Permeability is subsequently determined from hydraulic diffusivity through knowledge of the drained deformation modulus, E, or reciprocally analogous coefficient of volume compressibility, m_v, or "frame" compressibility (Levadoux and Baligh 1986; Robertson et al. 1992). The drained modulus is determined either from laboratory testing of recovered sediment samples, or in some cases from the reduction of tidally induced pore fluid pressures (Davis et al. 1991; Fang et al. 1993; Wang and Davis 1996). Of these two methods, the latter is most desirable, since in situ response is recorded for a relatively large representative sediment volume. However, depending on fixed tidal frequency and the relative moduli and permeabilities of the sediment, phase offsets and pressure amplitude profiles with depth may be difficult to resolve for the determination of permeabilities (Wang and Davis 1996). This is especially true where permeabilities are relatively high, and the phase offset is essentially absent. Alternatively, the use of maximum pore pressure magnitudes developed during penetrometer insertion provides a one-step method to determine permeability magnitudes (Elsworth 1993, 1998). This procedure offers the po-

[1]Dept. of Energy and Geo-Environmental Engineering, Pennsylvania State Univ., University Park, PA 16802-5000.

[2]Dept. of Energy and Geo-Environmental Engineering, Pennsylvania State Univ., University Park, PA 16802-5000.
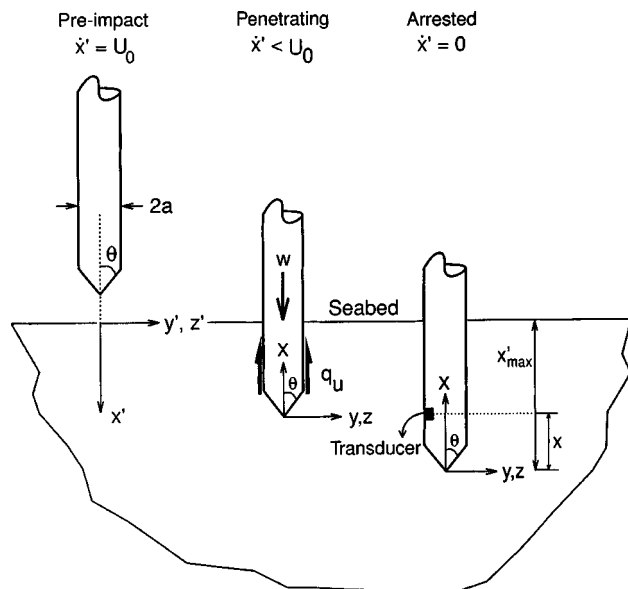
Fig. 1. Schematic of a lance falling at terminal velocity, U_0, and impacting the seabed. For embedment, the coordinate system is fixed to the seafloor as the lance self-embeds under undrained conditions. For the evolving partially drained analysis of embedment-generated pore pressures, the coordinate system is fixed to the penetrometer tip.

tential to provide independent corroboration of permeabilities where they are determined by other means, and permeability magnitudes where they are otherwise unavailable.

Many of the difficulties involved in determining permeability using current techniques may be resolved if the magnitude of penetration-induced pore pressure is used as an index to define permeability. From this approach, permeability magnitudes are available directly from the combined early time pressure data, and lance deceleration response. Hydraulic diffusivities, c, are available from the dissipation response, enabling frame compressibility, and potentially undrained sediment strength, to be recovered, without recourse to additional laboratory testing. The utility of this approach is examined in the following.

The following analysis addresses this complex problem by, for the first time, evaluating penetration induced pore pressures around a decelerating tapered probe. This is evaluated in two steps; first the rate of deceleration of the lance as it impacts the soft seabed is determined, and then used to evaluate the resulting pore pressure distributions that develop around the embedding tip and shaft.
This analysis may be extended to include the local geometry of the penetrometer tip by using a distribution of volumetric dislocations that closely approximate the geometry of tip advance. This is completed in the following.

Embedment Deceleration

Consider a sharp lance falling through the water column that has reached terminal velocity, U_0, and subsequently impacts the soft sediments of the seabed, as illustrated in Fig. 1. These soft sediments are assumed cohesive only, and in the time frame of deceleration of the lance, behave as undrained, for the purposes of this first evaluation. The undrained cohesive strength, S_u, is constant with depth, and the lance is sufficiently long that the tip-region is short in comparison with the overall length of the penetrometer.

Where strength is linearly varying, an average strength magnitude representative of the depth profile may be substituted. As the lance tip, assumed sharp in this analysis, embeds within the soil to a distance x' below the seabed surface, the force resisting embedment builds. The bearing capacity, q_u, of the lance may be defined in terms of the end-bearing area, A_p, and shaft area, A_s, as

$$q_u = A_p(S_u N_c + \sigma_{vo}) + A_s S_u \tag{1}$$

where σ_{vo} = total stress, absent the sea pressure, at current tip embedment-depth, x'; and N_c = nondimensional bearing capacity factor, typically approaching 9 for depth to diameter ratios greater than 4.5 (Skempton 1959). The rightmost two terms of stress and shaft friction vary linearly with embedment depth, x', and Eq. (1) may be redefined as

$$q_u = A_p S_u N_c + (A_p \gamma_s + 2\pi a S_u) x' \tag{2}$$

where the probe diameter is $2a$, and γ_s = drained unit weight of the soil. The penetrometer is assumed blunt in order to render the analysis of undrained penetration tractable. Alternatively, the bearing force, acting in the direction of negative x', may be defined as a linear function of depth as

$$q_u = N_c' + N_q' x' \tag{3}$$

This enables a force balance to be completed on the free-falling penetrometer as it embeds in the seabed, and the end-bearing force builds approximately linearly with embedment. Balancing the vertically downward absolute mass, w, and buoyant mass, w_b, of the penetrometer with the vertically upward resistance, q_u, of the combined end- and shaft-resistance, yields, when balanced with inertial force

$$w\ddot{x}'[t] = w_b g - N_c' - N_q' x'[t] \tag{4}$$

The double overdot represents acceleration. The lance is rigid, and translates with the motion of the tip, indexed in this relation as x'. The initial conditions are set at time $t = 0$ when the lance-tip first impacts the seabed at velocity, U_0, as

$$x'[t=0] = 0$$
$$\dot{x}'[t=0] = U_0 \tag{5}$$

Solving the differential equation (4) for the boundary conditions of Eq. (5) enables the progress of embedment with time to be defined as

$$x'[t] = \frac{(g w_b - N_c')}{N_q'}\left[1 - \cos\left(\sqrt{\frac{N_q'}{w}}t\right)\right] + U_0\sqrt{\frac{w}{N_q'}}\sin\left(\sqrt{\frac{N_q'}{w}}t\right) \tag{6}$$

and for the change in velocity, $\dot{x}'[t]$, with time as

$$\dot{x}'[t] = \frac{(g w_b - N_c')}{N_q'}\sqrt{\frac{N_q'}{w}}\sin\left(\sqrt{\frac{N_q'}{w}}t\right) + U_0\cos\left(\sqrt{\frac{N_q'}{w}}t\right) \tag{7}$$

In the solutions for both embedment length and velocity, the two terms represent, respectively, noninertial penetration under self-weight (first term), and the inertial component of the lance (second term). Solving for the time until arrest is possible by setting Eq. (7) to zero as $\dot{x}'[t] = 0$ when deceleration is complete. This yields

$$t|_{\dot{x}'=0} = \sqrt{\frac{w}{N_q'}}\arctan\left(-\frac{U_0 N_q'}{(g w_b - N_c')}\sqrt{\frac{w}{N_q'}}\right) \tag{8}$$

for the time to arrest, or alternatively the embedment length x'_{max}, as

$$x'_{max} = \left(\frac{gw_b - N'_c}{N'_q}\right) + \left[\left(\frac{gw_b - N'_c}{N'_q}\right)^2 \cdot \frac{N'_q}{w} \frac{1}{U_0} + U_0 \sqrt{\frac{w}{N'_q}}\right]$$

$$\times \sin\left(\sqrt{\frac{N'_q}{w}} t \Big|_{\dot{x}'=0}\right) \tag{9}$$

This complex relation may be simplified by realizing there are two regimes of penetration; that where inertial effects are negligible, for small U_0, and alternatively where inertial effects dominate. From Eq. (7), at slow penetration velocities, as $U_0 \rightarrow 0$ then

$$U_0 \ll \frac{(gw_b - N'_c)}{N'_q} \sqrt{\frac{N'_q}{w}} \tag{10}$$

and $t\sqrt{N'_q/w} = 0$. Substituting this into Eq. (6) yields a trivial solution of zero embedment as $x'|_{max} = 0$. This condition is met when $N'_c \gg N'_q$, and surface bearing capacity greatly exceeds the influence of bearing at depth. The corollary to the noninertial condition is where the impact velocity is comparatively large. For this condition

$$U_0 \gg \frac{(gw_b - N'_c)}{N'_q} \sqrt{\frac{N'_q}{w}} \quad \text{then from Eq. (7)} \quad \sqrt{\frac{N'_q}{w}} t = \frac{\pi}{2} \tag{11}$$

Substituting Eq. (11) into Eq. (6) results in a maximum embedment depth, $x'|_{max}$, of

$$x'|_{max} = U_0 \sqrt{\frac{w}{N'_q}} \tag{12}$$

occurring at time

$$t = \frac{\pi}{2} \sqrt{\frac{w}{N'_q}} \tag{13}$$

The consequence of Eq. (12) is that shear strength, S_u, may be determined from either knowledge of the impact velocity and embedment length, or from knowledge of the time to decelerate to zero velocity. Each reduction method enables N'_q to be determined, and hence S_u, if lance geometry and weight are known. An alternative to using a point measurement of time-to-arrest or embedment-length is to fit the recorded velocity history to the rearranged Eq. (7) as

$$N'_q = \left[\arccos\left(\frac{\dot{x}'[t]}{U_0}\right) \frac{\sqrt{w}}{t}\right]^2 \tag{14}$$

This enables N'_q and hence S_u to be recovered from the deceleration history. Where the impact velocity, U_0, is significant, as $U_0 \gg (gw_b - N'_c)/n'_q \sqrt{N'_q/w}$, then the embedment history simplifies to

$$\dot{x}'[t] = U_0 \cos\left(\sqrt{\frac{N'_q}{w}} t\right) = U \tag{15}$$

for velocity, and

$$x'[t] = U_0 \sqrt{\frac{w}{N'_q}} \sin\left(\sqrt{\frac{N'_q}{w}} t\right) \tag{16}$$

for embedment depth. These relations may be used to evaluate the development of pore fluid pressures that result from penetration, where the requirement for undrained penetration is relaxed. Pore

pressures generated around the decelerating probe may be determined from the approximate probe velocity as the unit decelerates.

Dislocation Analysis

The behavior of a sharp penetrometer, moving within a poroelastic medium, may be represented by a moving volumetric dislocation. The incremental form of this is a point volumetric dislocation, of volume dV (L^3), representing the dilation in unit time, t, subjected to a volumetric dilation rate, v $(L^3 T^{-1})$, as $dV = v\,dt$. For $t \geq 0$ a volumetric dislocation is introduced at the origin ($x = y = z = 0$) with the poroelastic medium moving at velocity $+U$ in the x-direction of the fixed Cartesian coordinate system, representing a dislocation migrating within an infinite medium, as illustrated in Fig. 1. The velocity of migration is $U = U_0 \cos(bt)$, and the location at time, t, is $x'[t] = (U_0/b)\sin(bt)$, where $b = \sqrt{N'_q/w}$ as identified in Eqs. (2), (3), and (4). The position of a point located at (x,y,z) at time t would have been $(\{x - (U_0/b)\sin[b(t-\tau)]\}, y, z)$ at time τ. This migrating coordinate system enables the behavior to be defined for a static dislocation (Cleary 1977; Elsworth 1991)

$$p - p_s = \frac{c\,dV}{4\pi \tilde{R}^3} \frac{\mu}{k} \frac{\tilde{\xi}^3}{2\sqrt{\pi}} e^{-\tilde{\xi}^2/4} \tag{17}$$

with $\tilde{\xi} = \tilde{R}/\sqrt{c(t-\tau)}$ and $\tilde{R}^2 = \{x - (U_0/b)\sin[b(t-\tau)]\}^2 + y^2 + z^2$. The material properties defining the medium represent absolute pore fluid pressure, p, relative to the initial static fluid pressure, p_s, permeability, k, hydraulic diffusivity, c, and dynamic viscosity of the fluid, μ. Although derived for an orthogonal triplicate of force dipoles, representing the volumetric dilation of a cube in a poroelastic medium (Cleary 1977), the undefined volume dilation may be indexed to the compressibility of the surrounding medium (Elsworth 1991; 1992). Physically, a migrating dislocation represents a volume of fluid equivalent to the volume of the soil and water mixture displaced by the injection of the penetrometer. It is feasible to represent the pressures induced by the instantaneous injection of a volume of fluid, dV. Substituting into Eq. (17) for the incremental rate of dilation as $dV = v\,d\tau$, and integrating in time yields

$$p - p_s = \int_0^t \frac{cv}{4\pi \tilde{R}^3} \frac{\mu}{k} \frac{\tilde{\xi}^3}{2\sqrt{\pi}} e^{-\tilde{\xi}^2/4} d\tau \tag{18}$$

where v is the rate of volume change $(L^3 T^{-1})$.

This is similar to the standard result reported (Elsworth 1991) for a penetrometer moving at constant velocity, v. To determine the form of the fluid pressure field that develops around a decelerating penetrometer, tapered along its axis, the response for a point volumetric dislocation must be distributed to represent the moving feature. Consider the conical tip of a penetrometer of radius, a, as illustrated in Fig. 2, where the semiapical angle, θ, and length of taper, l, define the geometry. A surrogate variable χ is selected that parallels the x axis that may be used for integrating an appropriately weighted distribution of the point dislocations. Correspondingly, the projected area, dA, of a circumferential contour on the y-, z-plane is defined

$$dA = 2\pi r'\,dr' \begin{cases} r' = \chi \tan\theta \\ dr' = d\chi \tan\theta \end{cases} \tag{19}$$

which upon substitution of the components of Eq. (19) gives

$$dA = 2\pi \tan^2\theta \, \chi \, d\chi \tag{20}$$
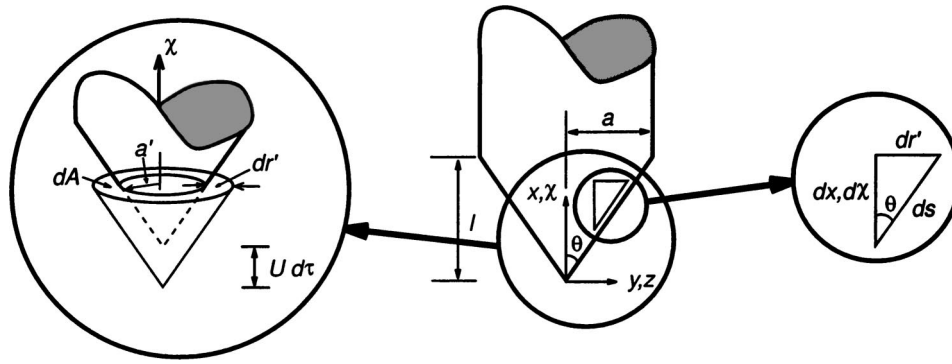
Fig. 2. Geometry of cone tip (center) definining length of taper, l, semiapical angle, θ, and shaft radius, a. Coordinate system is attached to the cone apex and migrates with the penetrometer at velocity, U, in the direction of the negative x or χ axis. Incremental advance of length $U d\tau$ in time $d\tau$ results in expansion of a cavity (left), defined in magnitude by Eq. (19).

For an incremental advance of the penetrometer of $U d\tau$ in time $d\tau$, the distribution of volume is $dV = dA \, U d\tau$, and substituting the relation of Eq. (20), and noting from the previous that $dV = v d\tau$, then

$$v = 2\pi \tan^2 \theta \chi U d\chi = 2\pi \tan^2 \theta \chi U_0 \cos[b(t-\tau)]d\chi \quad (21)$$

This may be substituted directly into Eq. (18) to yield

$$p - p_s = \frac{\mu}{k} \frac{\tan^2 \theta U_0 c}{4\sqrt{\pi}} \int_0^l \int_0^t \chi \frac{\widetilde{\xi}^3}{\widetilde{R}^3} e^{-\widetilde{\xi}^2/4} \cos[b(t-\tau)]d\tau d\chi \quad (22)$$

where the tilde overbar denotes inclusion of the variable coordinate of integration as $\widetilde{x} = x - (U_0/b)\sin[b(t-\tau)] - \chi$ and

$$\widetilde{R} = \sqrt{\widetilde{x}^2 + y^2 + z^2} \quad \text{and} \quad \widetilde{\xi} = \frac{\widetilde{R}}{\sqrt{c(t-\tau)}} \quad (23)$$

representing migrating coordinates and a reciprocal nondimensional time.

Static models are typically restricted to the undrained distributions of pore pressure and their subsequent dissipation, but are also incapable of partial drainage concurrent with penetration. Conversely, the models presented here represent a traveling cavity, not only static conditions. Importantly, it is feasible to represent the dynamic steady pore pressure distribution that evolves around the cone tip (Elsworth 1993), and to readily accommodate partially drained behavior.

The penetrometer decelerates as it enters the half space, although the pore pressure solution is for motion within an infinite medium. This apparent contradiction significantly simplifies the ensuing solution, with little expected loss of applicability or accuracy. Induced pressures, proportional to the tip radius, a, are insignificant beyond 10 radii from the shaft (Levadoux and Baligh 1986; Elsworth 1991) and therefore the influence of the free surface is not felt once insertion has reached beyond this. For the 40 mm diameter probe tip, the 10 radii threshold is passed once the 3 m probe has embedded to 8% of its length. Correspondingly, this simplification will have little adverse effect on the solution.

Nondimensional Parameters

The behavior of the system may be defined in terms of the nondimensional parameters of excess fluid pressure, P_D, penetration rate, U_D, strength, N_D, and time, t_D, as

$$P_D = \frac{4(p - p_s)}{U_0 a} \frac{k}{\mu} \quad (24)$$

$$U_D = \frac{U_0 a}{2c} \quad (25)$$

$$N_D = \frac{ba^2}{2c} \quad (26)$$

$$t_D = \frac{4ct}{a^2} \quad (27)$$

$$(x_D; y_D; z_D) = \frac{1}{a}(x; y; z) \quad (28)$$

with $\widetilde{R}_D = \sqrt{\widetilde{x}_D^2 + y_D^2 + z_D^2}$, $\widetilde{x}_D = \widetilde{x}/a$ or $\widetilde{x}_D = x_D - (U_D/N_D)\sin[1/2N_D(t_D - \tau_D)] - \chi_D$. These parameters give, respectively, nondimensional pressures, impact velocities, strength, time, and locations.

These nondimensional parameters may be substituted into Eq. (22) to give, in the final form, the behavior around a tapered penetrometer with tip length, $l_D = l/a$ as

$$P_D = \frac{2\tan^2 \theta}{\sqrt{\pi}} \int_0^{l_D} \int_0^{t_D} \chi_D \frac{e^{-\widetilde{R}_D^2/(t_D - \tau_D)}}{(t_D - \tau_D)^{3/2}}$$

$$\times \cos\left[\frac{1}{2}N_D(t_D - \tau_D)\right]d\tau_D d\chi_D \quad (29)$$

This enables magnitudes of pore pressure buildup to be determined following initiation of penetration within an infinite medium. Application to this is described in the following.

Parametric Behavior

Postinitiation Pressure Buildup

The nondimensional pressure, P_D, defined in Eq. (29), may be used to define the buildup of pressure following the impact of the penetrometer with the surface of the seabed. The penetrometer impacts the seabed at velocity U_0, represented in dimensionless magnitude as U_D, and decelerates to arrest. Both the length of embedment at arrest and the time to arrest may be evaluated from Eq. (12). The instant of impact is taken as time $t = 0$, when the velocity is U_0, enabling the time to arrest to be defined in non-
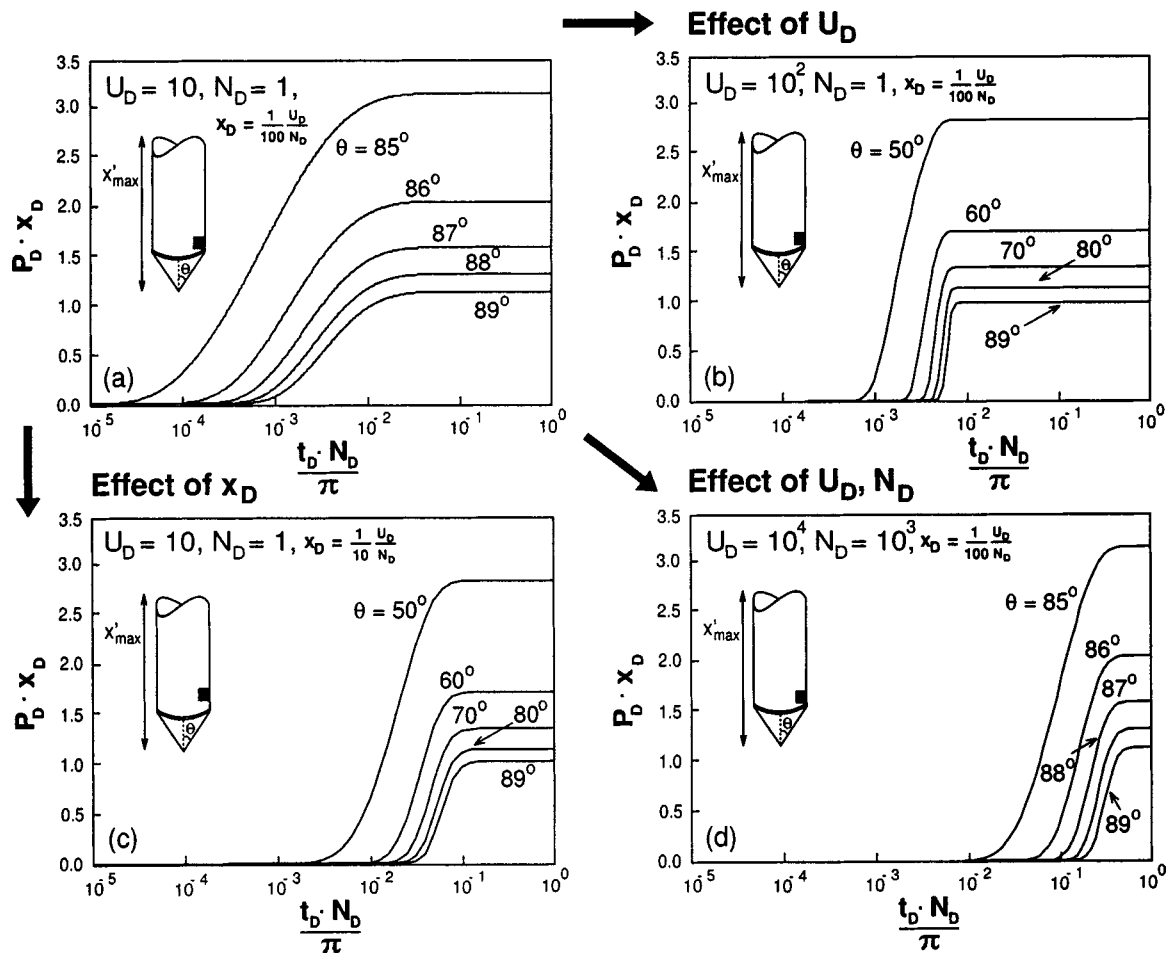
Fig. 3. Buildup of nondimensional pressure, $P_D x_D$, with time, $t_D N_D / \pi$, for a selected pressure monitoring location on the penetrometer shaft, at ordinate (a), (b), and (d) $x_D = (1/100)(U_D/N_D)$, (c) $x_D = (1/10)(U_D/N_D)$, behind the penetrometer tip. This represents a proportional length of 1/100 and 1/10 of the final embedment length behind the penetrometer tip. Pressure response is for various taper angles for the cone, θ, impact velocities, U_D, and material strengths, N_D.

dimensional terms as $t'_D = \pi / N_D$. At this time, the embedment depth is a maximum, with the seabed present to a height of $x'_{D_{max}} = U_D / N_D$ along the shaft.

Pressure buildup response may be evaluated over the period from impact to arrest, for $0 < t_D < t'_D$, and for a variety of taper angles for the cone, θ, impact velocities, and material strengths. Impact velocity is represented by U_D, tip length by l_D, and material strength by N_D. For soft seabed clays with undrained strength, S_u, of the order of 10–50 kN/m^2, magnitudes of N_D are in the range 1–1000. It is convenient to compare the buildup of pore pressures with respect to a given location of the transducer at x_D. To make comparisons feasible, we choose the transducer to be above the conical shoulder of the tip, and hence at a location, x_D, greater than the taper lengths, l_D, with respect to the embedment depth, U_D / N_D. This is dependent only on the choice of taper angle for the cone, θ, as $\tan \theta = 1/l_D$. Correspondingly, Fig. 3 represents the pressure buildup for the transducer placed one-hundredth $[x_D = (1/100)(U_D/N_D)]$ and one-tenth $[x_D = (1/10)(U_D/N_D)]$ of the distance back from the penetrometer tip, where x is the location of the pressure transducer behind the penetrometer tip. Axes of the figure are selected that take advantage of the known behavior of pressure buildup. Nondimensional pressures are plotted as the product $P_D x_D$, since it is known that the peak pressures shown in this format asymptote to unity as

$P_D x_D \rightarrow 1$. Time is reported as $t_D N_D / \pi$, since we know that arrest occurs at $t'_D = \pi / N_D$, hence arrest occurs at $t_D N_D / \pi = 1$.

For a sharp penetrometer, the influence of tip taper is prescribed for various taper angles, penetration rates, monitoring locations, and material strengths on the penetrometer shaft. In Fig. 3(a), for monitoring location $x_D = (1/100)(U_D/N_D)$, diffusive response is merely shifted by a one order-of-magnitude increase in taper angles for the cone. Apparent from Fig. 3(a) is that at larger taper angles ($\theta \rightarrow 90°$), the pressure response is close to that of a blunt penetrometer behavior (Elsworth and Lee, unpublished, 2004). In Fig. 3(b), with increased penetration rate, $U_D = 10^2$, and constant monitoring location $[(x_D = (1/100)(U_D/N_D)]$, response time increases, relative to time to arrest as permeability increases. For rapid insertion, the pressure buildup that results from the transducer moving into the pressure bulb is generated essentially instantaneously with insertion and results in the sharp pressure rise apparent in Figs. 3(a and b). As the pressure monitoring location is moved further from the tip to one-tenth $[x_D = (1/10)(U_D/N_D)]$ of the embedment depth from one-hundredth $[x_D = (1/100)(U_D/N_D)]$ of the embedment depth as illustrated in Fig. 3(c), the diffusive response is shifted in time. This represents the time that the transducer enters the sharply defined pressure bulb created by the penetrometer as it

enters the seabed. For the increased material strength, $N_D = 10^3$, penetration rate, $U_D = 10^4$, and constant monitoring location $[x_D = (1/100)(U_D/N_D)]$ as illustrated in Fig. 3(d), response time increases and the pressure response at larger taper angles $(\theta \to 90°)$ asymptote to unity, as $P_D x_D \to 1$.

Peak Pressure Magnitudes

Unlike penetration at constant velocity, U, where the pressures build to a dynamic steady state (Elsworth 1991), the peak pressures of interest for the decelerating penetrometer occur at the time of penetrometer arrest. From this state the pressures then dissipate. The distribution of peak pressures on the shaft of a decelerating penetrometer may be determined from $t|_{\dot{x}'=0}$, defined in Eq. (8), and resubstituted into Eq. (29), as $t'_D = \pi/N_D$. Since the penetrometer may arrest before it reaches a steady pressure distribution, it is likely that the pressure induced around a decelerating penetrometer may, in some circumstances, be less than for steady penetration.

This is the steady solution where the pore fluid pressure remains constant around the tip of the penetrometer when viewed relative to migrating coordinate system. Remote from the penetrometer tip the integral may be decoupled to evaluate $2\tan^2\theta \int_0^{l_D} \chi_D d\chi_D = \tan^2\theta l_D^2 = 1$ and the steady pressure distribution around a conical penetrometer under constant velocity penetration of U is defined as (Elsworth 1991, 1998)

$$P_D = \frac{1}{R_D} e^{-U_D(R_D - x_D)} \tag{30}$$

where the nondimensional penetration velocity is $U_D = Ua/2c$. Behind the blunt tip of the penetrometer, and on the shaft, this reduces to $P_D = 1/x_D$, allowing direct comparison with peak pressure magnitudes for the decelerating penetrometer. Most conveniently, this is plotted as $\log x_D$ versus $\log P_D$, where Eq. (30) plots as a straight line, as apparent in Fig. 4. In the zone ahead of the shoulder of the penetrometer ($0 < x_D < l_D$), the pore fluid pressure magnitudes are singular in this range, due to the assumed zero radius of the conical tip of the cone. This steady behavior reduces to $P_D = 1/x_D$ for large x_D, identical to the behavior for a blunt penetrometer. The $1/x_D$ distribution along the shaft is valid only at large separations from the tip, where the behavior for the tapered penetrometer approaches that for the blunt penetrometer for x_D greater than a few taper lengths, l_D. This is dependent only on the choice of taper angle for the cone, θ, as $\tan\theta = 1/l_D$. For a decelerating penetrometer, the results asymptote to the distribution defined for $U_D \leqslant 10^{-1}$ for slow impact. Under these conditions the pore pressure distribution around the tip has not yet reached the dynamic steady state represented by the straight line for $P_D = 1/x_D$. Physically, this represents the case where pressure transducers are far enough along the shaft that the penetrometer arrests before the transducer location may enter the induced pressure bulb. The pressure distribution for slow penetration will be near-spherical around the tip, and is influenced by the aggregate velocity along the path of the penetrometer, terminating at zero velocity.

Where the penetrometer impacts at a higher velocity, for example, for $U_D \geqslant 10^0$, the pressure distribution asymptotes to steady behavior. As nondimensional impact velocities become larger, the match to the steady behavior becomes closer, mainly because the embedment length increases proportionally to U_D as $x'_D = U_D/N_D$. These curves will be self-similar as the embedment length increases. Note that the pressure distributions are not truncated at the seabed, for $x_D > U_D/N_D$, because the medium is
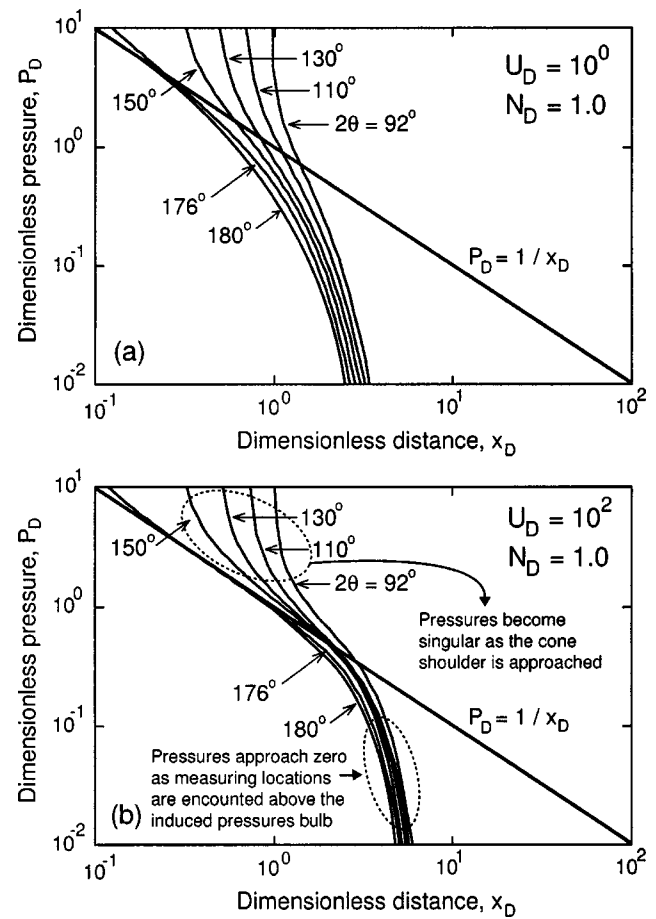
Fig. 4. Peak dimensionless pressure, P_D, measured along the penetrometer shaft illustrating the influence of penetrometer taper relative to the behavior for a blunt penetrometer, at the time of penetrometer arrest, $t'_D = \pi/N_D$. All pressures for both (a) and (b) correspond to dimensionless velocities of $U_D = 10^0$ and $U_D = 10^2$, and dimensionless strength of $N_D = 1$.

considered infinite, rather than semi-infinite, even though the effect of penetration is only applied following the presumed impact at the seabed at velocity U_0. As discussed previously, this effect will be small for typical embedment length.

The form of the contoured distribution of pressures around the tip is shown in Fig. 5 for a 120° cone ($2\theta = 120°$) with the tip centered on the origin, using Eq. (29). The magnitude of P_D may also be determined in the zone ahead of the shoulder of the penetrometer ($0 \leqslant x_D \leqslant l_D$), (Elsworth 1998). For high velocity impacts, the pressure distribution is cylindrical around the penetrometer, and markedly decreases in spread away from the penetrometer with an increase in nondimensional impact velocity, U_D. As the impact velocity is reduced, the pressure distribution becomes spherical, representing the dominant influence of the most recent portion of the advanced penetrometer, local to the tip. As nondimensional impact velocities are reduced below $U_D < 10^{-1}$, the distributions become identical, indicating the control of pressure diffusion in dissipating the pressures, and a reduction in the relative influence of the migrating penetrometer. Importantly, the contoured representations are not truncated at the seabed surface, as the diffusive solution is for an infinite medium, even though the penetrometer was only "turned-on" as it impacted the seabed surface.

Fig. 5. Peak pressure distribution centered on the tip of a 120° (2θ) cone at $(x_D, y_D) = (0,0)$. Taper length is defined by semiapical angle as $l_D = 1/\tan\theta$. Results document magnitudes of P_D in multiples of 2^{-n} within a radius of $R'_D = 1$ of the cone tip. All figures locate the tip at the time of arrest, at the origin of the plot.

Postarrest

Postarrest behavior may be evaluated by superposing a moving dislocation of negative strength, beginning at the time of arrest, $t|_{\dot{x}'=0}$, defined as t'_D, over the positive strength moving dislocation that is applied continuously from the time of impact. Physically, the coincident moving dislocations of opposite strength, that initiate over the "phantom" trajectory of penetrometer, postarrest, enforce approximate boundary conditions for the system. Behavior at any time, $t_D > t'_D$, may be determined from the coincident and colinear moving dislocations, the first representing dilation from $0 \rightarrow t_D$ and the second representing an equivalent but opposite contractile volumetric dislocation from $t'_D \rightarrow t_D$ beginning from the location of the arrested tip at time t'_D. The effects of the coincident dislocation, ahead of the arrested tip, exactly cancel. The system equations follow directly from Eq. (29) as

$$P_D = \frac{2\tan^2\theta}{\sqrt{\pi}} \int_0^{l_D} \int_0^{t_D} \chi_D \frac{e^{-\tilde{R}_D^2/(t_D - \tau_D)}}{(t_D - \tau_D)^{3/2}}$$

$$\times \cos\left[\frac{1}{2}N_D(t_D - \tau_D)\right] d\tau_D d\chi_D$$

$$- \frac{2\tan^2\theta}{\sqrt{\pi}} \int_0^{l_D} \int_{t'_D}^{t_D} \chi_D \frac{e^{-\tilde{R}_D^2/(t_D - \tau_D)}}{(t_D - \tau_D)^{3/2}}$$

$$\times \cos\left[\frac{1}{2}N_D(t_D - \tau_D)\right] d\tau_D d\chi_D \qquad (31)$$

or alternatively as

$$P_D = \frac{2\tan^2\theta}{\sqrt{\pi}} \int_0^{l_D} \int_0^{t'_D} \chi_D \frac{e^{-\tilde{R}_D^2/(t_D - \tau_D)}}{(t_D - \tau_D)^{3/2}}$$

$$\times \cos\left[\frac{1}{2}N_D(t_D - \tau_D)\right] d\tau_D d\chi_D \qquad (32)$$

where the coordinate system migrates with the continuously migrating dislocation, postarrest, and pressures are referenced relative to this coordinate system. To transform to coordinates relative to the arrested penetrometer, a periodic transformation must be applied. Where the coordinate system $[\hat{x}, \hat{y}, \hat{z}]$ is chosen to represent locations relative to the arrested penetrometer ($[\hat{x}]$ is the distance of the pressure-measuring transducer behind the penetrometer tip), the linkage between the two coordinate systems is

$$x = \hat{x} - \frac{U_0}{b} + \frac{U_0}{b}\sin[b(t)]$$

$$y = \hat{y} \qquad (33)$$

$$z = \hat{z}$$

where arrest always occurs at time, $t_{\text{arrest}} = t' = \pi/2b$ and

$$\tilde{x} = x - \frac{U_0}{b}\sin[b(t-\tau)] - \chi \qquad (34)$$

The same nondimensional coordinate system may be invoked to yield the coordinate transform

$$x_D = \hat{x}_D - \frac{U_D}{N_D}\left[1 - \sin\left(\frac{1}{2}N_D t_D\right)\right] \qquad (35)$$

or $\tilde{x}_D = \hat{x}_D + (U_D/N_D)[\sin(1/2 N_D t_D) - 1] - (U_D/N_D)\sin[1/2 N_D(t_D - \tau_D)] - \chi_D$ by substituting Eq. (35) into Eq. (34) and the result into $\tilde{R}_D = \sqrt{\tilde{x}_D^2 + y_D^2 + z_D^2}$. This results in an appropriate transform where the time to arrest is $t'_D = \pi/N_D$ and enables Eq. (31) to be directly evaluated.

Figure 6 describes the dissipation behavior following arrest at time t'_D. The time since arrest is defined as $(t_D - t'_D)$, and these plots, for transducer locations at 1/100 and 1/10 of the embedment length from the tip follow directly from the buildup data of Fig. 3. Maximum magnitudes of $P_D x_D$ track across from the buildup curves of Fig. 6, setting the peak pressure that falls following arrest. The dissipation behavior is included in Figs. 6(a–d) for a pressure transducer located one-hundredth $[x_D = (1/100)(U_D/N_D)]$ and one-tenth $[x_D = (1/10)(U_D/N_D)]$ of the embedment length back from the penetrometer tip. Similar to the pressure buildup behavior, dissipation is close to the behavior of a blunt penetrometer for large taper angles of the cone, θ, with different penetration rates, U_D, and material strengths, N_D. As in Figs. 6(b and c), dissipation is more rapid for a high nondimensional impact velocity, $U_D = 10^2$, and a transducer location further from the tip $[x_D = (1/10)(U_D/N_D)]$, and slowest for a low impact velocity, $U_D = 10^1$ with given transducer location $[x_D = (1/100)(U_D/N_D)]$, as in Fig. 6(a). The dissipation response is rapid for high nondimensional material strength, $N_D = 10^3$, with given high nondimensional impact velocity, $U_D = 10^4$, apparent in Fig. 6(d). As the cone taper approaches a blunt tip, as in Figs. 6(a–d), the pore pressures have a greater opportunity to build to the steady magnitude of $P_D x_D = 1$.

At low magnitudes of nondimensional penetration velocity, $U_D < 10^0$, the dissipation curves are all of similar form. At high impact velocities, $U_D \geq 10^1$, the dissipation response is rapid and results from the thin pressure "skin" that develops around the penetrometer shaft (Fig. 5). These results enable the time to 50%
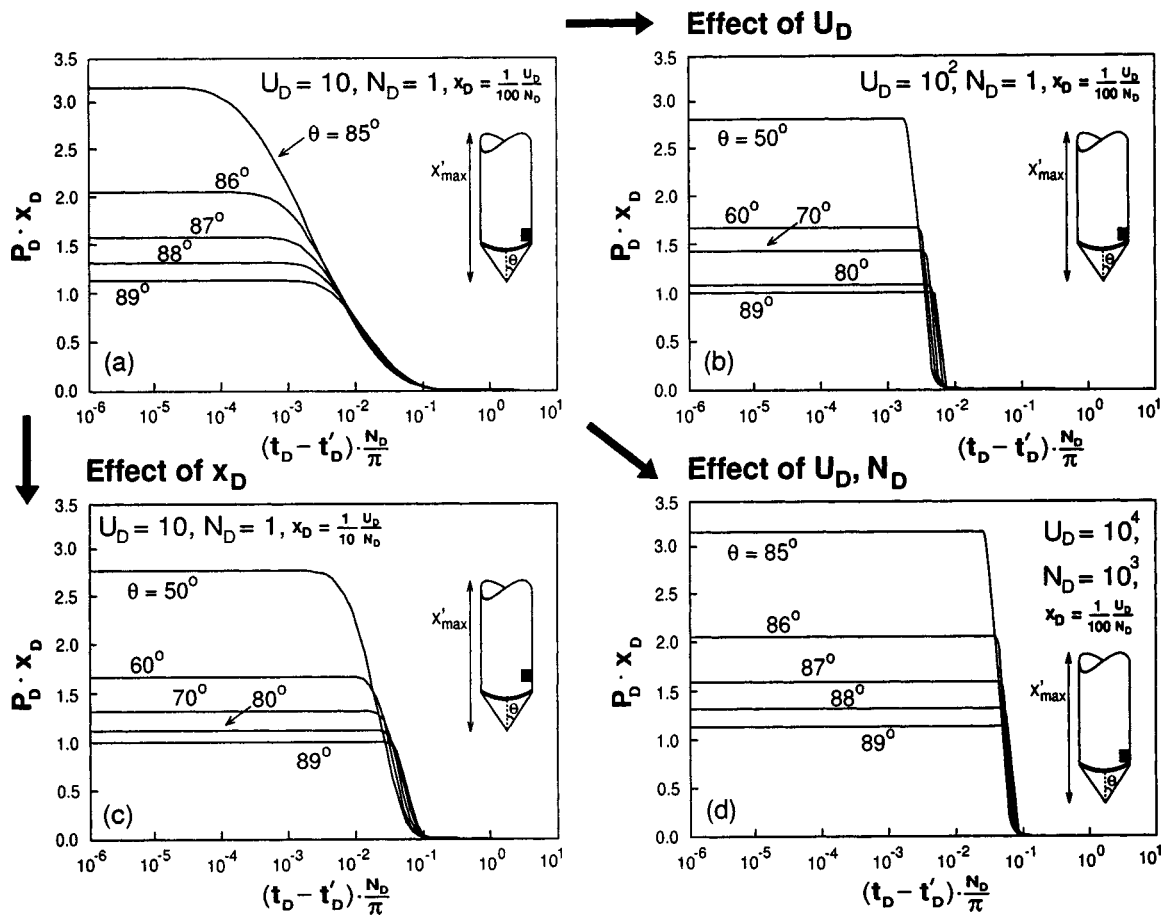
Fig. 6. Dissipation response following penetrometer arrest at time, t'_D. Change in nondimensional pressure is recorded as the product $P_D x_D$ for a transducer located a distance (a), (b), and (d) $x_D = (1/100)(U_D/N_D)$, (c) $x_D = (1/10)(U_D/N_D)$, behind the penetrometer tip. This represents a constant proportion of 1/100 and 1/10 of the total embedment length back from the tip. Pressure response is for various taper angles for the cone, θ, impact velocities, U_D, and material strengths, N_D.

pressure dissipation, t_{50}, to be determined, enabling hydraulic diffusivity, or consolidation coefficient, c, to be determined from the dissipation response.

Conclusions

A general treatment has been developed to represent the buildup and dissipation of pore pressures that result around a decelerating tapered penetrometer as it embeds within a poroelastic seabed. Pressure buildup and dissipation results have been specifically generated for various taper angles for the cone, θ, penetration rates, U_D, material strengths, N_D, and for two different monitoring locations $[x_D = (1/100)(U_D/N_D); (1/10)(U_D/N_D)]$. These strength magnitudes were selected as representative of a range of seabed sediment strengths. These results may be generalized for various strengths, by selecting appropriate groupings of nondimensional parameters. These parameter groups are different for buildup and for dissipation.

The assumed zero radius of the penetrometer in the zone of tip taper results in singular magnitudes of induced pore pressure in this region $(0 \leq x_D \leq l_D; y_D = z_D = 0)$. Behind the penetrometer tip, pore pressures asymptote to the blunt penetrometer distribution of $P_D = 1/x_D$ as x_D becomes large. If the time of arrest and taper angle for the cone are known, the peak pressure magnitude, corresponding to that time may be defined. In the limit, and for

small penetration velocities, $P_D x_D = 1$, and confirms the $P_D = 1/x_D$ pressure distribution along the shaft, apparent for steady penetration, as in Eq. (30).

The peak pressure for a tapered penetrometer may vary from this steady distribution due to both the effect of tip-taper and the unsteady behavior occasioned by penetrometer arrest. Tip-pressures are accentuated by the role of the tapered tip, as a result of pushing the singular pressures present at the tip shoulder further along the shaft. Further behind the tip, pressures measured beyond the penetration induced pressure bulb are lower than steady pressures, due to the brief period pressures are induced around the decelerating penetrometer.

Finally, since the nondimensional pressure, P_D, includes the magnitude of permeability, k, the peak generated pressure may be used to evaluate transport parameters of both permeability and consolidation coefficient or synonymous hydraulic diffusivity. From the definition of dimensionless pressure, P_D, of Eq. (24), permeability may be determined for peak insertion pressure, $p - p_s$, as

$$\frac{k}{\mu} = \frac{U_0 a}{4(p - p_s)x_D} \tag{36}$$

provided behavior has asymptoted to $P_D x_D = 1$. The appropriateness of using $P_D x_D = 1$ as a method of evaluating permeability may be determined only from dissipation data, used to evaluate U_D and from the form of the tip-local pressure distribution de-

fined in Fig. 4. In general, the relation of Eq. (36) cannot be used without correction. This is an important finding of this study.

Applying Eq. (36) to pore pressure data from pop-up pore pressure instrument (PUPPI) deployments (Urgeles et al. 2000) off La Palma, in the Canary Islands, enables permeabilities, k, and coefficient of consolidation, c, to be calculated directly from the peak pressure data and the dissipation response, respectively. For a 9.4° angle of cone taper, θ, an impact velocity, U_0, of 0.4 ms^{-1}, a penetrometer radius, a, of 0.019 m, a location of the pressure port (x) at 1.7 m behind the tip, and peak pressure ($p - p_s$) in the range 0.4–80 kPa, permeabilities may be recovered in the range 2×10^{-13} to 2×10^{-11} m^2. The evaluated results are higher than permeabilities obtained either from the tidal response, 10^{-18} to 10^{-16} m^2 (Urgeles et al. 2000) or from laboratory tests, 10^{-16} to 10^{-15} m^2 (Robert and Cramp 1996). This mismatch may result from rapid pressure dissipation along the shaft–soil interface, resulting in poor measurement of the peak pressure.

The solutions provide feasible mechanisms to evaluate transport properties of the penetrated seabed sediments. The first method involves the use of peak penetration-induced pressure as a proxy for permeability, that is independent of both drained compressibility measurements on recovered cores, or correlations with tidally forced pore-fluid pressures. The second method relates the matching of measured dissipation response to consolidation coefficient magnitudes, c, to be determined. These are determined by matching actual time-pressure responses with those for dimensionless-time and dimensionless-pressure to relate time directly with diffusive time, t_D, and thereby evaluate consolidation coefficient, c.

This full suite of penetration induced pore fluid pressure and subsequent dissipation responses offer the potential to better understand tip-local processes and the determination of sediment transport parameters from recorded pore pressure response.

Notation

The following symbols are used in this paper:

a = penetrometer of radius [L];
c = coefficient of consolidation [L^2 T^{-1}];
K = hydraulic conductivity [L T^{-1}];
k = absolute permeability [L^2];
N_c = dimensionless bearing capacity factor [—];
N_D = dimensionless strength [—];
P_D = dimensionless pressure [—];
p = absolute pore fluid pressure [F L^{-2}];
$p - p_s$ = excess pore pressure [F L^{-2}];
p_s = initial static fluid pressure [F L^{-2}];
q_u = bearing capacity [F L^{-2}];
R = radius of interest $R^2 = x^2 + y^2 + z^2$ [L];
S_u = undrained cohesive strength [F L^{-2}];
t = time (current) [T];
t_D = dimensionless time (current) [—];
t_D' = dimensionless time of penetrometer arrest [—];
U = penetration rate [L T^{-1}];
U_D = dimensionless penetration rate [—];
U_0 = terminal velocity [L T^{-1}];
x = location of excess pore pressure [L];
x' = distance below seabed surface [L];
x, y, z = global Cartesian coordinates [—];
x_D, y_D, z_D = dimensionless Cartesian coordinates $(x/a; y/a; z/a)$ [—];
η = integration coefficient [—];
θ = semiapical angle [—];
μ = fluid dynamic viscosity [F T];
ξ = dimensionless inverse root time $\xi = R / \sqrt{c(t - \tau)}$ [—];
τ = time integrating parameter [—]; and
χ = global coordinate [—].

References

Acar, Y., and Tumay, M. T. (1986). "Strain field around cones in steady penetration." *J. Geotech. Eng.,* 112(2), 207–213.

Baligh, M. M. (1985). "Strain path method." *J. Geotech. Eng.,* 111(9), 1108–1136.

Baligh, M. M., and Levadoux, J. N. (1986). "Consolidation after undrained piezocone penetration. II: Interpretation." *J. Geotech. Eng.,* 112(7), 727–745.

Baligh, M. M., and Scott, R. F. (1976). "Analysis of deep wedge penetration in clay." *Geotechnique,* 26(1), 185–208.

Biot, M. A., and Willis, D. G. (1957). "The elastic coefficients of the theory of consolidation." *J. Appl. Mech.,* 24, 594–601.

Cleary, M. P. (1977). "Fundamental solutions for a fluid saturated porous solid." *Int. J. Solids Struct.,* 13(9), 785–806.

Davis, E. E., Horel, G. C., MacDonald, R. D., Villinger, H., Bennett, R. H., and Li, H. (1991). "Pore pres-sures and permeabilities measured in marine sediments with a tethered probe." *J. Geophys. Res. B,* 96(B4), 5975–5984.

Drescher, A., and Kang, M. (1987). "Kinematic approach to limit load for steady penetration in rigid-plastic soils." *Geotechnique,* 37(3), 233–246.

Elsworth, D. (1991). "Dislocation analysis of penetration in saturated porous media." *J. Eng. Mech.,* 117(2), 391–408.

Elsworth, D. (1992). "Pore pressure response due to penetration through layered media." *Int. J. Numer. Analyt. Meth. Geomech.,* 16(1), 45–64.

Elsworth, D. (1993). "Analysis of piezocone data using dislocation based methods." *J. Geotech. Eng.,* 119(10), 1601–1623.

Elsworth, D. (1998). "Indentation of a sharp penetrometer in a poroelastic medium." *Int. J. Solids Struct.,* 35(34–35), 4895–4904.

Fang, W. W., Langseth, M. G., and Schultheiss, P. J. (1993). "Analysis and application of in situ pore pressure measurements in marine sediments." *J. Geophys. Res. B,* 98(B5), 7921–7938.

Harvey, F., Rudolph, D. L., and Frape, S. K. (1997). "Measurement of hydraulic properties in deep lake sediments using a tethered pore pressure probe: Applications in the Hamilton Harbour, western Lake Ontario." *Water Resour. Res.,* 33(8), 1917–1928.

Ladanyi, B. (1963). "Expansion of a cavity in a saturated clay medium." *J. Soil Mech. Found. Div., Am. Soc. Civ. Eng.,* 89(4), 127–161.

Lee, D. R. (1977). "A device for measuring seepage flux in lakes and estuaries." *Limnol. Oceanogr.,* 22(1), 140–147.

Levadoux, J. N., and Baligh, M. M. (1986). "Consolidation after undrained piezocone penetration. I: Prediction." *J. Geotech. Eng.,* 112(7), 707–726.

Richards, A. F., Oien, K., Keller, G. H., and Lai, J. Y. (1975). "Differential piezometer probe for an in situ measurement of sea-floor pore-pressure." *Geotechnique,* 25(2), 229–238.

Robert, J., and Cramp, A. (1996). "Sediment stability on the western flanks of the Canary Islands." *Mar. Geol.,* 134, 13–30.

Robertson, P., Campanella, R., Gillespie, D., and Greig, J. (1986). "Use of piezometer cone data. In Proceedings of In Situ '86." *American Society of Civil Engineers Speciality Conf. GSP 6,* New York, 1263–1280.

Robertson, P., Sully, J., Woeller, D., Lunne, T., Powell, J. M., and Gillespie, D. (1992). "Estimating coefficient of consolidation from piezocone tests." *Can. Geotech. J.,* 29(4), 539–550.

Schultheiss, P. J., and Noel, M. (1986). ''Direct indication of pore water advection from pore pressure measurements in the Madeira Abyssal Plain sediments.'' *Nature (London),* 320, 348–350.

Skempton, A. W. (1954). ''The pore pressure coefficients A and B.'' *Geotechnique,* 4(4), 143–147.

Skempton, A. W. (1959). ''Cast-in situ bored piles in London clay.'' *Geotechnique,* 9, 158.

Torstensson, B. A. (1977). ''The pore pressure probe.'' *Nord. Geotekniske Mote.,* 34, 34.1–34.15.

Tumay, M. T., Acar, Y. B., Cekirge, M. H., and Ramesh, N. (1985). ''Flow field around cone in steady penetration.'' *J. Geotech. Eng.,* 111(2), 193–204.

Urgeles, R., Canals, M., Roberts, J., and the SNV ''Las Palmas'' Shipboard Party. (2000). ''Fluid flow from pore pressure measurements off La Palma, Canary Islands.'' *J. Volcanol. Geotherm. Res.,* 101, 253–271.

Vesic, A. (1972). ''Expansion of cavities in infinite soil mass.'' *J. Soil Mech. Found. Div., Am. Soc. Civ. Eng.,* 98(3), 265–290.

Wang, K., and Davis, E. E. (1996). ''Theory for the propagation of tidally induced pore pressure variations in layered subseafloor formations.'' *J. Geophys. Res. B,* 101(B5), 11483–11495.

Watts, A. B., and Masson, D. G. (1995). ''A giant landslide on the north flank of Tenerife Canary Islands.'' *J. Geophys. Res. B,* 100(B4), 24487–24498.

VITA – Dae Sung Lee

Professional Preparation

Pennsylvania State University, USA   Energy & Geo-Environmental Engineering   Ph.D.   2006

Pennsylvania State University, USA   Geo-Environmental Engineering   M.S.   2001

Dong-A University, South Korea   Mineral and Mining Engineering   B.Sc.   1998

Experiences

2005 ~2006 **Co-Instructor**, Geo-Environmental Engineering, Pennsylvania State University

2001 ~ 2006 **Teaching Assistant**, Geo-Environmental Engineering, Pennsylvania State University

2001 ~2006 **Computer Assistant**, Geo-Environmental Engineering, Pennsylvania State University

2000 ~ 2006 **Research Assistant**, Geo-Environmental Engineering, Pennsylvania State University

University Services

2005   Member, EGEE Computer committee, Geo-Environmental Engineering, Pennsylvania State University

Awards & Honors

2005   EGEE Graduate Teaching Assistant of the Year, Pennsylvania State University

2005   Outstanding Graduate Teaching Assistant Award in GeoEE, Pennsylvania State University

2005   EMS Centennial Graduate Research Award, Pennsylvania State University

1998   LG 21st Centuries Global Challenger, South Korea

Publications

1.   **Lee, D.S**., Elsworth, D., Hryciw, R.D., and Butler, Jr. J.J. (2006). Hydraulic conductivity measurement from the-on-fly uCPT sounding and from VisCPT. - *ASCE Journal of Geotechnical and GeoEnvironmental Engineering* (under review).

2.   **Lee, D.S**., Elsworth, D., Butler, Jr. J.J., and Dietrich, P. (2006). Direct Evaluation of Permeability from uCPT Soundings: Validation against Data from the Nauen Test Site, Germany – *Canadian Geotechnical Journal* (under review).

3.   Elsworth, D., **Lee, D.S**., Hryciw, R.D., and Shin, S.C. (2006). Pore pressure response following undrained uCPT sounding in a Dilating Soil. - *ASCE Journal of Geotechnical and GeoEnvironmental Engineering* (in press).

4.   Elsworth, D. and **Lee, D.S**. (2005). Limits of Determining Permeability from On-the-fly CPT Sounding - *Geotechnique* (under review).

5.   Elsworth, D and **Lee, D.S**. (2005). Permeability Determination from On-the-fly Piezocone Sounding - *ASCE Journal of Geotechnical and GeoEnvironmental Engineering* Vol 131, No 5, 1-11.

6.   Elsworth, D and **Lee, D.S**. (2005). Indentation of a Free-Falling Lance Penetrometer into a Poroelastic Seabed - *International Journal for Numerical and Analytical Methods in Geomechanics* Vol 29, No 2, 141 – 162.

7.   **Lee, D.S**. and Elsworth, D (2004). Indentation of a Free-Falling Sharp Penetrometer into a Poroelastic Seabed - *ASCE Journal of Engineering Mechanics* Vol 130, No 2. 170 - 179.

8.   Elsworth, D., **Lee, D.S**., Long, H., and Flemings, P (2003). Penetration-Induced Pore Pressure Magnitudes - Methods to Determine Transport Parameters from Terrestrial and Marine Penetrometer Testing - *GeoProc 2003, International Conference on Coupled T-H-M-C Processes in Geosystems*, October 2003, 475-480.